The numerical simulation of astrospheric evolution in different interstellar environments

A Marais

orcid.org/0000-0002-5040-5896

Dissertation accepted in partial fulfilment of the requirements for the degree *Master of Science in Astrophysical Sciences* at the North-West University

Supervisor: Prof SES Ferreira

Graduation May 2023

26994852

Acknowledgements

I would like to thank my supervisor Prof S.E.S Ferreira for his guidance and encouragement throughout my research.

I would also like to express my gratitude towards Juandre Light for always being willing to lend a helping hand as well as my parents for their unconditional love and support.

I would like to give special thanks to the National Research Foundation (NRF) for their financial support.

Abstract

The interaction between the interstellar medium (ISM) and a stellar wind leads to the formation of an astrosphere. In this study, the evolution of astrospheres is simulated with a two-dimensional spherical hydrodynamic (HD) and magnetohydrodynamic (MHD) model, and a three-dimensional cartesian MHD model. The two-dimensional HD and MHD model of Fahr et al. (2000), Scherer & Ferreira (2005) and Ferreira & de Jager (2008) is first used to show the effect of radiative cooling on simulations and also to illustrate the effect that changing parameters such as the mass-loss rate, ISM density and the ISM magnetic field have on the astrospheric evolution. It was shown that radiative cooling has an effect on the overall astrosphere size, and the termination shock (TS), astropause (AP) and bow shock (BS) positions and compression ratios (defined as the difference in density between the shocked and unshocked fluid). The compression ratios are also influenced by the ISM density, along with the rate of cooling. Changing the mass-loss rate influences the ram pressure, affecting the size of the astrosphere. The ISM magnetic pressure is dependent on the ISM magnetic field magnitude, and increases as the ISM magnetic field increases. Comparing different ISM magnetic field magnitude scenarios with each other shows that a higher ISM magnetic pressure influences the outer shell of the astrosphere and allows the outer astrosheath (OAS) to decompress faster. For the second part of this study, the three-dimensional cartesian MHD model of Pen et al. (2003) is used to simulate the astrospheric expansion for different grid cell sizes and to show the effect that different ISM wind speeds and different outflow speeds have on the evolution of M-Dwarf astrospheres. The choice of grid cell size is important as it influences the compression ratios of the TS and BS. Also computed were the astrospheres of LHS 1140 and Proxima Centauri. Comparing these simulations to results obtained by Herbst et al. (2020) showed that there are some differences between the astrospheres of LHS 1140 and Proxima Centauri, which can be attributed to the different models, grid geometries and parameters used.

keywords: Astrospheres, stellar wind, interstellar medium, magneto-hydrodynamics, interstellar magnetic field, radiative cooling.

Contents

1 Introduction **8**

2 Method **19**

2.1 Two-dimensional HD and MHD simulations 19

2.2 Three-dimensional MHD simulations 27

2.3 Summary 31

3 Astrospheric expansion **32**

3.1 Introduction 32

3.2 The effect of different mass-loss rates on astrospheric evolution 32

3.3 The effect of different ISM densities on astrospheric evolution 38

3.4 The effect of different ISM magnetic field strengths on astrospheric evolution 41

3.5 Summary and Conclusions 48

4 Three-dimensional simulations **53**

4.1 Introduction 53

4.2 Asymmetrical results 55

4.3 Bullet-shaped cavity 59

4.4 Comparing results corresponding to different magnetic field orientations 63

4.5 Summary and Conclusions 67

5 Three-dimensional simulations of M-stars **69**

5.1 Introduction 69

5.2 Astrospheric simulations of LHS 1140 71

5.3 Astrospheric simulations of Proxima Centauri 76

5.4 Summary and Conclusions 81

6 Summary and Conclusions **83**

Chapter 1

Introduction

The interaction and properties of a surrounding interstellar medium (ISM) and a stellar wind determine the structure of an astrosphere, also known as a circumstellar bubble (van Marle et al. 2015) and (Wood & Linsky 2016). Figure 1.1, taken from Strauss (2013), is a three-dimensional illustration for the heliosphere, which is our local astrosphere. Shown here is the computed solar wind speed ($\vec{v}$), with the colour of the flow lines is done in accordance with $\log_{10}$ of $|\vec{v}|$. The faster speeds are illustrated by the blue to magenta colours with the slower speeds being illustrated by the red colouring. As the solar wind flow progresses it is diverged in the direction of the heliospheric tail region, and as it moves past the termination shock (TS), non-radial components develop. Here the solar wind also forms strong polar components and azimuthal components. The ISM $|\vec{v}|$velocity is also diverged in a similar manner. The heliospheric (and astrospheric) structures discussed above also play an important role in, e.g., the modulation of cosmic rays over time.

As shown in Figure 1.1, when a star has a relative speed that is non-zero with respect to the surrounding ISM, the star creates a bullet-shaped astrosphere. This characteristic is especially noticeable with runaway stars (Van den Eijnden et al. 2022). Some display bow shocks (BS), which occur when these types of stars move through the interstellar medium with supersonic velocities, and in so doing the ISM is swept up in front forming a BS. These types of stars have relative velocities between 40 $\mathrm{km\,s^{-1}}$ and 200 $\mathrm{km\,s^{-1}}$, as mentioned in, e.g., Perets & Subr (2012). For stars with a subsonic relative speed, there is no BS, but rather a bow wave (wave with an increased density and no shock) (McComas et al. 2012).

As mentioned above, a runaway star is associated with a relative velocity even greater than 100 $\mathrm{km\,s^{-1}}$. There are two possible explanations (the two main mechanisms) for the origin of these stars, see Gvaramadze et al. (2009), Perets & Subr (2012) and Lux et al. (2021). For a binary supernova scenario, it is possible for one of the stars to be expelled from the binary system (Perets & Subr

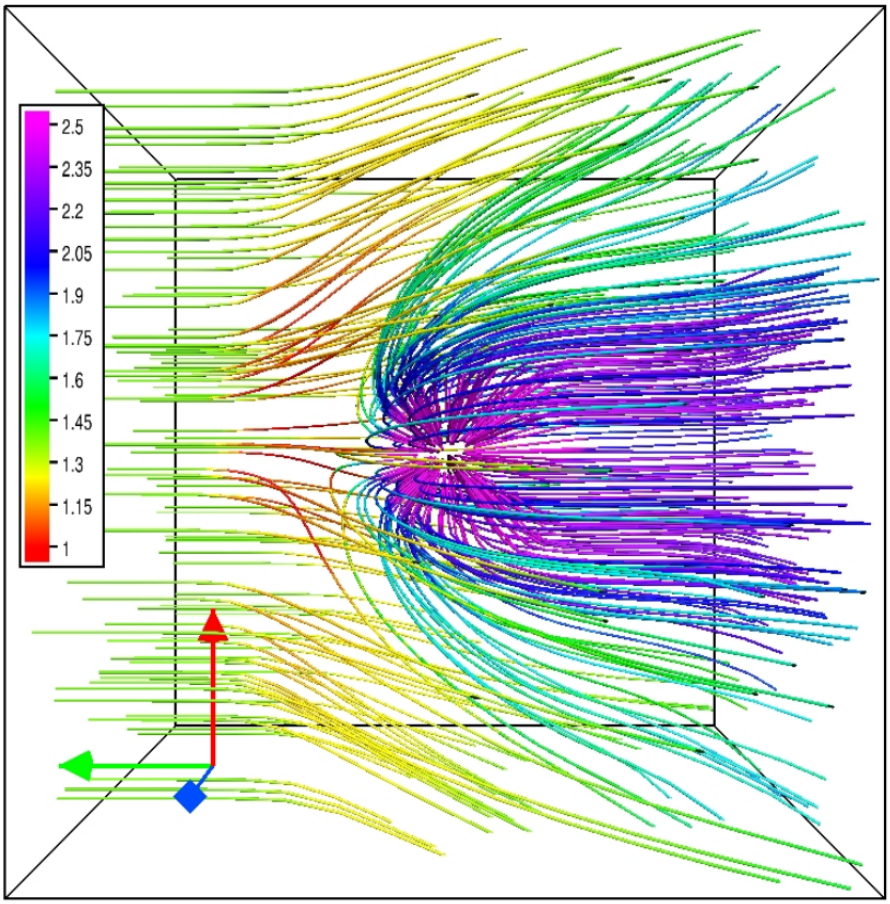

Figure 1.1: *Shows the heliosphere in terms of the computed solar wind speed ($\vec{v}$). The slower speed is illustrated with red and the colouring of the flow lines is done in accordance with the log_{10} of $|\vec{v}|$. A right hand coordinate system was used as indicated by the arrows. The red arrow is along the x-direction, the green arrow is along the y-direction and the blue arrow is along the z-direction. Figure was taken from Strauss (2013).*

2012). This is due to a supernova explosion of a companion star. Another possibility is the dynamical ejection model, where gravitational interactions between cluster members cause a star to be expelled. Between 30 and 40 % of O-type stars and about 5 to 10 % of B-type stars are runaway stars. Figure 1.2, [Credit: NASA/JPL/ESA], shows the bullet-shaped astrosphere created due to a relative speed between the star and the ISM.

The details of an astrospheric structure are demonstrated in Figure 1.3, taken from Scherer et al. (2015) and Scherer et al. (2016). The figure shows a standard hydrodynamic (HD) astrosphere. Visible in both panels are the point of reference $S_\star$, which represents the star, the TS, astropause (AP) and a BS (see also Light et al. (2022)). The inner astrosheath (IAS) is between the TS and the AP, with the outer astrosheath (OAS) found between the AP and the BS. For the simulations that include radiative cooling, the OAS is split into the cold outer astrosheath (COAS) and the hot

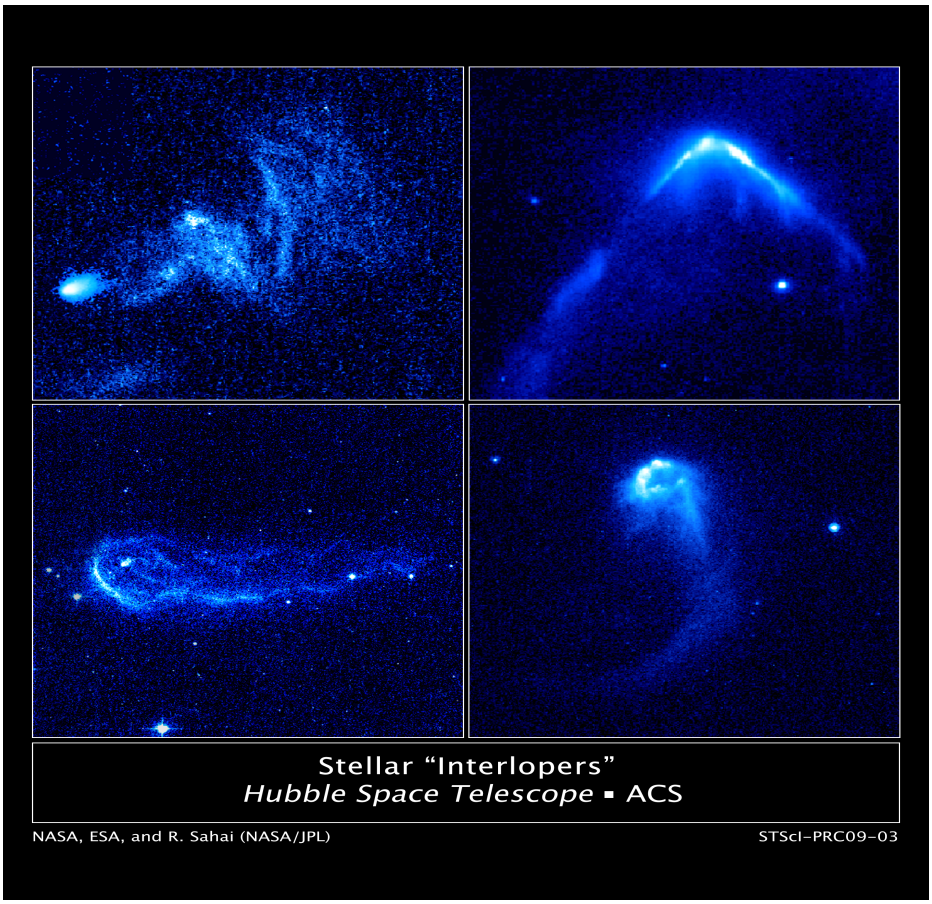

Figure 1.2: *The bullet-shaped astrospheres created by runaway stars. Credit: NASA/JPL/ESA*

outer astrosheath (HOAS) as seen in the bottom panel of Figure 1.3. The other features such as the tangential contact discontinuity (TD), the Mach disc (MD) and M, the mach number of a specific area, are of less importance in this study. Other features include the sonic lines (SL), a reflected shock (RS) and C as the middle point. For more detailed discussions, see Scherer et al. (2015), Light et al. (2022) and Herbst et al. (2022).

The TS forms due to a stellar wind interaction with the ISM. As the stellar wind (SW) flows outward, its speed decreases from a super to a subsonic flow at the TS, and afterwards there is an incompressible flow up to the AP, which is a discontinuity between the ISM and the stellar wind (Scherer et al. 2016). If there is motion between the ISM and the astrosphere, and when the relative speed is supersonic with respect to the ISM, a BS will form. However, no BS will form if the relative speed is subsonic. In the downwind direction beyond the TS, the astrotail is visible, while the nose is found in the upwind direction. In the downwind direction, an MD and a TD can also be observed (Herbst et al. 2022).

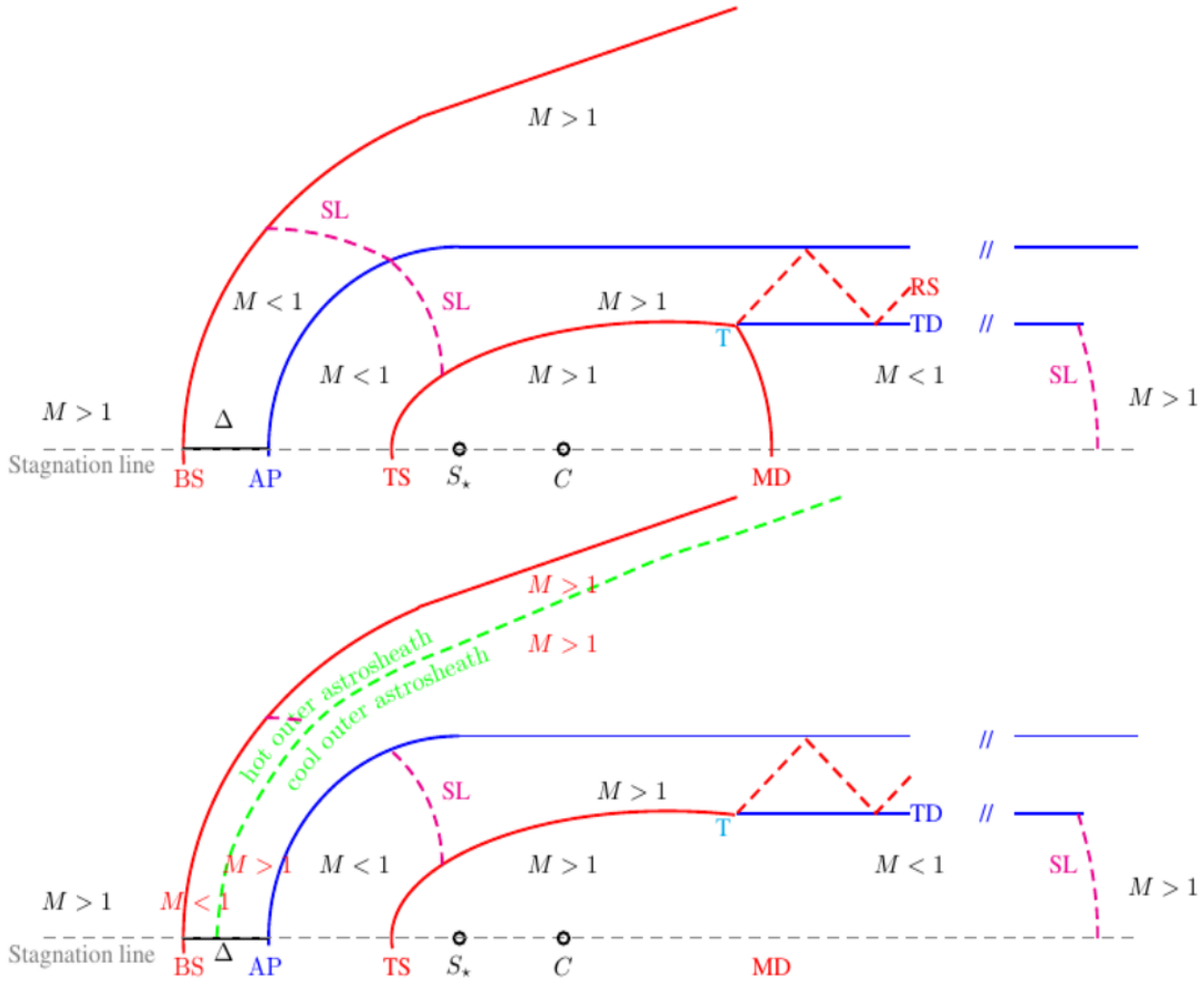

Figure 1.3: *The shock structure of an astrosphere is shown here. A standard hydrodynamic astrosphere is presented in the top panel. The bottom panel represents a hydrodynamic calculated astrosphere, with radiative cooling included in the model. This leads to a COAS and a HOAS. Both panels show a reference point* $S_\star$*, a termination shock (TS), astropause (AP) and a bow shock (BS). The figure was taken from Scherer et al. (2015) and Scherer et al. (2016).*

The stellar as well as the interstellar material are separated by the AP. The BS is found in the upwind direction with a paraboloid shape. The apex of both the AP and the TS is upwind of the star (Herbst et al. 2022). The structure of the astrosphere about the central axis is rotationally symmetric, for a pure HD case. This axis (the stagnation line) goes through the star and runs parallel to the downwind and upwind directions (Herbst et al. 2022). However, an MHD astrosphere can have a stagnation point, but with the effects of the magnetic field taken into account, it is generally not on the central axis.

Depending on the stellar wind properties, the BSs of massive stars are similar on a qualitative level to the heliosphere, but different on a quantitative level (Herbst et al. 2022). More often, the BSs of massive stars are roughly bigger than 10 pc (van Marle et al. 2015) and can be distorted by stellar motion. To simulate the structure of an astrosphere, the HD and MHD model of Fahr et al. (2000), Scherer & Ferreira (2005) and Ferreira & de Jager (2008) is used in Chapter 3. It will be shown that there are various parameters that can influence the structure of an astrosphere, e.g., the density, magnetic field and temperature of the ISM, and whether or not radiative cooling is included.

For example, one parameter that has the ability to affect not only the overall shape and size of the astrosphere, but also the compression ratio (difference in density between the shocked and unshocked fluid) of the BS, is the ISM magnetic field. From observations it is known that the ISM contains large-scale magnetic fields, with a magnitude between 1 μG and 60 μG, as recently stated by, e.g., Opher et al. (2009) and Heerikhuisen & Pogorelov (2011). The ISM magnetic field has the potential to influence the shape and size, either on a small or large scale, of the circumstellar bubbles. On a small scale, the ISM magnetic field has been observed to alter hydrodynamic instabilities (van Marle et al. 2015). On a large scale, minimal effects are expected on astrospheric evolution in the direction where the flow is parallel to the magnetic field, but in the direction perpendicular to the magnetic field, the magnetic pressure is expected to have maximal effects. When the ISM magnetic pressure is comparable to or larger than the thermal or ram pressure, it reduces the rate of expansion and in the process influences the shape and size of the circumstellar bubble. Studies done by Tomisaka (1990) and Ferriere (1998) showed that the bubble's rate of expansion is reduced in the direction perpendicular to the ISM magnetic field. For a faster and denser stellar wind or ISM, the effects of the magnetic field on astrospheric expansion decreases.

More recently, van Marle et al. (2015) reported on the effect of different magnetic field strengths on the evolution of a circumstellar bubble/astrosphere. The authors used the MPI-AMRVAC MHD code, explained in Keppens et al. (2012), for the simulations. These simulations, which were axi-symmetric, were done in a similar manner to that in van Marle et al. (2012). They found that, as expected, the expansion of the bubble is hindered in the direction perpendicular to the ISM magnetic field. As the interstellar magnetic field strength increases, so does the magnetic pressure. Should the ram pressure be smaller than the magnetic pressure, the evolution of the astrosphere is influenced by the magnetic field. As will be shown in Figure 1.4, this, in turn, results in the creation of an asymmetric interstellar bubble. Should the magnetic pressure be large enough, it can hinder the evolution of certain features, e.g. Wolf-Rayet ring nebulae.

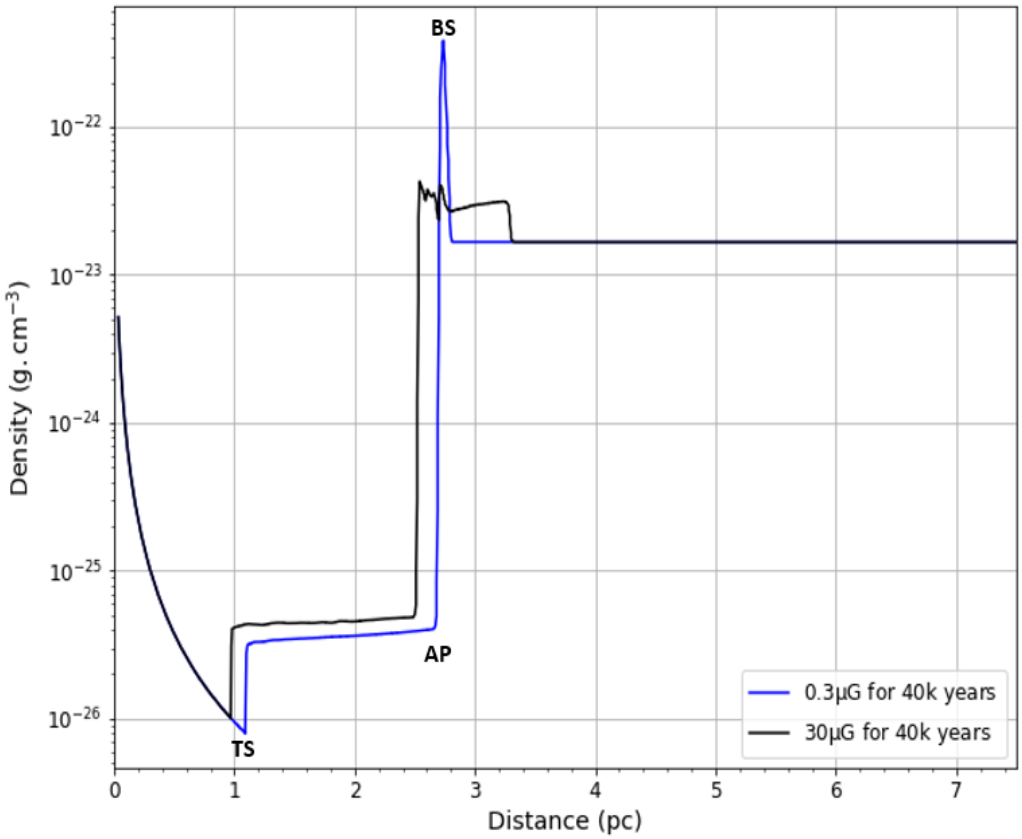

Figure 1.4: *The radial profile of the density as a function of distance from the inner boundary for two different interstellar magnetic field magnitudes after 40 000 years simulation time. The density is shown on a logarithmic scale. The blue line shows a small interstellar magnetic field of 0.3 μG and the black line shows a field of 30 μG.*

Figure 1.4 illustrates the abovementioned. The evolution of the interstellar bubble is simulated to show the effects of two different magnetic field magnitudes. Simulations were done with the modified two-dimensional MHD model of Fahr et al. (2000), Scherer & Ferreira (2005) and Ferreira & de Jager (2008), discussed in Chapter 2. The computed density is shown as a function of distance from the inner boundary and an astrosphere is simulated for a time interval of 40 000 years by using the modified two-dimensional MHD model discussed in Chapter 2.2. As the ISM magnetic field magnitude increases, the magnetic pressure exerted on the astrosphere increases, changing its structure. This also leads to an increase in the overall size of the astrosphere. The size of the OAS increases as the magnetic pressure increases. This happens due to the magnetic pressure that allows the OAS to decompress faster. Similar figures and features are discussed in more detail in later chapters.

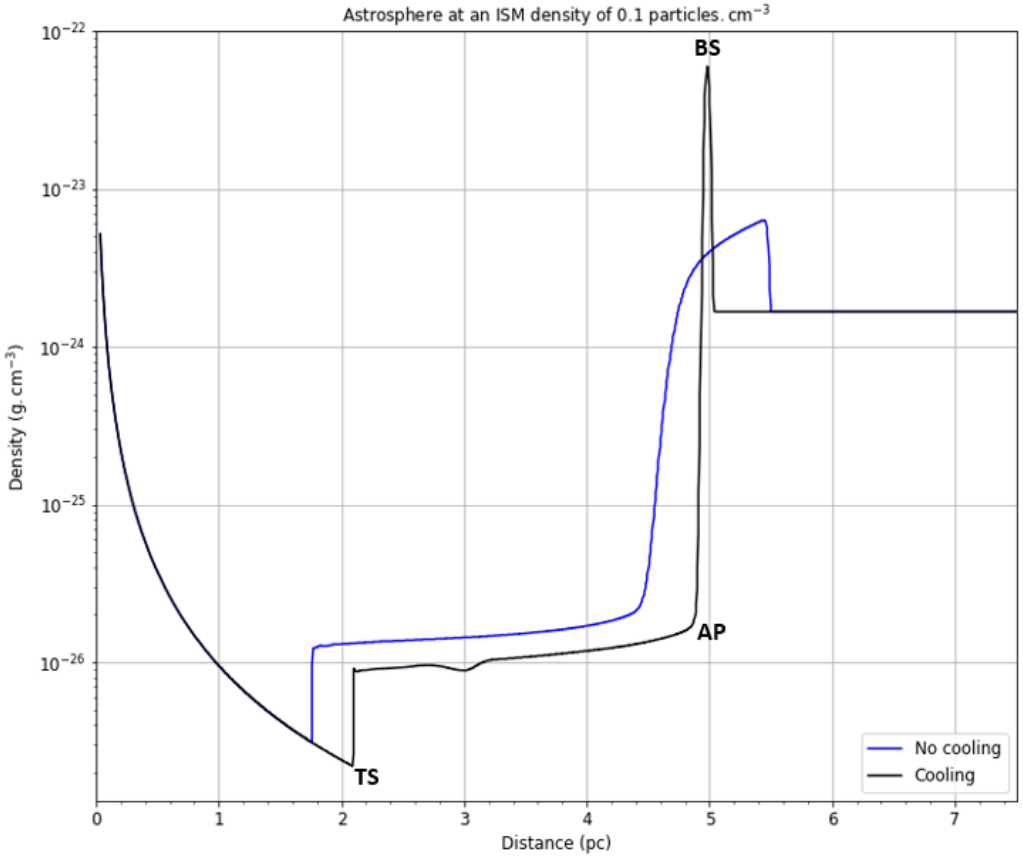

Figure 1.5: *The radial profile of an astrosphere for a scenario including and excluding cooling is shown. The computed density is given as a function of the distance from the inner boundary at 40 000 years simulation time. An ISM magnetic field magnitude of 0.3* μG *and an ISM density of* 1.6726×10^{-24} g cm^{-3} *are assumed. The black line shows the scenario with cooling and the blue line shows the scenario without cooling.*

It will be shown in Chapter 3 how radiative cooling influences astrospheric expansion. Figure 1.5 shows an example, and the computed density as a function of the distance from the inner boundary is shown to illustrate the effect of cooling on the shape and size of the astrosphere. Figure 1.5 is also simulated with the two-dimensional MHD model. The black line shows the scenario with cooling and the blue line the scenario without cooling. An ISM density of 1.6726×10^{-24} g cm^{-3} and an ISM magnetic field magnitude of 0.3 μG are assumed. For the scenario with cooling, the TS and AP are shifted further out, while the BS moves inwards. Whereas, for the scenario without cooling, the BS moves outwards, while the TS and AP shifts inwards. Radiative cooling influences the density and compression of the astrosphere's outer shell. Cooling reduces the OAS to a thin but dense structure.

Once the structure has cooled, the OAS starts to decompress and the density along with the compression ratio decreases.

As mentioned above, the effects that the ISM magnetic field and radiative cooling as well as other parameters have on astrospheric expansion will be reported on in more detail in Chapter 3 using the modified two-dimensional HD and MHD model of Fahr et al. (2000), Scherer & Ferreira (2005) and Ferreira & de Jager (2008). The reason why the two-dimensional model is chosen is due to the sensitivity of cooling on the grid cell size, e.g. (van Marle et al. 2015). In Chapter 4, a three-dimensional cartesian MHD model is used to illustrate the effect of grid cell size on astrospheric expansion. This model is discussed in Strauss (2013), who used the three-dimensional MHD model of Pen et al. (2003) to simulate the heliosphere. In Chapter 5, the three-dimensional model will again be used to simulate the astrospheric expansion of LHS 1140 and Proxima Centauri and compare these with calculations done by Herbst et al. (2020).

Although not the focus of this study, but important for the collaboration, e.g. Herbst et al. (2020) and Light et al. (2022), to which this study was closely related to, is the modulation of galactic cosmic rays in these astrospheres. Galactic cosmic rays (GCR) are energetic particles that can be modulated by their stellar wind, i.e. the cosmic ray position and intensity as a function of energy changes due to the out-blowing stellar wind, e.g., Manuel (2013) and Herbst et al. (2020). Recently, the effect of CRs on the atmospheres of exoplanets and how they influence the habitability (climate, astrospheric ionization, chemistry, etc.) of these planets became a topic of interest. The cosmic ray's ability to travel through an astrosphere is subject to the astrosphere's properties, such as the turbulent state, structure and volume. The astrospheric properties are determined by the stellar activity, stellar wind, inner and outer boundary conditions, the stellar type, etc. (Herbst et al. 2019). In Chapter 3, it will be shown how some of these parameters influence an astrosphere's evolution.

By making use of Parker's transport equation (Parker 1968), GCR modulation can be calculated. This was done for O-and B-type stars by, e.g., van der Schyff (2016) and Light (2017). In Herbst et al. (2020), the authors investigated the modulation of GCRs within the astrospheres of three M-type stars (Dittmann & et al. 2017), namely LHS 1140, V374 Pegasi and Proxima Centauri. Note that astrospheric magnetic fields have an impact on the GCR propagation, lowering the GCR flux. Herbst et al. (2020) used a three-dimensional MHD model that makes use of the magnetic field and the stellar wind speed distributions to explore the GCR modulation of the chosen stars. It was concluded that the effect of GCRs has to be taken into account when measuring for habitability of

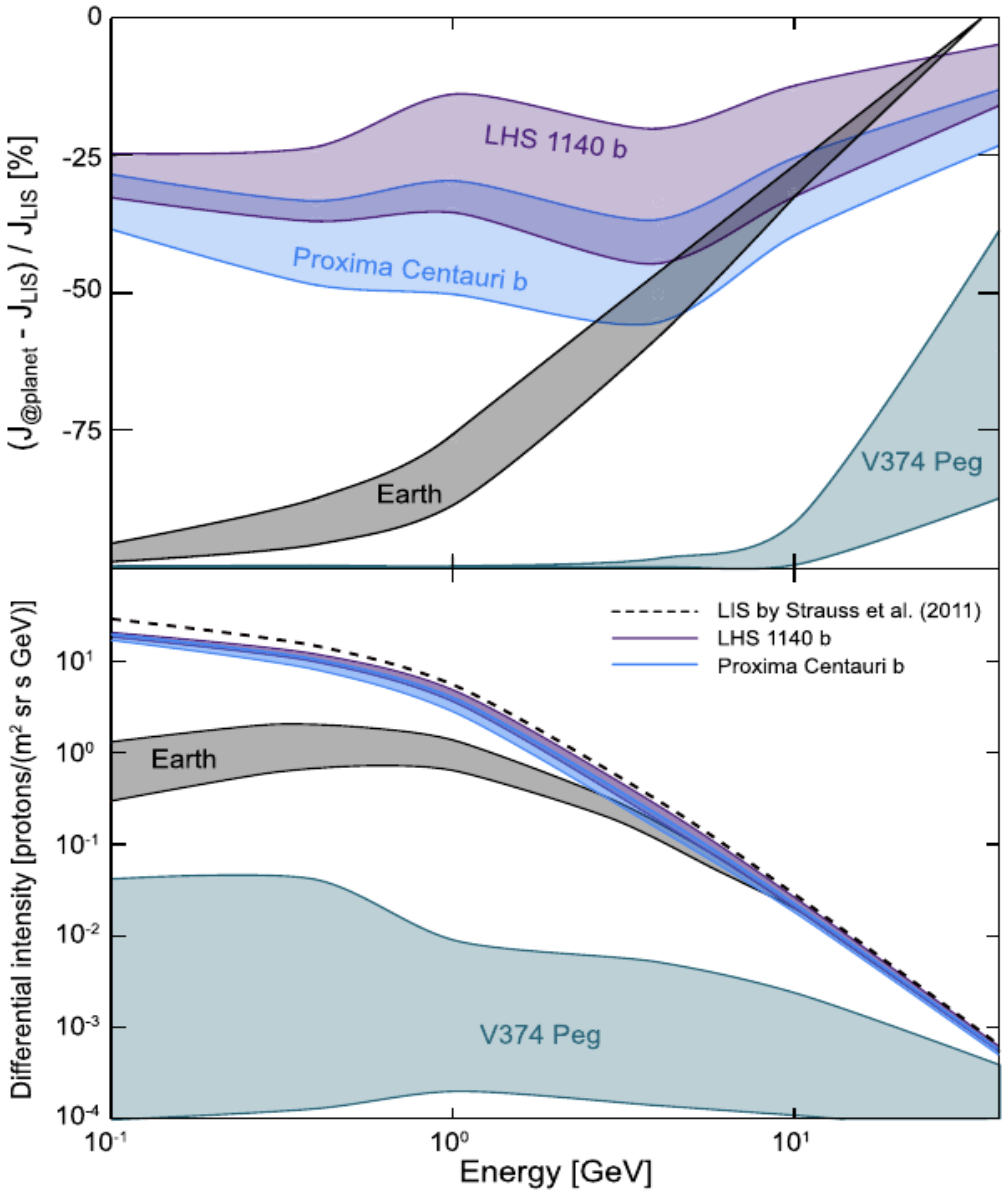

Figure 1.6: *The lower panel shows the differential energy spectra inside of the astrosphere and the top panel shows the change in the intensity of the galactic cosmic rays. The black line refers to the heliosphere, the purple line to LHS 1140, the greyish blue line to V374 Pegasi and the light blue line refers to Proxima Centauri. The dark grey sections shows the GCR intensity change (top panel) and the differential intensity (lower panel) of both Earth and V374 Peg. The figure was taken from Herbst et al. (2020).*

earth-like exoplanets and cannot be neglected.

Figure 1.6 was taken from Herbst et al. (2020). The top panel shows the intensity change of the GCRs with reference to the local interstellar spectrum. The differential intensity inside of the different astrospheres is in the bottom panel. The black line refers to the heliosphere, the purple line refers

to LHS 1140, the greyish-blue line to V374 Pegasi and the light blue line refers to Proxima Centauri. If the flux around V374 Pegasi is, for example, 1 GeV particles, it will be suppressed, whereas the effects of the GCRs on the atmospheres of LHS 1140 b, and Proxima Centauri b are stronger than was previously assumed and have to be taken into account when measuring for planetary habitability.

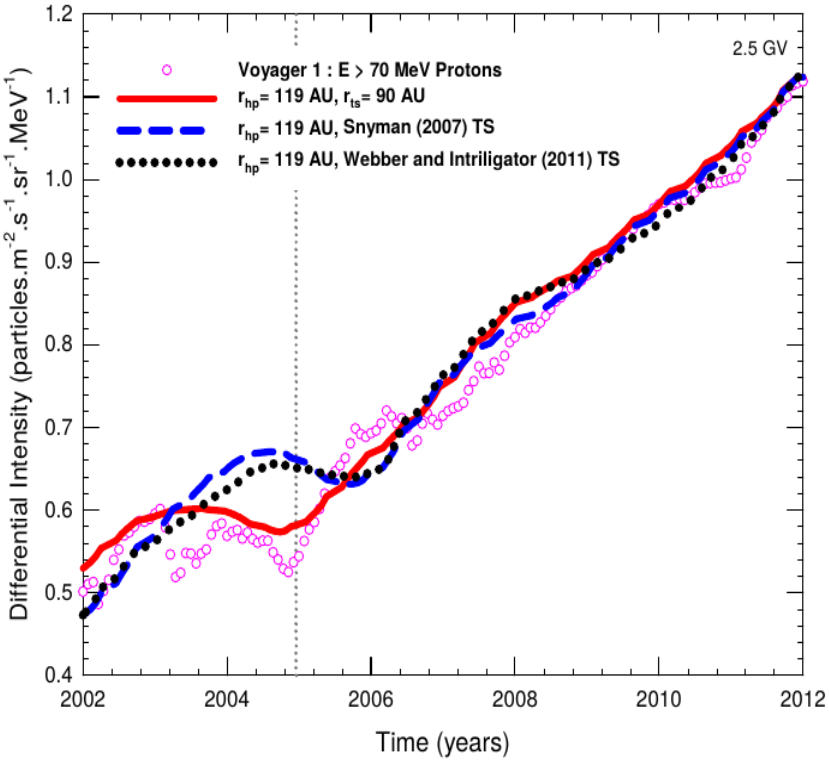

Figure 1.7: *The red line,* r_{ts} *shows the computed cosmic ray intensities corresponding to a static TS position, the blue dashed line is the time-dependence in the TS position as suggested by Snyman (2007) and the black dotted line is the time-dependence in the TS position, as suggested by Webber & Intriligator (2011) and the magenta circles are the differential intensity as measured by Voyager 1. Figure was taken from Manuel (2013).*

Also of interest are time-dependent effects, as was recently studied by, e.g., Moloto et al. (2018). They showed how parameters like the solar wind speed, magnetic field magnitude and tilt angle, and their variation over a solar cycle incorporated in a cosmic ray transport model can successfully simulate cosmic ray variation. Concerning the heliospheric structure, Manuel (2013) reached the conclusion that a dynamic heliosphere has an effect on cosmic ray modulation. He specifically focused on how varying the radius of the TS, suggested by Snyman (2007) and Webber & Intriligator (2011), and the heliopause (HP) may impact cosmic ray modulation in the same direction as both Voyager 1 and 2. The computed results of the cosmic ray intensities were compared to the Voyager proton

observations in Figure 1.7. The TS positions, suggested by Snyman (2007), are time dependent. r_{hp} is the HP radius, and r_{ts} is the static TS position (red line). Computed cosmic ray intensities corresponding to the time dependence in the TS position, as proposed by Snyman (2007), are shown as the blue dashed line and those suggested by Webber & Intriligator (2011) are shown as the black dotted line. His findings demonstrated that variations in the TS position alone are not enough to improve the model's compatibility with the Voyager observations and that an extra time-dependent parameter, such as the HP position, will be needed to improve the results obtained and to ensure compatibility between the numerical model and the observations. The study also proposes that there is a possible ratio between the TS and the HP positions.

Chapter 2

Method

2.1 Two-dimensional HD and MHD simulations

Space plasmas are typically referred to as magnetized fluids in MHD studies, and they obey a set of equations known as the MHD equations. For an in-depth discussion and derivation of these equations, see Choudhuri (1998) or McGreivy (2017). The equations are,

$$\frac{\partial \rho}{\partial t} + \nabla \cdot (\rho \vec{v}) = 0, \tag{2.1}$$

$$\frac{\partial (\rho \vec{v})}{\partial t} + \nabla \cdot (\rho \vec{v} \otimes \vec{v} + P^* \mathbf{I} - \frac{1}{4\pi} \vec{B} \otimes \vec{B}) = 0, \tag{2.2}$$

$$\frac{\partial e}{\partial t} + \nabla \cdot [(e + P^*)\vec{v} - \frac{1}{4\pi} \vec{B}(\vec{B} \cdot \vec{v})] = -n_e n_H \Lambda(T), \tag{2.3}$$

$$\frac{\partial \vec{B}}{\partial t} + \nabla \times (\vec{B} \times \vec{v}) = 0, \tag{2.4}$$

$$\nabla \cdot \vec{B} = 0. \tag{2.5}$$

The variables are defined as follows: ρ defines the density, $\vec{v}$ the velocity, $\vec{B}$ the magnetic field, $P^* = P + \frac{\vec{B}^2}{8\pi}$ describes the total pressure of the ISM, $\mathbf{I}$ is a unit matrix and $\otimes$ is a dyadic product.

Equation (2.1) describes the conservation of mass (ρ), equation (2.2) the conservation of momentum ($\rho\vec{v}$) and equation (2.3) the conservation of energy (e). Equation (2.4) is the induction equation, with equation (2.5) a necessary requirement to ensure a divergence free magnetic field in the numerical model. Should the magnetic field be equal to zero, then the MHD equations reduce to the simpler hydrodynamic equations (HD equations). The total pressure P^* is equal to the thermal pressure P of the gas plus the square of the magnetic field $\vec{B}^2$, known as the magnetic pressure, divided by 8π. By

making use of the ideal gas law, the total energy, with γ the adiabatic index ($\gamma = \frac{5}{3}$, treats protons as mono-atomic gas), can be written as

$$e = \frac{\rho\,|\vec{v}|^2}{2} + \frac{P}{\gamma - 1} + \frac{\vec{B}^2}{8\pi}. \tag{2.6}$$

In equation 2.3, n_e and n_H are the electron density and proton density, respectively, with $\Lambda(T)$ the cooling efficiency. This equation describes the radiative cooling, which is included in one of the numerical models that is used in this work. A full discussion regarding radiative cooling can be found in Dalgarno & McCray (1972). During radiative cooling, a partially ionized gas cools and its thermal kinetic energy is converted, by collisional processes, into radiation. For an optically thin environment, the excited atom radiates the gained energy away through a photon, allowing the photon to escape and thus decreasing the environment's total thermal kinetic energy (Dalgarno & McCray 1972).

In this chapter, the two numerical models used in this work are discussed. For the simulation of the astrospheric expansion of a stellar wind cavity into the ISM, the two-dimensional spherical HD and MHD model of Fahr et al. (2000), Scherer & Ferreira (2005) and Ferreira & de Jager (2008) will be used in Chapter 3. This model was also recently used by van der Schyff (2016) and Light (2017). For additional information on the model, parameters and boundary conditions see Ferreira & de Jager (2008). In Chapters 4 and 5, a modified version of the Pen et al. (2003) three-dimensional cartesian MHD model will be used. This model is similar to the one used by Strauss (2013), see also Strauss & Effenberger (2017), to calculate the heliospheric geometry. This model is discussed later on in this chapter in section 2.2.

The original HD model of Fahr et al. (2000) was expanded to an MHD model by Ferreira & de Jager (2008) to calculate the evolution of pulsar wind nebulae and supernova remnant (SNR) evolution. The authors used the model to investigate the effect that certain parameters have on the evolution of an SNR. These parameters included the ISM density, ejecta mass, adiabatic index, etc. It was established that the SNR reverse shock evenly distributes its time between shifting outward and then back inward. The authors also considered the expansion of an SNR in a non-uniform medium. The results concluded that if an SNR moved into a higher density region, it will lead to the formation of a reflection wave, and that if the SNR blast wave propagates from an area of higher density to a lower density area, the high density medium geometry changes and a second reverse shock starts to form. For similar case studies, see also Vorster et al. (2013).

Originally, the two-dimensional model of Fahr et al. (2000) was developed to simulate the solar wind interaction with the ISM. van der Schyff (2016) expanded on the extensions of Ferreira & de Jager (2008) and adapted the model to simulate astrospheric expansion. The author included radiative cooling and also adapted the model to simulate the evolution of an astrosphere created by an out-blowing stellar wind. The author mostly focused on the effect that radiative cooling has on the astrospheric expansion of O-and B-type stars. To show how the evolution of a cavity can be affected by radiative cooling, simulations were done with three different cooling functions and the results were compared to each other. It was concluded that the choice of cooling function is important as it influences the position and the compression ratios of the TS, AP and BS. He also investigated the evolution of SNRs in the ISM using this model.

The model was later on used by Light (2017), who extended it to include periodic fluctuations in the outflow velocity and the stellar wind density at the star's inner boundary, see also Light et al. (2022). He showed that the periodic fluctuations in the oscillations in the number density influence the space between the TS and the inner boundary. Another topic investigated by Light (2017) was the effect that the ISM magnetic field and radiative cooling have on the astrosphere created around LBV HD 99953. He found that the addition of radiative cooling leads to the creation of a thin but very dense shell that surrounds the astrosphere. This, in turn, influences the density, compression ratio and the position of the TS and the BS, while the ISM magnetic field allows the OAS to decompress faster. He also considered another star, namely AG Carinae. His research on this star specifically focused on the periodic outflow and the effect that varying the stellar parameters periodically will have on the astrosphere's evolution. He showed that an astrosphere with a periodic inner boundary will typically be the size in between what is expected when one assumes maximum speed and density parameters. There were, however, no noticeable time-dependent changes in the OAS thickness over the simulation time period for the periodic astrosphere of AG Carinae.

Figure 2.1, taken from Light (2017), shows how an astrosphere with an eruptive event, which lasted for a 100 years, evolves. The computed density profile is plotted as a function of distance for a simulation time of 100 000, 150 000, 200 000 and 250 000 years. For the other model parameters, see Light (2017). During an eruptive event, large quantities of matter are ejected by an LBV-type star. As time passed, the mass-loss rate increased from 1×10^{-6} $M_{\odot}\,year^{-1}$ (green line) to 1×10^{-4} $M_{\odot}\,year^{-1}$ (blue line) and then to 1×10^{-3} $M_{\odot}\,year^{-1}$ (orange line). At 100 000 years, for a high mass-loss rate, the BS moved further away from the inner boundary. This was the only observable effect on the astrosphere's outer structure. For the inner structure, the eruptive event led to the

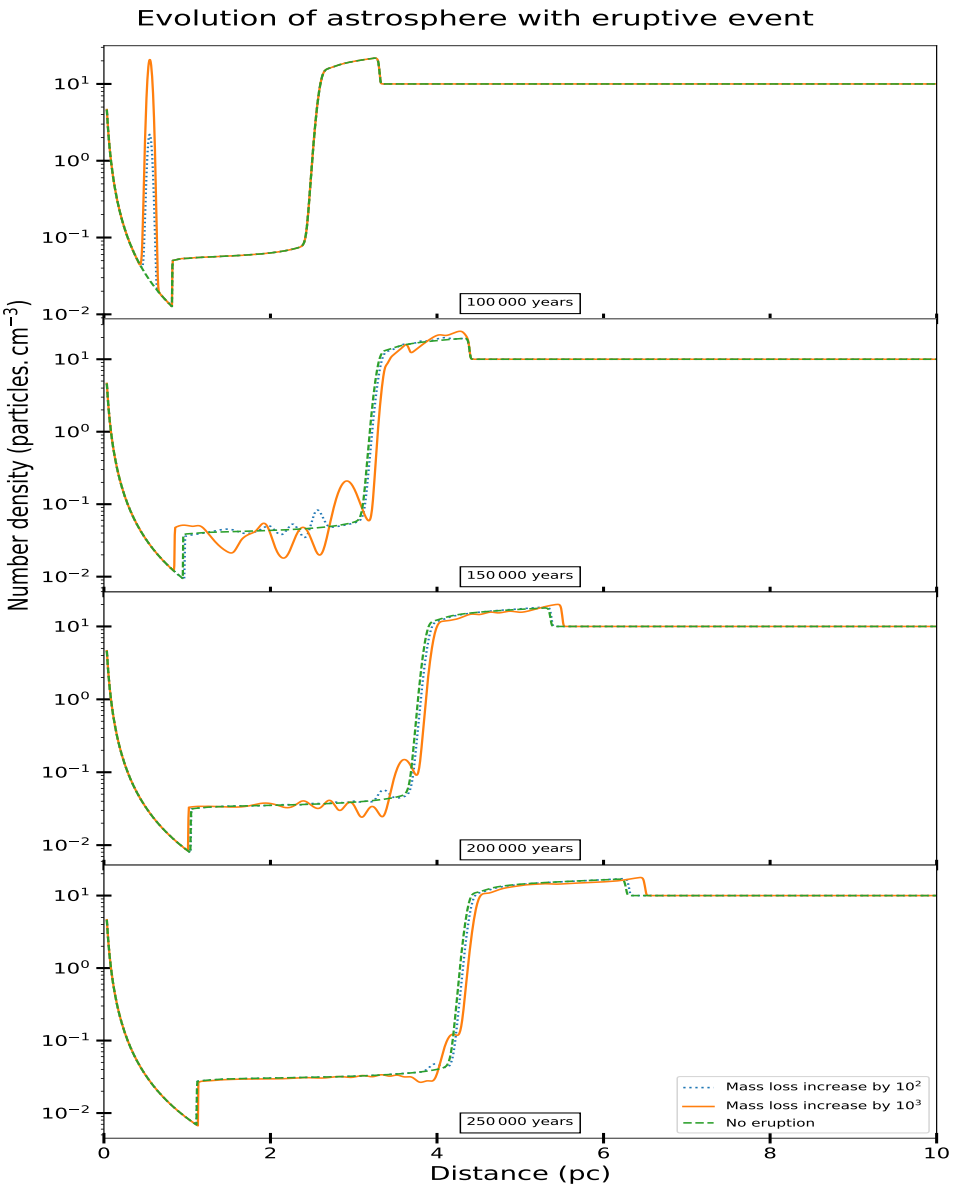

Figure 2.1: *Illustration of how an eruptive event influences the astrospheric evolution by increasing the mass-loss rate. The number density is shown as a function of the distance from the inner boundary. The blue dot line shows a* 10^2 *increase in the mass-loss rate and the orange line shows a* 10^3 *increase, which can be compared to the no eruption scenario (green line). Figure was taken from Light (2017).*

creation of a wave. The wave was continuously reflected between the TS and the inner boundary, causing oscillations.

As shown by both van der Schyff (2016) and Light (2017), radiative cooling has an effect on the density and the compression ratio of the OAS. Radiative cooling also affects the position and the compression ratio of the TS and the BS. For simulations including cooling, the compression ratio of the BS increases. At early stages of evolution, with the inclusion of cooling, the thermal pressure

in both the IAS and the OAS decreases pushing the stellar wind deeper into the ISM, reducing the OAS to a thin but dense structure. To counteract the increase in compression caused by the drop in thermal pressure, the density of the OAS increases. Once the cavity is cooled, it starts to decompress, allowing the density to decrease as the temperature rises. Including radiative cooling in HD and MHD models will result in the formation of smaller astrospheres when compared to simulations where this process is not considered.

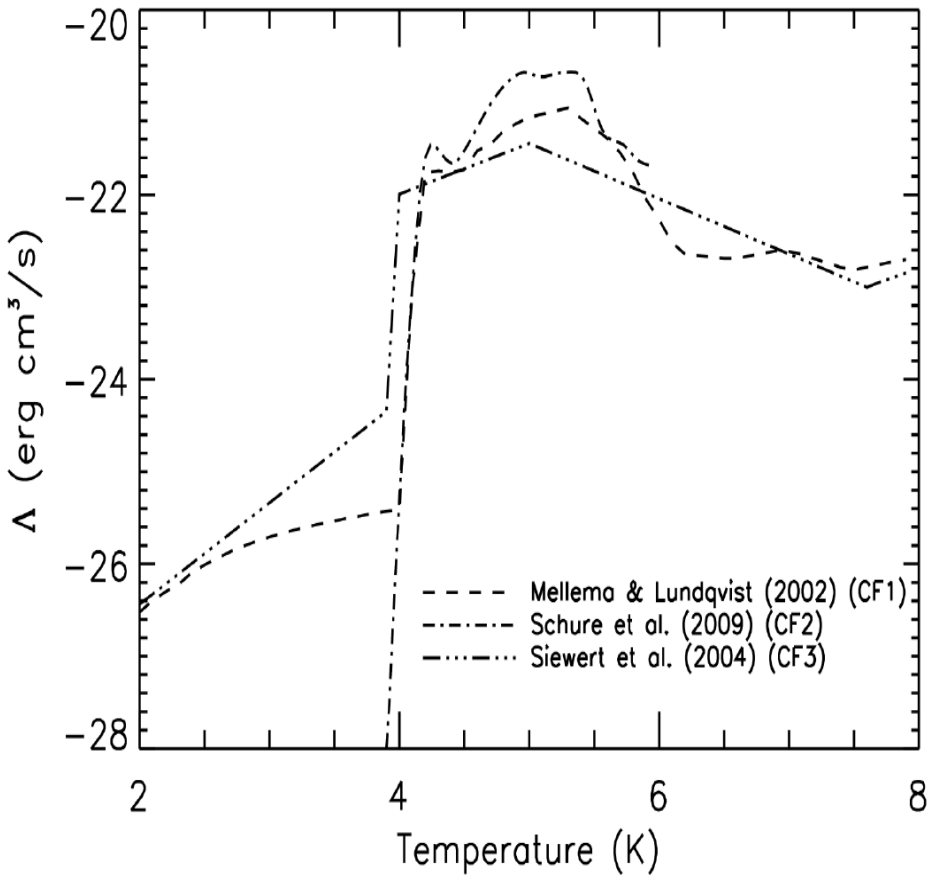

Figure 2.2: *Different cooling functions plotted as a function of the temperature. Figure was taken from van der Schyff (2016).*

A brief summary of the study of van der Schyff (2016) will now be given to better illustrate the effects of cooling. The cooling functions incorporated in the model are displayed in Figure 2.2, taken from van der Schyff (2016). The cooling functions are displayed as a function of the temperature with both axes on a logarithmic scale. The functions used are taken from: dashed line (CF1) - Mellema & Lundqvist (2002), the dot-dashed line (CF2) - Schure et al. (2009) and the dot-dot-dot-dashed line (CF3) - Siewert et al. (2004). In Figure 2.2, the functions CF1 and CF2 are used alongside the assumption of solar abundances, while Siewert et al. (2004) utilized the functions of Dalgarno & McCray (1972)for abundances. In Figure 2.3, however, solar abundances are considered for all three functions.

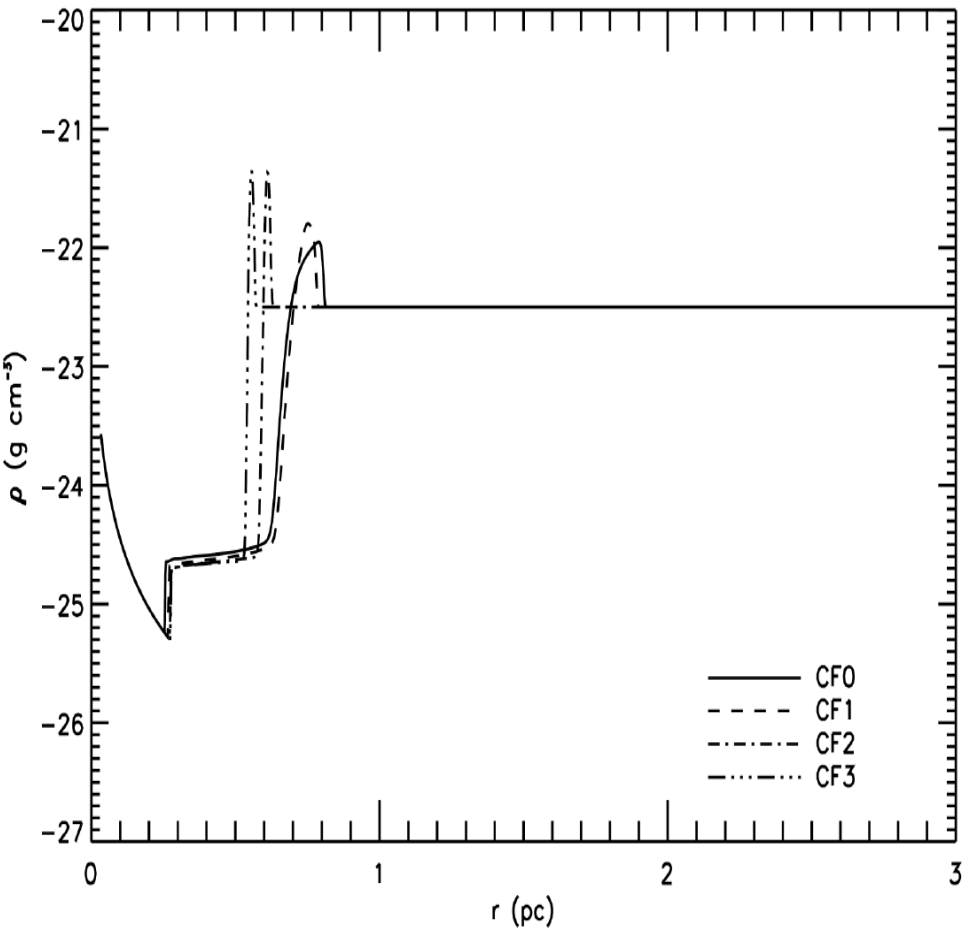

Figure 2.3: *The computed density profile for a pure HD scenario at 5 000 years. The density is plotted on a logarithmic scale. The CF0 line corresponds to a case without cooling, CF1 shows the results of the cooling function from Mellema & Lundqvist (2002), CF2 corresponds to Schure et al. (2009) and CF3 corresponds to Siewert et al. (2004). The figure was taken from van der Schyff (2016).*

The effects of the three cooling functions on cavity evolution are now displayed alongside a pure HD case without cooling. These results are from van der Schyff (2016) and are now briefly summarized. In Figure 2.3, the solid line, CF0, is the pure HD case without cooling, the dashed line is CF1, the dashed-dot line is CF2 and the dot-dot-dot-dashed line is CF3. For all four cases, there is a minor difference in the position of the TS as well as its compression ratio. The shape, AP size and position for CF0 and CF1 are similar, whereas CF2 and CF3 have a slightly similar shape and OAS size. With CF3, the astrosphere cools quickly and has a higher density and BS compression ratio than the astrospheres computed with CF1. CF2 allows the astrosphere to cool over a slightly longer period than CF3, leading to a bigger astrosphere, but essentially has the same BS compression ratio and OAS size. The main difference between the scenario without cooling and CF1 is the size of the

OAS and the BS compression ratio, which is larger for the astrosphere with cooling (CF1).

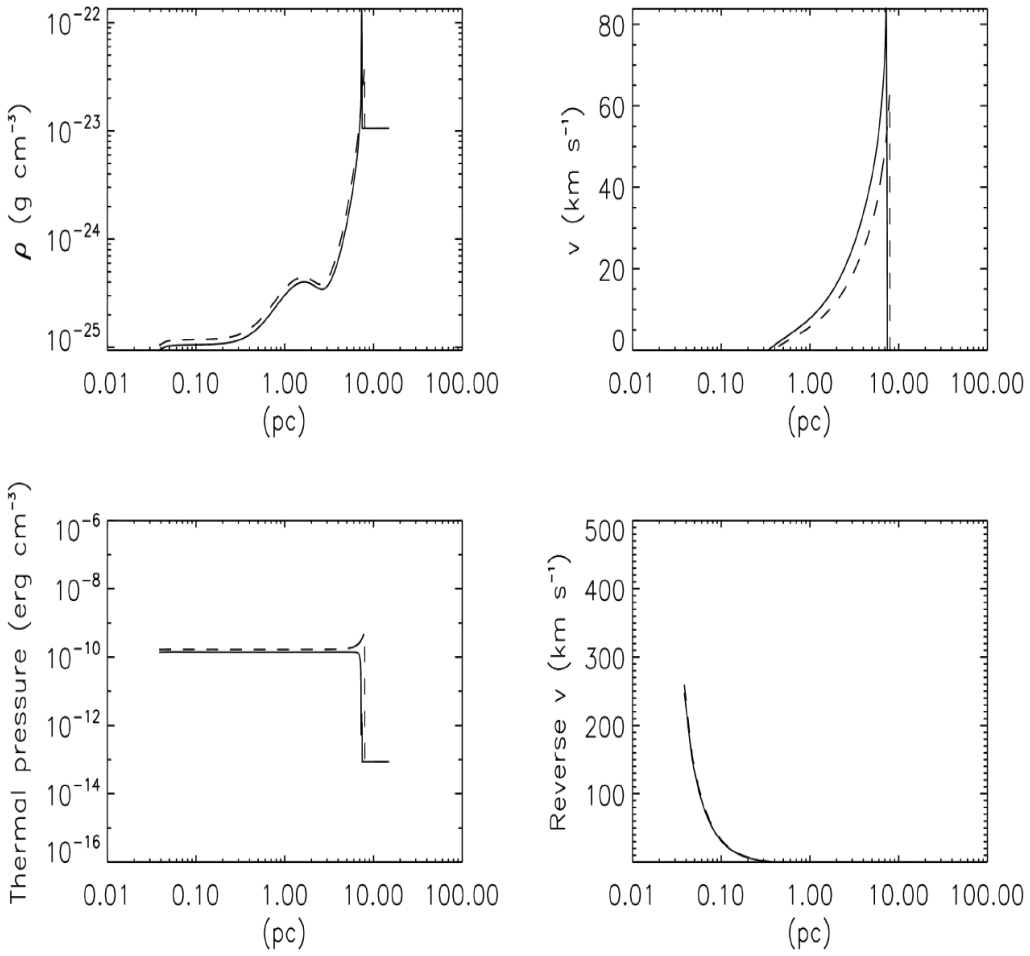

Figure 2.4: *The figure shows an example of how cooling affects the astrospheric evolution of an SNR. The density, thermal pressure, outward and backward bulk velocity are plotted as a function of distance from the inner boundary at 38 000 years simulation time. The parameters are computed in a uniform ISM. An ISM magnetic field and relative motion are not included. The solid line and the dashed line show the results including and excluding radiative cooling, respectively. The figure was taken from van der Schyff (2016).*

Figure 2.4, also taken from van der Schyff (2016), gives an example of the effects of cooling and how it affects the astrospheric evolution of an SNR. The assumed ISM density is 1.05×10^{-23} g cm^{-3}. Relative speed and an ISM magnetic field are not included. The computed profiles of the density, thermal pressure, outward and backward bulk velocity are plotted as a function of distance from the inner boundary at 38 000 years. The solid line and the dashed line give the cases including and excluding radiative cooling, respectively. For the case with cooling, the forward shock (FS) region is more compressed than that of the other case, and from the thermal pressure profile it is visible that

the FS moves closer towards the centre. This is due to cooling. It causes a loss in thermal pressure at the FS and, in order to rectify, moves towards the centre.

2.2 Three-dimensional MHD simulations

As mentioned above, the two-dimensional model of Fahr et al. (2000) was originally used to simulate the heliosphere. For the heliosphere, there are, however, various complex other three-dimensional models available, such as those of Pogorelov et al. (2008), Opher et al. (2009) and Izmodenov & Alexashov (2015) to name a few. For stellar wind results, see the numerical calculations by, e.g. Mohamed & Aydil (2022).

For Chapters 4 and 5, a three-dimensional cartesian MHD model without the effect of radiative cooling will be used. In this model, Pen et al. (2003) proposed a three-dimensional MHD solver that makes use of a total variation diminishing (TVD) scheme. The TVD scheme is taken from Jin & Xin (1995) and updates the fluid variables across all directions (Pen et al. 2003). For additional information on the TVD scheme see Toro (2009) and Gottlieb & Shu (1998). For the model to be accurate, the $\nabla \cdot \vec{B} = 0$ constraint has to be enforced, and this is done by making use of the Evans & Hawley (1988) CT (constrained transport) approach. The MHD equations are solved on a three-dimensional cartesian grid. The magnetic field is specified at the cell faces and the fluid variables at the cell centres.

Figure 2.5, taken from Strauss (2013), shows simulations of the heliosphere using the MHD model of Pen et al. (2003). This shows that the model is able to successfully compute a three-dimensional astrosphere. Panel a) shows the density, ρ, panel b) the speed, $|\vec{v}|$, panel c) the heliospheric magnetic field (HMF), $\left|\vec{B}\right|$ and panel d) the temperature, T. The ISM "moves" from right to left and the trajectories of the two Voyager spacecrafts, V1 and V2, are also shown. Both V1 (Voyager 1) and V2 (Voyager 2) are projected onto the same plane. At approximately 200 AU from the Sun, a BS is created. This BS forms in the nose direction (Strauss 2013), and for the heliosphere, the BS is somewhat controversial. McComas et al. (2012) argued that the ISM flow may be subsonic, resulting in a significantly bigger bow wave region taking the place of the BS. However, as shown by Pogorelov et al. (2009), even if, at first, the flow of the ISM is supersonic, if the ISM magnetic pressure is increased, the creation of the BS can be hindered.

The HP, which separates the interstellar material from the solar material, is found at $\sim$ 100 AU from the Sun, as shown in Figure 2.6 (Strauss 2013). Here the results are now shown as radial profiles. Close to the equatorial plane, the HP is particularly distinct in the $|\vec{v}|$ profiles. There the ISM flow diminishes to nearly zero at the HP to reach zero at the stagnation point. The outer heliosheath is the area connecting the BS to the HP. It was concluded later on that V1 crossed the HP on 25

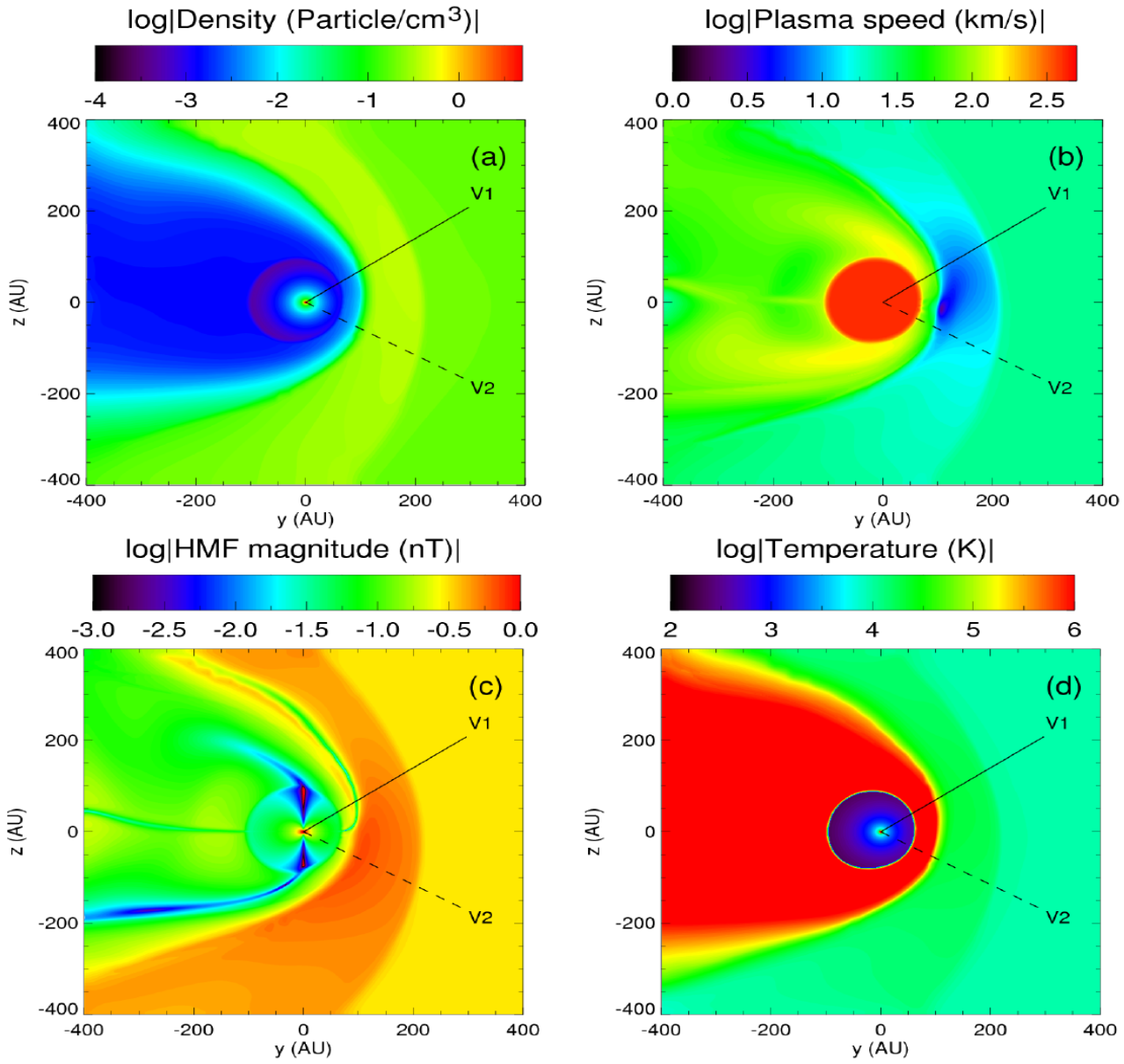

Figure 2.5: *The computed heliospheric geometry. Panel a) is given in terms of the density ρ, panel b) in terms of the speed $|\vec{v}|$, panel c) in terms of the heliospheric magnetic field (HMF) $\left|\vec{B}\right|$ and panel d) is given in terms of the temperature T. The trajectories of both Voyager 1 and Voyager 2 spacecraft are shown. Figure was taken from Strauss (2013).*

August 2012, entering interstellar space with V2 crossing the HP on 5 November in 2018 (Croswell 2021). The TS is found in the equatorial plane at ~ 75 AU. At this distance, the solar wind decreases from supersonic to subsonic speeds. When crossing the TS, it was observed by V1 that the TS has a compression ratio of ~ 2, which is much weaker than ~ 4, which was the expected maximum value (Richardson et al. 2008).

The crossing of the TS by both of the Voyager spacecrafts exposed a north-south geometrical

asymmetry of the heliosphere (Pogorelov et al. 2007). One possible explanation is shown in Figure 2.5, panel c), illustrating that the ISM magnetic field orientation can be the cause of the asymmetry. Close to the HP in the southern hemisphere, the heliosphere is more compressed. This is due to the ISM magnetic field piling up in that region, causing more magnetic pressure to be exerted and basically compressing that specific hemisphere. Also seen is the upward deflected tail region (Pogorelov et al. 2007). Similar results for an astrospheric cavity will be presented in Chapters 4 and 5.

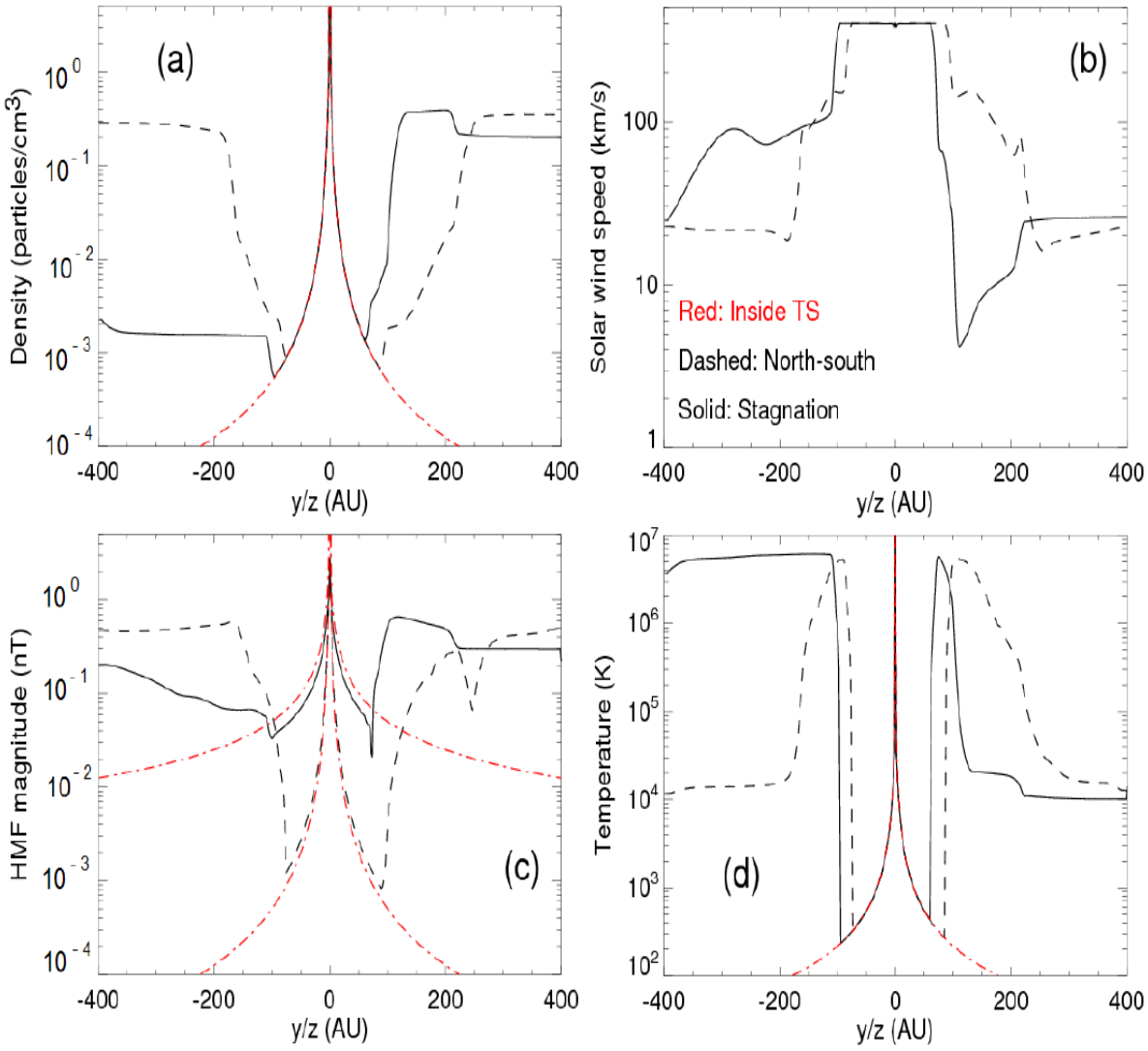

Figure 2.6: *Illustrates the plasma properties of Figure 2.5 as radial profiles. The stagnation line corresponds to the solid line and the north-south cut to the dashed line. The stagnation line is along the y-axis and the north-south cut is along the z-axis. The red lines illustrate the profiles inside the TS. Panel c shows the HMF in the polar regions and in the equatorial regions. Figure was taken from Strauss (2013).*

In Figure 2.6, four different parameters are shown as radial profiles along the y-and z-axes. Panel

a) shows the density, panel b) the solar wind speed, panel c) the HMF magnitude and panel d) shows the temperature as a function of distance. A summary of the results is given, but a full discussion can be found in Strauss (2013). The stagnation line corresponds to the solid line and the north-south cut to the dashed line. The stagnation line is along the y-axis and the north-south cut is along the z-axis. The red lines illustrate the computed profiles inside the TS. Inside the TS, the density is proportional to $1/r^2$ and panel a) shows the anticipated decrease inside the TS up to the shock, which has a compression ratio of ~ 4, and then followed with a region of constant density thereafter. In the nose direction, compression can also be seen at the BS.

Panel a) illustrates the asymmetry of the TS previously mentioned. There are two asymmetries to be noted. The first is the nose-tail asymmetry and the second is the north-south asymmetry. For the north-south asymmetry, the TS is found at ~ 75 AU and ~ 100 AU in the southern and northern hemisphere, respectively. As for the nose-tail asymmetry, the TS is found at ~ 75 AU and ~ 100 AU in the nose and the tail region, respectively (Strauss 2013). The wind speed profiles $|\vec{v}|$, panel c), exhibit similar behaviour. For panel c), the heliospheric current sheet (HCS) is also seen in the results. In the northern hemisphere, there is a decrease in the HMF ($\left|\vec{B}\right|$) at ~ 250 AU. The HMF also decreases just past the TS. Panel d), which gives the temperature profile, shows how the plasma is heated. This takes place at the BS and the TS.

2.3 Summary

In this chapter, the two-dimensional HD and MHD model used in Chapter 3, and the three-dimensional cartesian MHD model used in Chapters 4 and 5 were discussed. The two-dimensional HD and MHD model of Fahr et al. (2000), Scherer & Ferreira (2005) and Ferreira & de Jager (2008) were used and adapted by van der Schyff (2016) and Light (2017). van der Schyff (2016) adapted the model to include radiative cooling. He simulated the effects that different cooling functions had on O-and B-type stars as well as the evolution of SNRs in the ISM. He found that the choice of cooling function was important as it influenced the position and the compression ratios of the TS, AP and the BS. Light (2017) and Light et al. (2022) later on modified the model to include periodic fluctuations in the outflow velocity and the stellar wind density at the inner boundary. During the author's study, he considered the effects that radiative cooling and the ISM magnetic field as well as varying these parameters periodically may have on the evolution of an astrosphere around two stars, namely LBV HD and AG carinae. He concluded that an astrosphere with a periodic inner boundary will most likely be the size in between what is expected when maximum or minimum density and speed parameters are assumed. Light (2017) also showed the evolution of an astrosphere with an eruptive event. Both he and van der Schyff (2016) showed that the compression ratio was dependent on various parameters including the ISM density. In this work, the model is used in Chapter 3.

The three-dimensional cartesian model to be used in Chapters 4 and 5 was also discussed. In this model, Pen et al. (2003) proposed a three-dimensional MHD solver that makes use of a TVD scheme. The model of Pen et al. (2003) was first used by Strauss (2013) to simulate the heliosphere. The author discussed the TS, BS and the HP and explained his results by means of comparison with the observations made by the Voyager spacecrafts. Also discussed by him was the important role that the heliospheric and the astrospheric structures played in, e.g. the modulation of cosmic rays over time. Also briefly mentioned in this chapter was the study of Manuel (2013). He showed that a dynamic heliospheric geometry has an effect on cosmic ray modulation and showed that varying the radius of the TS and the HP may impact cosmic ray modulation.

Chapter 3

Astrospheric expansion

3.1 Introduction

In this chapter, the effects of varying the mass-loss rate, ISM density and the ISM magnetic field have on the evolution of an astrosphere will be studied. Results will be presented for a pure two-dimensional hydrodynamic case and for an MHD case, both including and excluding radiative cooling. Different scenarios are necessary in order to understand the sensitivity of model results to these different parameters. This chapter only includes radial plots. For plots of temperature and velocity on similar scenarios see van der Schyff (2016). The resolution of simulations are discussed in detail in the next chapter.

3.2 The effect of different mass-loss rates on astrospheric evolution

This section will illustrate the effect that the mass-loss rate has on astrospheric evolution. In this section, a mass-loss rate (amount of mass ejected from the star) of 3.27×10^{-6} $M_{\odot}\,year^{-1}$ is used at the model's inner boundary, which is set as 0.032 pc with the inner boundary of the astrsophere also taken to be the star's radius. The outflow velocity is 1500 $km\,s^{-1}$ and the ISM density is 1.6726×10^{-23} $g\,cm^{-3}$. Radiative cooling is included unless stated otherwise, and the ISM magnetic field strength is 3×10^{-6} G. These parameters form the standard or default scenario, will be referred to as standard throughout this study, and will remain the same throughout this chapter, unless otherwise indicated. For all of the computed density profiles, the density is plotted on a logarithmic scale in order to highlight different structures, such as the termination shock (TS) and the heliopause (HP). Note, that for all of the density profiles throughout this study, the computed density is plotted as a function of the distance from the inner boundary.

Figure 3.1 shows a computed astrosphere after 20 000 years of simulation time. The formation of the TS and the astropause (AP: contact discontinuity between the ISM and the stellar wind) is

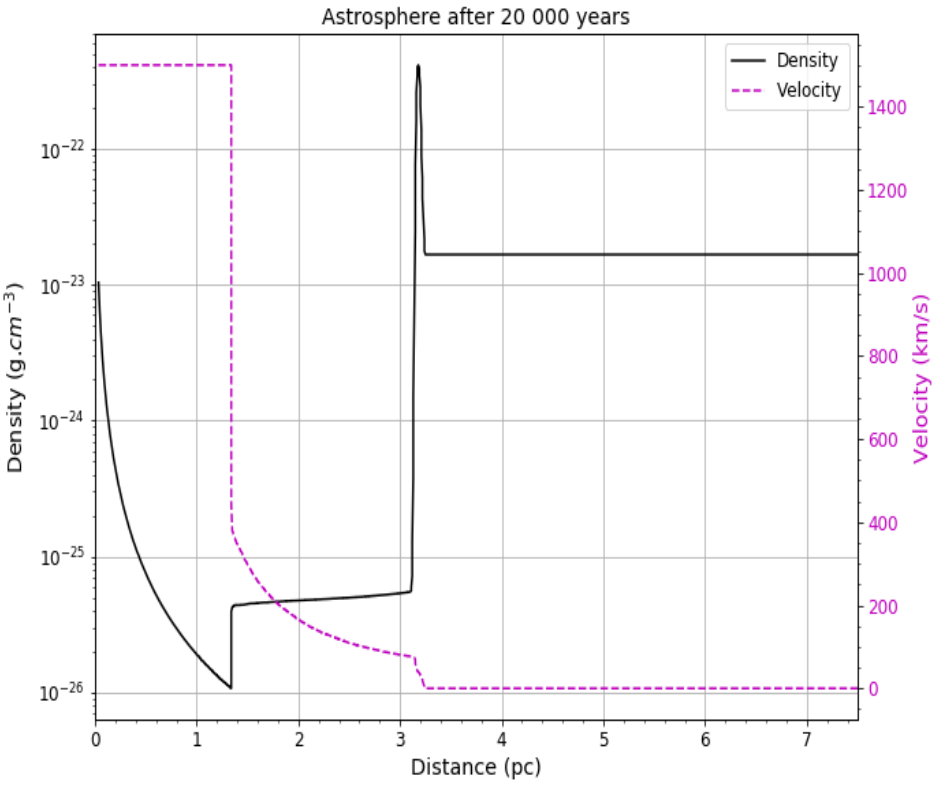

Figure 3.1: *The computed radial profile shows the density as a function of distance (solid black line) and the velocity as a function of distance after 20 000 years (purple line). The computed astrosphere was modelled for a mass-loss rate of* 3.27×10^{-6} $\mathrm{M}_{\odot}\,\mathrm{year}^{-1}$ *and an ISM density of* 1.6726×10^{-23} $\mathrm{g\,cm}^{-3}$. *This is a pure hydrodynamic case as no magnetic field is included.*

due to the stellar interaction with the ISM. The outflow velocity decreases at the TS from a super to a subsonic flow. At the TS, the density increases and then stays constant up to the AP due to incompressible subsonic flow in this region. Although not visible here, after the TS, the kinetic energy is converted into thermal energy, which results in a temperature increase after the TS. The BS forms when there is motion between the astrosphere and ISM or due to the expansion of the astrosphere into the ISM. The OAS is heated by the shocked ISM as the BS moves over it.

Figure 3.2 shows the density as a function of distance for three different mass-loss rate scenarios. The black line is the standard mass-loss rate scenario of 3.27×10^{-6} $\mathrm{M}_{\odot}\,\mathrm{year}^{-1}$, the green line is half the standard mass-loss rate, 1.635×10^{-6} $\mathrm{M}_{\odot}\,\mathrm{year}^{-1}$, and the red line is double the standard mass-loss rate, 6.54×10^{-6} $\mathrm{M}_{\odot}\,\mathrm{year}^{-1}$.

Comparing the black line of the standard mass-loss rate with the red line (double the standard

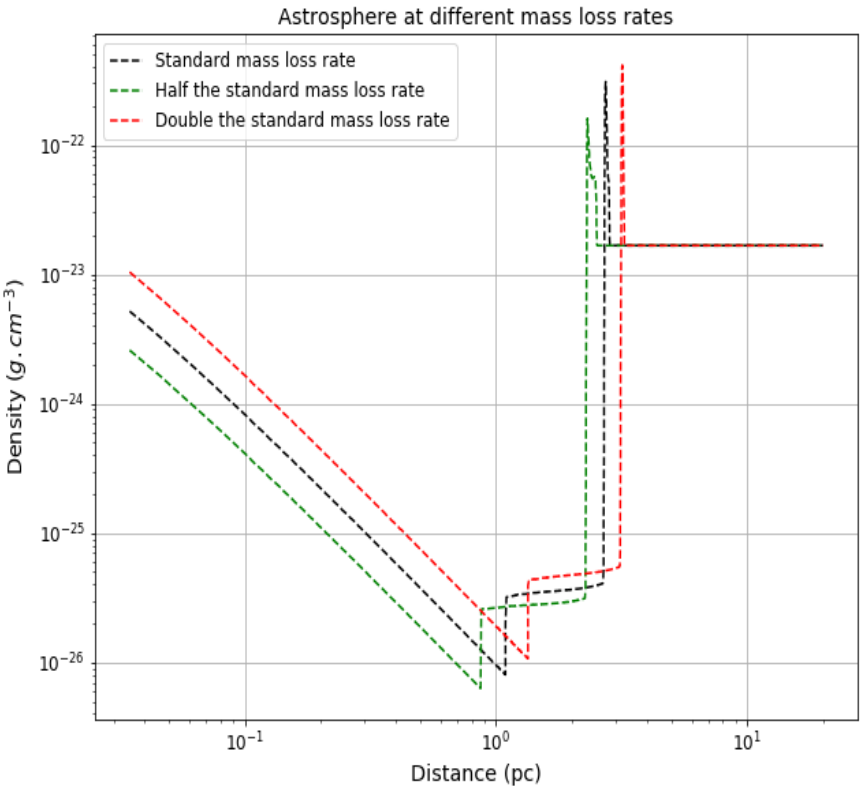

Figure 3.2: *The graph shows the computed density plotted against the distance at 40 000 years for an astrosphere corresponding to three different mass-loss rate scenarios. Radiative cooling is included and the magnetic field is excluded. The black line is the standard mass-loss rate scenario of* 3.27×10^{-6} $M_{\odot}\,year^{-1}$*, the green line is half the standard mass-loss rate* 1.635×10^{-6} $M_{\odot}\,year^{-1}$ *and the red line is double the standard mass-loss rate* 6.54×10^{-6} $M_{\odot}\,year^{-1}$*. The x and the y axis are plotted on a logarithmic scale to show the discernible difference in density for the different scenarios.*

mass-loss rate), there is a noticeable increase of $\sim 32.7\%$ in the density of the outer shell for the higher mass-loss rate. For a higher mass-loss rate, the ram pressure is larger, leading to a larger computed astrosphere as compared to a lower mass-loss rate scenario for the same simulation time. The larger cavity resulted in a thinner but more dense outer shell. When comparing the astrosphere computed from the standard mass-loss rate to the astrosphere computed from half the standard mass-loss rate (green line), the opposite happens for a lower mass-loss rate than for a higher mass-loss rate. For a lower mass-loss rate, there is a decrease of $\sim 48.2\%$ in the density of the outer shell, which causes a temperature increase as lower density areas lose less energy than the surrounding areas. This, in turn, leads to an increase in the local pressure.

The variation in the mass-loss rate leads to a shift in the stellar wind's ram pressure, which is

given by:

$$P_{ram} = \frac{1}{2}\rho v^2. \tag{3.1}$$

With v the bulk speed and ρ the stellar wind density, which is proportional to the mass-loss rate ($\dot{M}$), it is also known that,

$$\rho = \frac{\dot{M}}{4\pi r^2 v}, \tag{3.2}$$

where r is the distance and in this case is the astrosphere's inner boundary. From equation 3.2, it follows that an increase in the mass-loss rate of the computed astrosphere will lead to an increase in the ram pressure, which, in turn, leads to an increase in the TS distance. For a smaller mass-loss rate, the overall size of the astrosphere decreases.

For the black line in Figure 3.2 (standard mass-loss rate), the TS is located at a distance of ∼1.1 pc. For the green line (half the standard mass-loss rate), the TS is located at a distance of ∼0.88 pc and the TS for the red line (double the standard mass-loss rate) is located at a distance of ∼1.3 pc. As the mass-loss rate increases the TS moves further away from the inner boundary. The distance between the AP and the TS remains constant, which may change if a magnetic field is included.

As the mass-loss rate varies, so does the BS distance. For this particular case in Figure 3.2, the BS for the black line is located at ∼2.75 pc, for the green line the BS is located at a distance of ∼2.5 pc and for the red line the BS is located at a distance of ∼3.1 pc.

Figure 3.3 shows the same as Figure 3.2, but now for 160 000 years. This figure properly demonstrates the decreases in astrospheric density. Again, the black line is the standard mass-loss rate of 3.27×10^{-6} $M_\odot\,year^{-1}$, the green line is half the standard mass-loss rate 1.635×10^{-6} $M_\odot\,year^{-1}$ and the red line is double the standard mass-loss rate 6.54×10^{-6} $M_\odot\,year^{-1}$. All three scenarios show almost the same compression ratio of the outer shell. At this point in time, the cooling process has already finished and thus there is less of a difference in the compression between the different scenarios at later times. There is, however, a difference in TS and BS positions between the three scenarios. For the black line, standard mass-loss rate, the TS is located at a distance of ∼2 pc and the BS at ∼4.3 pc. For the green line, half the standard mass-loss rate, the TS is located at a distance of ∼1.6 pc and the BS at ∼3.7 pc. The TS for the red line, double the standard mass-loss rate is located at a distance of ∼1.3 pc and the BS at ∼4.9 pc. Comparing Figure 3.2 and Figure 3.3, it is

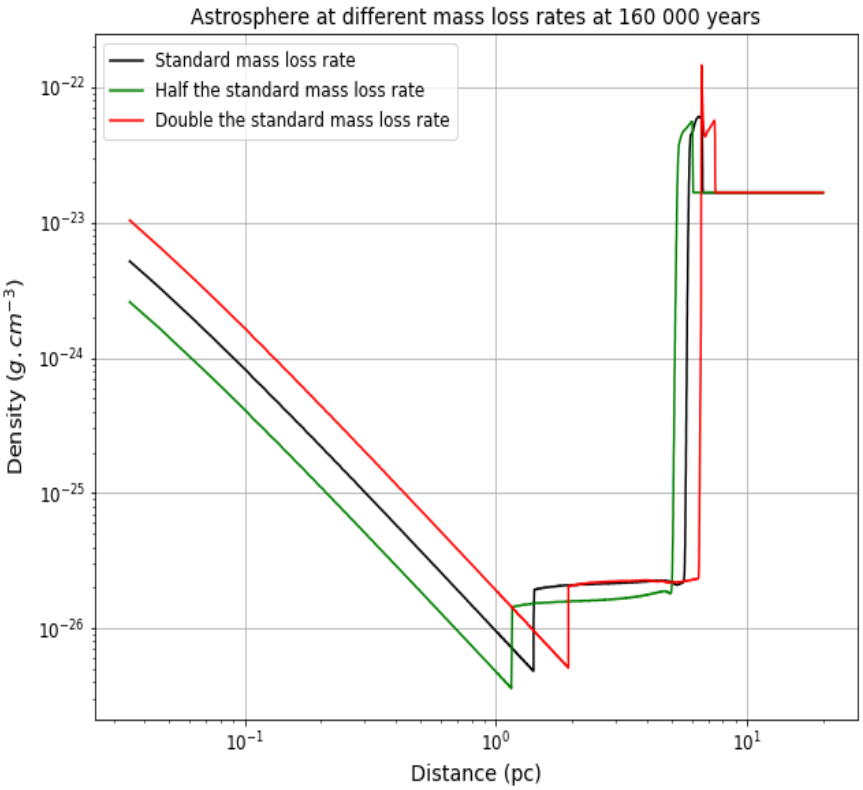

Figure 3.3: *The black line is the standard mass-loss rate scenario of* 3.27×10^{-6} $M_{\odot}\,year^{-1}$*, the green line is half the standard mass-loss rate* 1.635×10^{-6} $M_{\odot}\,year^{-1}$ *and the red line is double the standard mass-loss rate* 6.54×10^{-6} $M_{\odot}\,year^{-1}$.

clear that the time it takes the astrosphere to cool is proportional to the density and that a larger mass-loss rate increases the astrosphere's cooling time.

Figure 3.4 shows the computed compression ratios of the outer shell as a function of time for the three different mass-loss rate scenarios. The black line corresponding to the compression ratio for the model where a standard mass-loss rate of 3.27×10^{-6} $M_{\odot}\,year^{-1}$ is assumed, the green line shows the ratio when half the standard mass-loss rate is assumed in the model and the red line the compression ratio for twice the standard mass-loss rate.

For the standard mass-loss rate, black line, the maximum compression ratio peaks at ∼20 at approximately 45 000 years. At 50 000 years, the double mass-loss rate scenario reaches its peak of ∼ 25 as shown by the red line. For the scenario of half the standard mass-loss rate (green line), the compression ratio reaches its peak of ∼ 16.5 at 25 000 years. For all three the scenarios, the ratio drastically decreases after reaching their different peaks and continues to decrease until it reaches a

value of ~ 4 where it remains constant over time with only slight deviations.

For the astrosphere with a standard mass-loss rate, radiative cooling influences simulations for almost 50 000 years before the fluid is cooled, meaning the outer shell is no longer a thin compressed shell but has expanded and now looks similar to non-cool simulations. For twice the mass-loss rate, the astrosphere is cooled within ~60 000 years and for half the standard mass-loss rate, the astrosphere is cooled within ~30 000 years. This shows that the larger the mass-loss rate, the longer it takes for the outer shell to cool and to decompress.

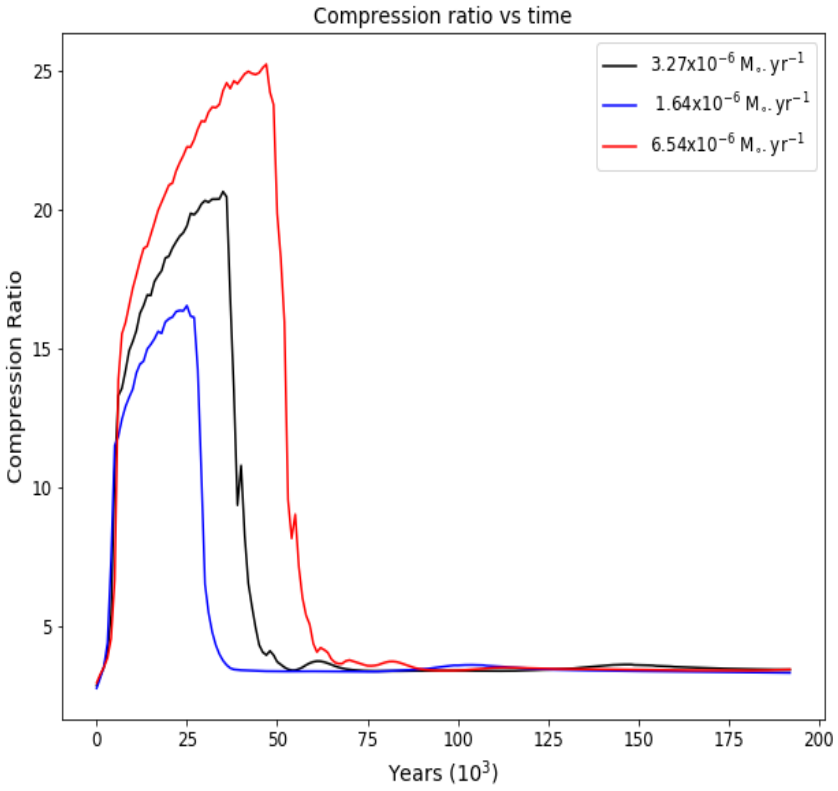

Figure 3.4: *The computed compression ratio of the outer shell (bow shock) as a function of time. The black line corresponds to model calculations assuming a standard mass-loss rate scenario of* 3.27×10^{-6} $M_\odot$ year^{-1}*, the blue line is when half the standard mass-loss rate* 1.635×10^{-6} $M_\odot$ year^{-1} *is assumed in the model and the red line corresponds to double the standard mass-loss rate* 6.54×10^{-6} $M_\odot$ year^{-1}.

3.3 The effect of different ISM densities on astrospheric evolution

In this section, the mass-loss rate is now kept constant at 3.27×10^{-6} $M_{\odot}\,year^{-1}$, with the ISM density being varied. The inner boundary and outflow speed are again 0.032 pc and 1500 $km\,s^{-1}$ respectively and remain the same throughout this section. Radiative cooling is included and the ISM magnetic field strength is 3×10^{-6} G. Figures 3.5, 3.6 and 3.7 will now illustrate what happens to an astrosphere when the ISM density in the model is changed and then compared to the standard/default scenario. It will be shown that this parameter influences the size of the astrosphere. It also affects radiative cooling and therefore leads to different compression ratios in the outer shell.

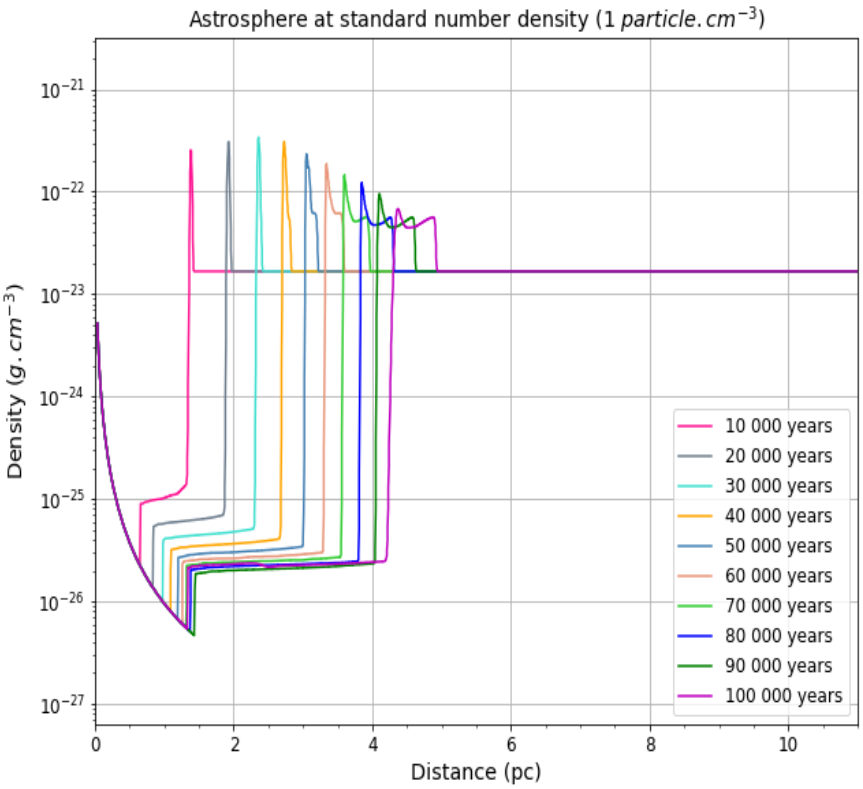

Figure 3.5: *The graph shows the computed density profiles as a function of distance corresponding to different simulation times as shown in the legend. The ISM density in this scenario is assumed to be* 1.6726×10^{-23} $g\,cm^{-3}$ *or 1* particle cm^{-3}.

The standard ISM density scenario of 1.6726×10^{-23} $g\,cm^{-3}$ is shown in Figure 3.5. Here the computed density profile is plotted as a function of distance for 10 different simulation times. The effect that the radiative cooling has on the astrosphere as a function of time is clearly visible. For this density scenario, radiative cooling is compressing the outer shell within the first 40 000 years

where after the compression becomes less as time goes on. At 100 000 years, the outer shell has expanded with a much smaller compression ratio. A double peak-like outer shell has also formed.

For Figure 3.6, the ISM density is now increased to 1.6726×10^{-22} g cm^{-3}. This is 10 times larger than in Figure 3.5. Shown here is that with the increase in density, the astrosphere is much smaller with an increase in compression. The radiative cooling is only visible in early stages. For this larger density scenario, radiative cooling occurs within the first few thousand years and is not as pronounced as at later stages.

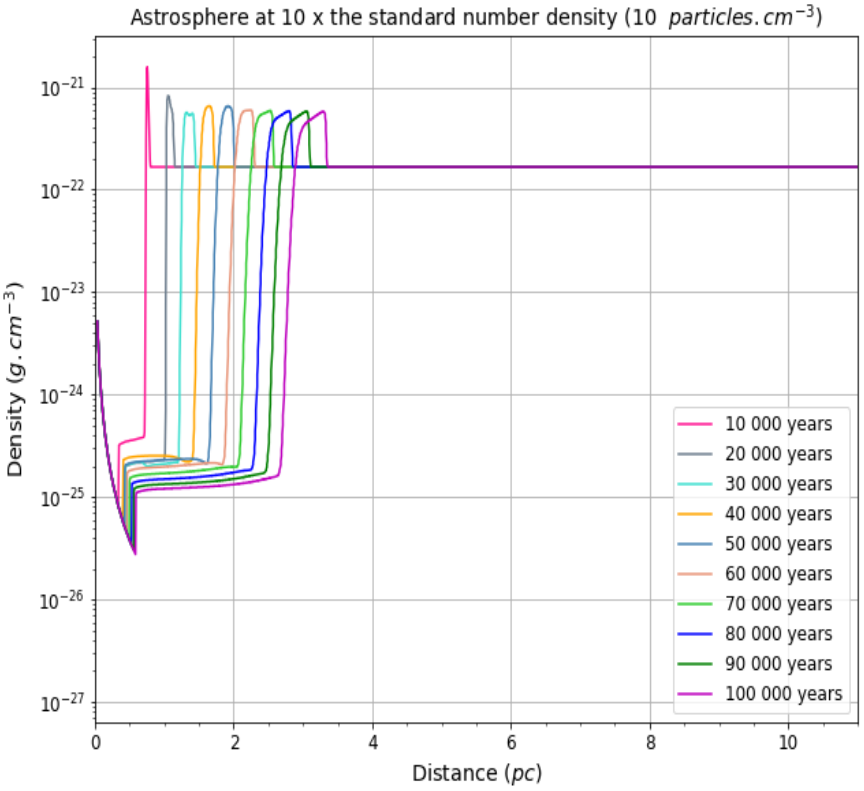

Figure 3.6: *Similar to Figure 3.5. The ISM density in this scenario is increased to be* 1.6726×10^{-22} g cm^{-3} *or 10* particle cm^{-3}.

For Figure 3.7, the ISM density was now decreased to 1.6726×10^{-24} g cm^{-3}. The ISM pressure decreases for a lower ISM density. This results in the TS and AP being further out in distance from the inner boundary. For this lower ISM density scenario, radiative cooling compresses the outer shell over a longer time period. Whereas the scenario with the higher ISM density shows that significant amounts of cooling have already taken place at 40 000 years. For the lower ISM density, the OAS only starts its cooling process around 40 000 years and has considerably cooled by the time the simulation

reaches 60 000 years.

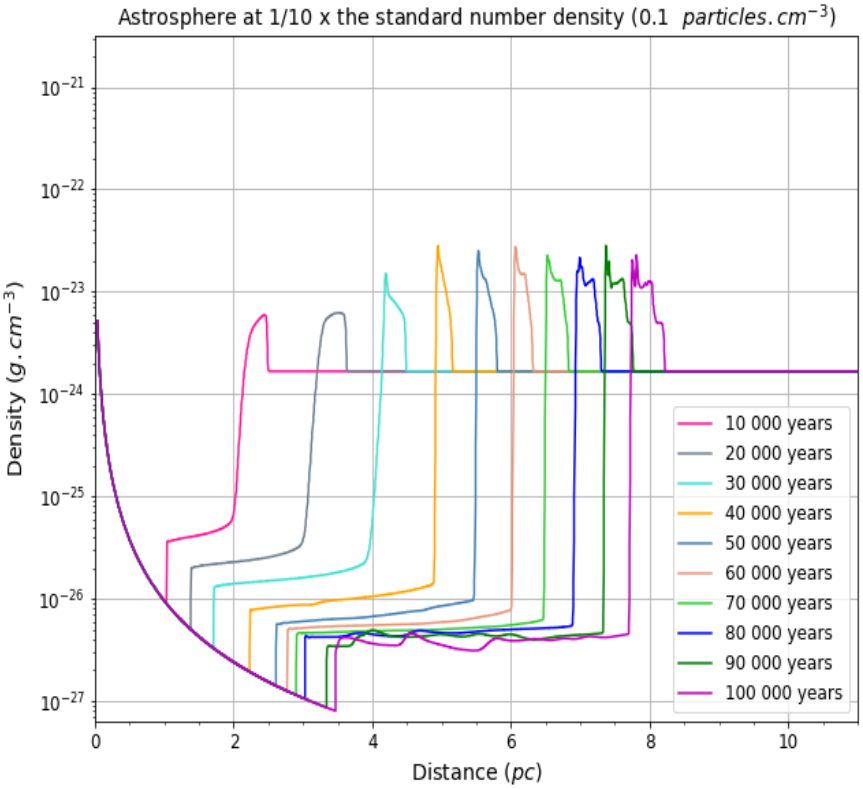

Figure 3.7: *Similar to Figure 3.5 and Figure 3.6. The ISM density in this scenario is assumed to be* 1.6726×10^{-24} g cm^{-3} *or 0.1* particle cm^{-3}.

For the lower ISM density scenarios, a double peak is visible in the outer shell. Due to the radiative cooling, a HOAS and a COAS structure is created. The AP density increases and the effect the ISM magnetic field has on the astrosphere can become more important for a lower ISM density. This will be studied later on in this chapter. As shown in Figures 3.5, 3.6 and 3.7, the higher the ISM density, the smaller the astrosphere becomes and the sooner cooling occurs.

3.4 The effect of different ISM magnetic field strengths on astrospheric evolution

In this section, the effect of different ISM magnetic field strengths on astrospheric evolution will be shown. In Figures 3.8, 3.9 and 3.10, the red line is the standard ISM magnetic field of 3×10^{-6} G that is mostly assumed in this work, the black line is 10 times the standard magnetic field (3×10^{-5} G) and the blue line is 1/10 times the standard magnetic field scenario (3×10^{-7} G). Model results for each of these scenarios are also shown for different ISM densities in the different figures. The mass-loss rate, inner boundary and outflow velocity are 3.27×10^{-6} $M_{\odot}\,year^{-1}$, 0.032 pc and 1500 $km\,s^{-1}$, respectively, and remain the same throughout this section. Radiative cooling is included. As will be shown, the ISM magnetic field pressure will affect the astrosphere's outer structure. Because of the two-dimensional limitation of the model, an azimuthal ISM magnetic field perpendicular to the outflow is assumed. The magnetic pressure affecting the cavity evolution is expected to be a maximum for this orientation. In the next chapter, a more realistic three-dimensional field will be implemented in the three-dimensional model.

In Figure 3.8, the computed radial density profiles as a function of distance for an ISM density of 1.6726×10^{-23} $g\,cm^{-3}$ are shown. Three different scenarios corresponding to the three different ISM magnetic field strengths are shown at 40 000 years simulation time. The red line shows model results corresponding to 3×10^{-6} G, the blue line shows model results corresponding to 3×10^{-7} G and the black line to 3×10^{-5} G. For the standard magnetic field scenario, the TS is located at a distance of $\sim$ 1.1 pc and the BS at $\sim$ 2.7 pc.

As the ISM magnetic field increases, as shown by the black line in Figure 3.8, the TS moves closer to the inner boundary and is located at $\sim$ 0.9 pc, with the BS at $\sim$ 3.2 pc. As for the lower ISM magnetic field scenario, blue line, the TS is located at $\sim$ 1.1 pc and the BS at $\sim$ 2.7 pc. There is no noticeable difference in the position of the TS and the BS of the standard and lower ISM magnetic field. The ISM magnetic field influences the size of the OAS and, in turn, the compression ratio of the BS, as will be better illustrated in Figure 3.11.

As shown in Figure 3.8, the compression, due to radiative cooling, of the ISM is counteracted by the ISM magnetic field. As the magnetic field increases, so does the size of the OAS, which, in turn, decreases the compression ratio of the BS. For the higher ISM magnetic field, the magnetic pressure increases and the AP moves closer to the inner boundary. The structure of the outer shell is also

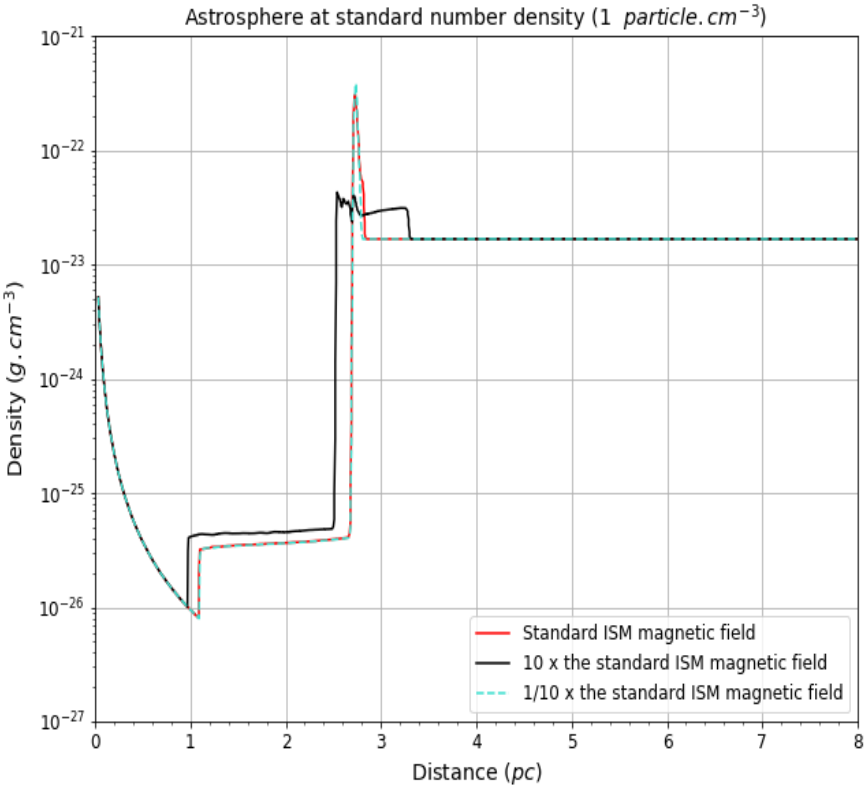

Figure 3.8: *Computed radial density profiles corresponding to different ISM magnetic field strength scenarios are shown as a function of distance for an ISM density of* 1.6726×10^{-23} g cm^{-3} *or 1* particle cm^{-3}. *Three different scenarios are shown corresponding to three different ISM magnetic field strengths. The red line shows the standard magnetic field strength of* 3×10^{-6} G*, the blue line is 1/10 times the standard magnetic field strength (*3×10^{-7} G*) and the black line is double the standard magnetic field strength (*3×10^{-5} G*). Results are shown at 40 000 years simulation time.*

influenced by the increase/decrease of the magnetic pressure, with a lower ISM magnetic pressure resulting in a thinner outer shell.

Figure 3.9 is similar to Figure 3.8, but now the ISM density is assumed to be 1.6726×10^{-22} g cm^{-3}. As mentioned in the previous section, for a higher ISM density, the position of the TS is shifted closer to the inner boundary of the astrosphere. Due to the increase in the ISM density, the radiative cooling process takes place over a smaller time period as when compared to the previous figure. Due to this, the compression ratio decreases and the size of the astrosphere also decreases. For the standard ISM magnetic field scenario, red line, the TS is located at ~ 0.41 pc and the BS at ~ 1.6 pc. For 10 times the standard ISM magnetic field strength, black line, the TS is located at $\sim$ 0.43 pc and the BS at ~ 1.8 pc and for 1/10 times the standard ISM magnetic field strength, blue

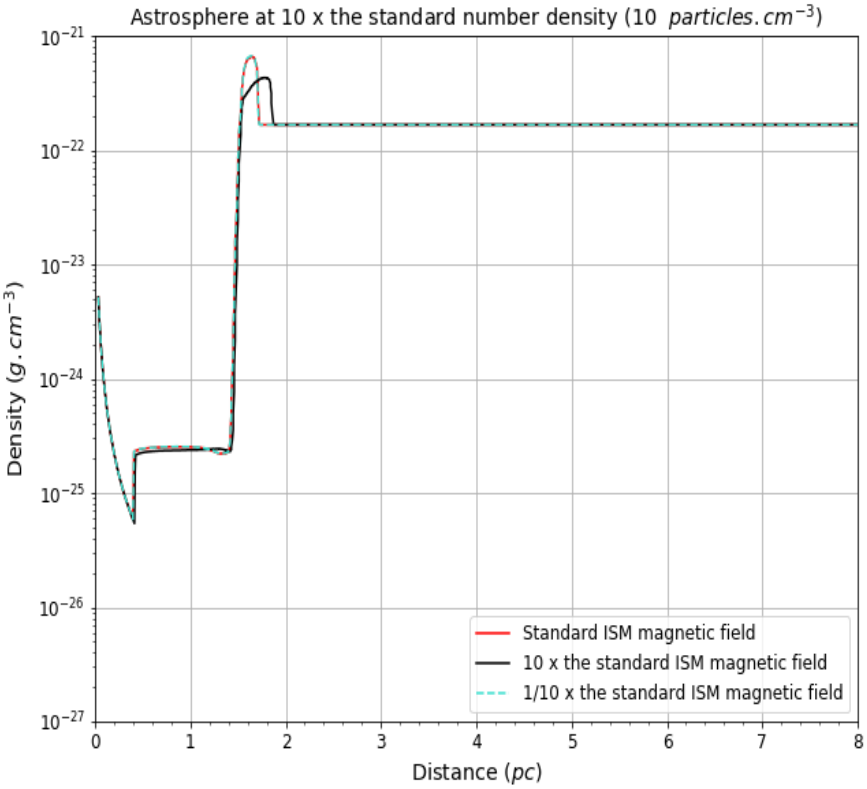

Figure 3.9: *Similar to the previous graph, the computed radial density profiles as a function of distance for an ISM density of* 1.6726×10^{-22} g cm^{-3} *or 10* particle cm^{-3} *are shown. The red line shows the standard magnetic field strength of* 3×10^{-6} *G, the blue line is 1/10 times the standard magnetic field strength (*3×10^{-7} *G) and the black line is double the standard magnetic field strength (*3×10^{-5} *G). Results are shown at 40 000 years simulation time.*

line, the TS is located at $\sim$ 0.4 pc and the BS at $\sim$ 1.6 pc.

Figure 3.10 shows the computed radial density profiles as a function of distance for the lowest ISM density scenario of 1.6726×10^{-24} g cm^{-3}. Again, three different scenarios corresponding to different ISM magnetic field strengths are shown. For the lower ISM density, the position of the TS and BS is shifted further out. Radiative cooling takes longer to compress the outer shell. As shown by the black line, for a lower ISM density scenario, the magnetic pressure becomes more important and as a result there is less compression in the outer shell. For the standard ISM magnetic field scenario, red line, the TS is located at $\sim$ 2.2 pc and the BS at $\sim$ 5.1 pc. For 10 times the standard ISM magnetic field strength, black line, the TS is located at $\sim$ 1.7 pc and the BS at $\sim$ 6.6 pc and for 1/10 times the standard ISM magnetic field strength, blue line, the TS is located at $\sim$ 2.1 pc and the BS at $\sim$ 4.9 pc.

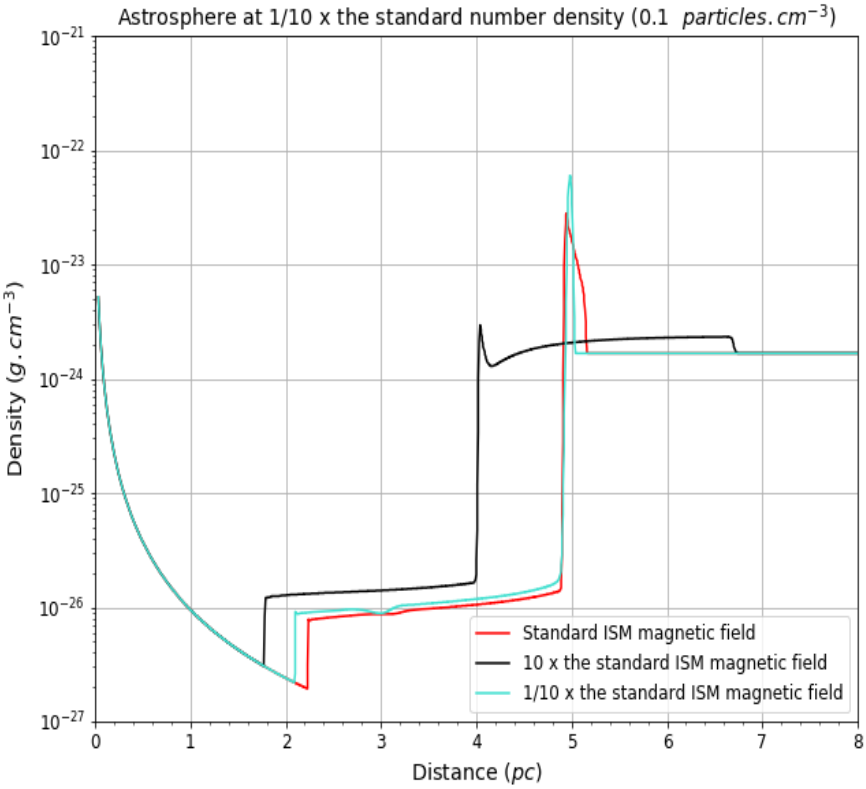

Figure 3.10: *This figure is similar to Figures 3.8 and 3.9, but for an ISM density of* 1.6726×10^{-24} g cm^{-3} *or 0.1* particle cm^{-3}. *The red line shows the standard magnetic field strength of* 3×10^{-6} *G, the blue line is 1/10 times the standard magnetic field strength (*3×10^{-7} *G) and the black line is double the standard magnetic field strength (*3×10^{-5} *G). Results are shown at 40 000 years simulation time.*

As shown in Figures 3.8 to 3.10, a larger ISM magnetic field increases the size of the OAS, which, in turn, causes the BS's compression ratio to decline. On the other hand, a smaller ISM magnetic field leads to a thinner outer shell. The stronger the magnetic field becomes, the less visible the effects of radiative cooling become.

In Figure 3.11, the compression ratio is shown as a function of time for three different magnetic field strengths. The red line corresponds to the standard ISM magnetic field of 3×10^{-6} G, the blue line corresponds to 1/10 times the standard ISM magnetic field (3×10^{-7} G) and the black line corresponds to 10 times the standard ISM magnetic field (3×10^{-5} G). The ISM density is 1.6726×10^{-23} g cm^{-3}. As shown, the larger the ISM magnetic field strength becomes, the lower the compression ratio becomes. For a magnetic field strength of 3×10^{-5} G (black line), the compression ratio reaches its peak of ∼4 at ∼15 000 years, then decreases to a ratio of ∼2 at ∼23 000 years, whereafter it grad-

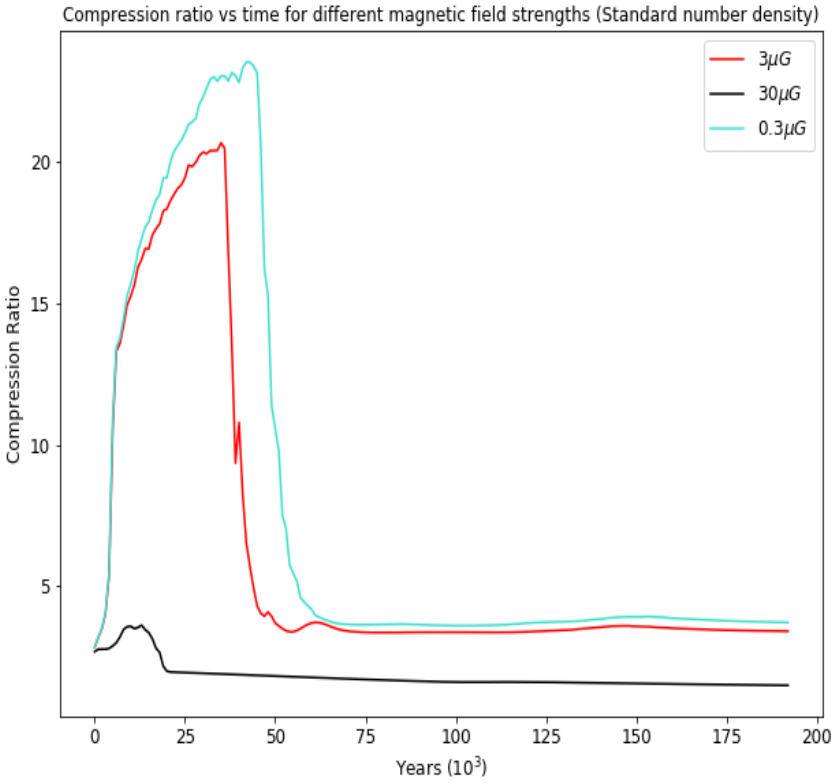

Figure 3.11: *The computed compression ratio for the BS as a function of time corresponding to an ISM density of* 1.6726×10^{-23} g cm^{-3}. *The red line shows the ratio corresponding to the standard magnetic field strength of* 3×10^{-6} G, *the blue line is 1/10 times the standard magnetic field strength (*3×10^{-7} G*) and the black line is 10 times the standard magnetic field strength (*3×10^{-5} G*).*

ually decreases. For the standard magnetic field strength (red line), the compression ratio reaches its peak of ∼20, then decreases to a ratio of ∼4 where it remains more or less constant. The blue line, with a magnetic field strength of 3×10^{-7} G, has a maximum compression ratio of ∼25 at ∼50 000 years, whereafter it gradually begins to decrease to a ratio of ∼5 and then remains more or less constant.

Figure 3.12 shows similar results, but here the ISM density is now 1.6726×10^{-22} g cm^{-3}. Shown here is that for a higher ISM density, the compression ratio decreases. This is because cooling occurs much sooner in the astrosphere's evolution compared to a lower ISM density scenario (see Figure 3.10). Similar to the previous figure is that the stronger the ISM magnetic field strength becomes, the more the compression ratio decreases. For a standard magnetic field strength and a magnetic field of 1/10 times the standard magnetic field strength (red and blue line), the compression ratio reaches its peak of ∼10 at ∼20 000 years, where both decrease and increase until they settle at a compression

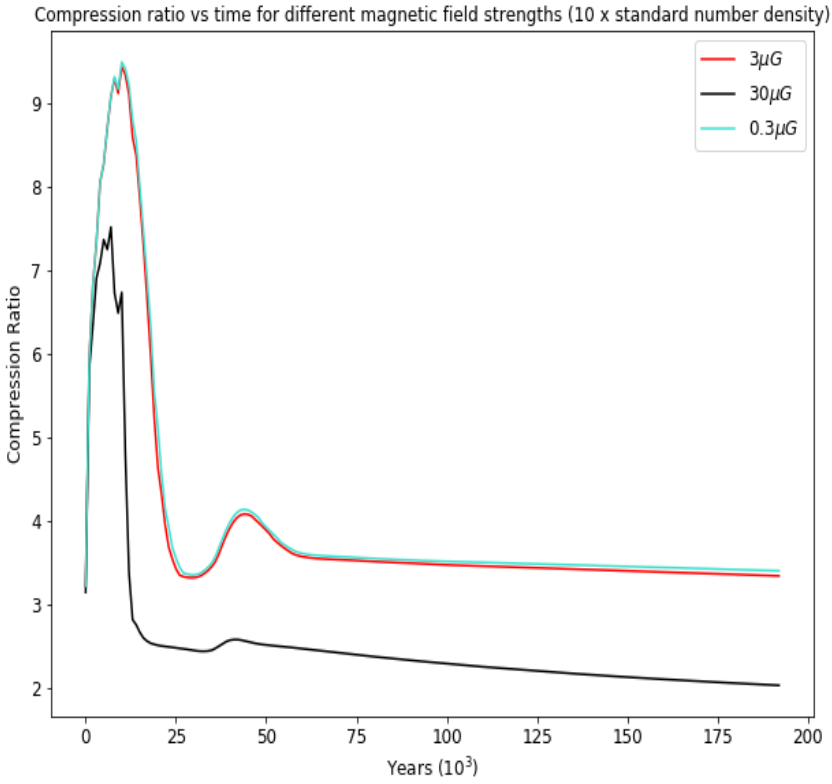

Figure 3.12: *This figure is the same as the previous one, but for an ISM density of* 1.6726×10^{-22} $\mathrm{g\,cm^{-3}}$ *as shown in Figure 3.9.*

ratio of almost 4. Whereas the magnetic field with a strength 10 times that of the standard magnetic field reaches a peak of ∼7.5, then decreases to a ratio of ∼2.

Lastly, for Figure 3.13, results are shown for an ISM density scenario of 1.6726×10^{-24} $\mathrm{g\,cm^{-3}}$. Shown here is that for a lower ISM density, as compared to the previous cases, the compression ratio increases at 40 000 years simulation time. The lower ISM magnetic field (blue line) has a compression ratio that gradually increases until it reaches its peak of ∼50 at 125 000 years (the lower the density, the longer it takes for the astrosphere to cool), then it decreases to a ratio of ∼3 where it remains. For the red and black line, standard and higher magnetic field strength, the compression ratio is extremely low at a value of ∼3 after ∼190 000 years.

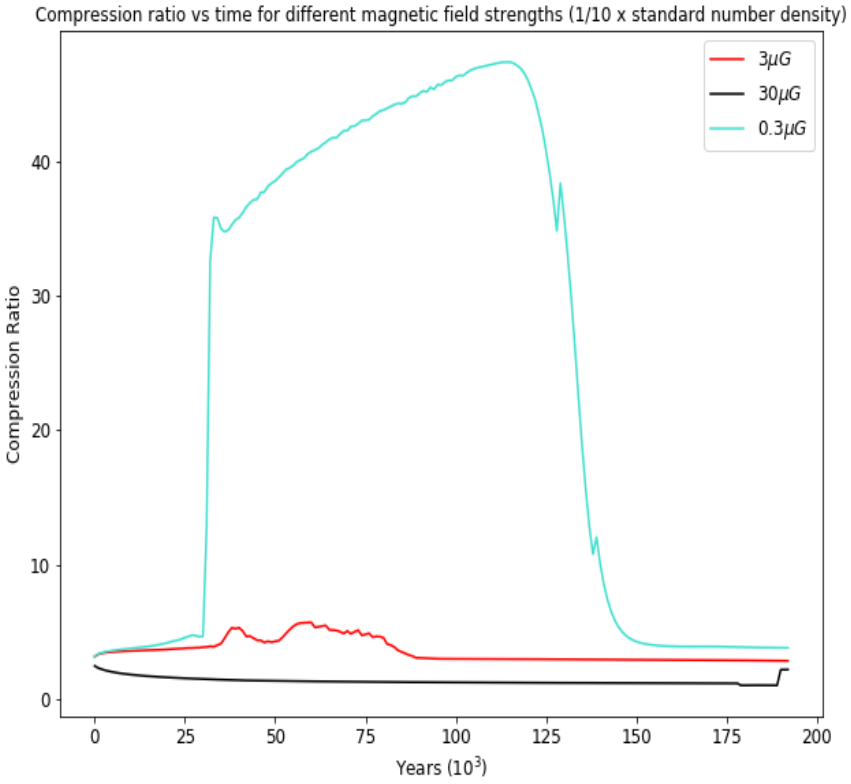

Figure 3.13: *Similar to Figures 3.11 and 3.12, but for an ISM density of* 1.6726×10^{-24} $\mathrm{g\,cm^{-3}}$ *as shown in Figure 3.9.*

3.5 Summary and Conclusions

In this section, the results of the previous sections can be summarized and compared to each other at various stages of evolution. This is done in Figure 3.14. This figure illustrates the computed radial density profiles as a function of distance for an ISM density of 1.6726×10^{-24} g cm^{-3}. The different scenarios including and excluding radiative cooling and different ISM magnetic field strengths of 3×10^{-5} G, 3×10^{-6} G and 3×10^{-7} G are shown at 40 000 years and 100 000 years, respectively. As shown before, the compression ratio changes as the ISM density increases or decreases. This ratio is further influenced by the addition of radiative cooling and an ISM magnetic field. The figure highlights how sensitive the astrosphere's geometry is to assumptions made in the model.

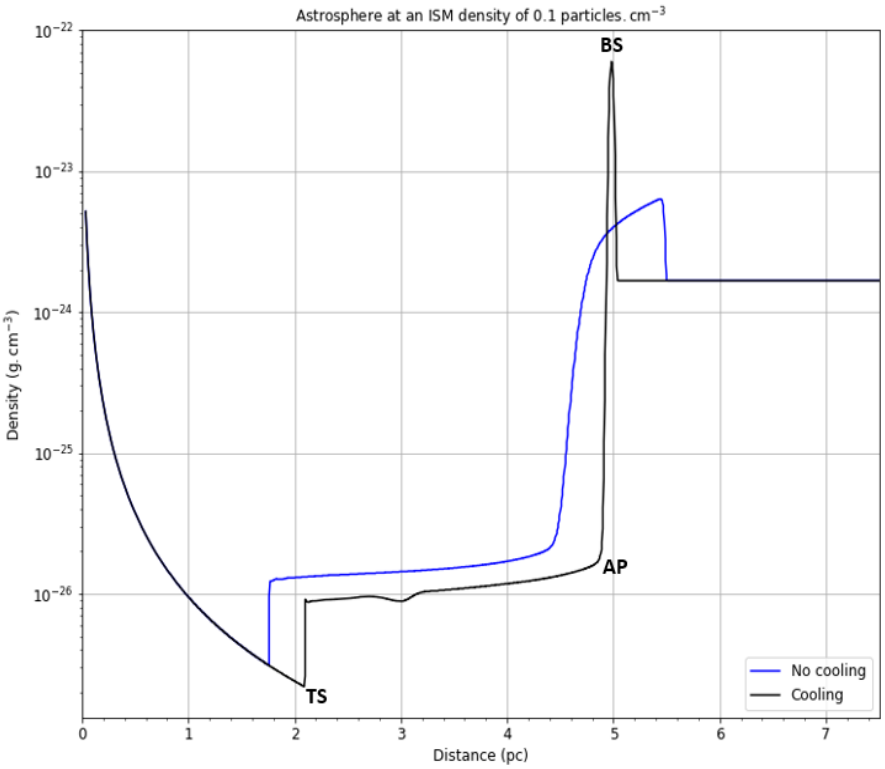

Figure 3.14: *This figure shows a computed astrosphere for a ISM density of* 1.6726×10^{-24} g cm^{-3} *or 0.1* particle cm^{-3} *for various scenarios including and excluding radiative cooling and different ISM magnetic field strengths at 40 000 years and a 100 000 years simulation time.*

When comparing, for example, the two pure hydrodynamic cases with and without cooling, for the case including cooling, there is a sharp peak in the density at the BS. Due to this increase in density, a thin shell is formed around the astrosphere. Because of cooling, the thermal pressure of the IAS and the OAS is lowered, reducing the OAS to a thin structure (thin outer shell). The distance

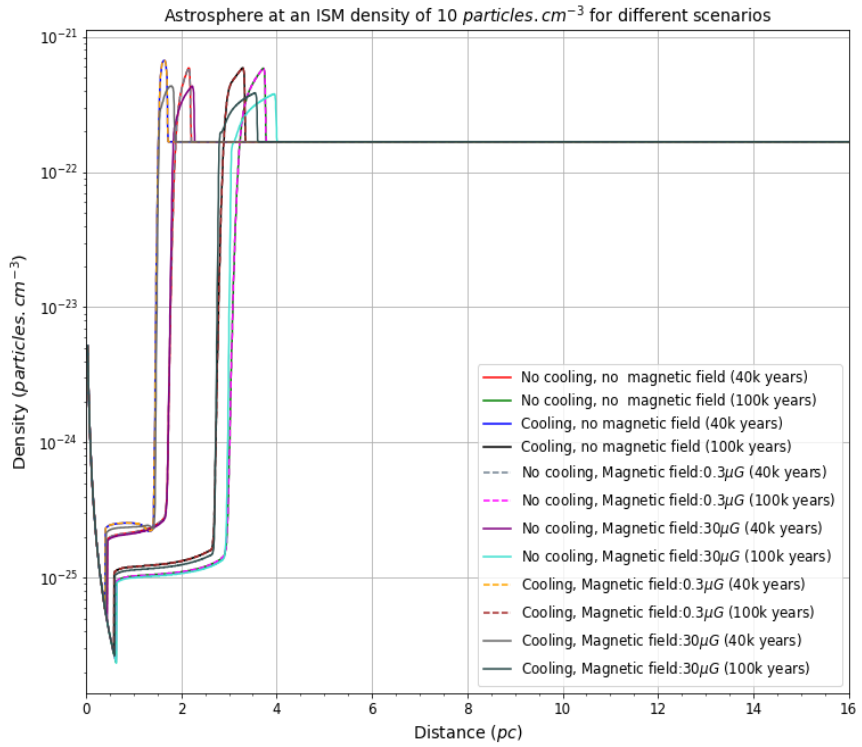

Figure 3.15: *The figure is similar to the previous one and shows an astrosphere for a higher ISM density of* 1.6726×10^{-22} g cm^{-3} *or 10* particle cm^{-3} *for the same set of scenarios for 40 000 years and 100 000 years.*

between the TS and the inner boundary is thus affected by cooling. As previously mentioned, cooling decreases the thermal pressure, which causes compression and, in turn, increases the density. Once the astrosphere is cooled, the OAS starts to decompress and the density decreases.

The addition of cooling results in a smaller astrosphere, whereas those without cooling are slightly larger. For the cases that include cooling and an ISM magnetic field, the effect of cooling becomes barely noticeable when the magnetic pressure begins to dominate over the ISM thermal pressure. A relatively strong ISM magnetic field leads to a decrease in the compression ratio of the BS as well as the density. At early stages, the astrosphere's OAS is compressed due to cooling. A magnetic field counteracts the effect of radiative cooling, causing the size of the OAS to increase. As a result, a double peak is visible in the outer shell, indicating that a distinct HOAS and COAS are created. Comparing the MHD cases with cooling at the two different times, it is clear that the OAS thickness has increased, and that the BS compression ratio decreases. Comparing the different ISM magnetic field strengths of the hydrodynamical case shows that the stronger the ISM magnetic field, the larger

the OAS becomes, which, in turn, decreases the BS's compression ratio. With the added ISM magnetic field pressure, the AP moves closer to the inner boundary and the AP has a thicker shell.

Figure 3.15 again shows a summary of results. It is similar to Figure 3.14, but now for an ISM density of 1.6726×10^{-22} g cm^{-3}. Comparing Figure 3.15 to Figure 3.14, it can be seen that for a lower ISM density scenario, the astrosphere only starts to cool around the time the astrosphere for a higher ISM density is already cooled. With the increase in ISM density, the size of the astrosphere decreases. For a stronger ISM magnetic field, the compression of the outer shell decreases. The position of the TS and the BS is also closer to the inner boundary. The distance between the AP and the inner boundary is shortened for a larger ISM magnetic field, because of the increase in the ISM magnetic pressure. For a higher ISM density, it is more difficult to find a distinction between a HOAS and a COAS and can only be done if the ISM magnetic field is large enough. As the ISM density increases, the magnetic field pressure becomes less important, whereas the thermal pressure becomes more significant.

Figure 3.16 (top panel) illustrates the evolution of an astrosphere with an ISM density of 1.6726×10^{-22} g cm^{-3}. The figure shows the computed density as a function of time. Density cuts are shown along the y-axis as a function of time on the x-axis. This is a pure hydrodynamic case excluding radiative cooling. From the inner boundary, the first shock (the black dark purple portion) is the TS. After that, we see the blue portion, which is the IAS. This is followed by the thin light blue-greenish line, the AP and then by the OAS, yellow-red portion and the white part, which is the BS.

The middle panel of Figure 3.16 is similar to the top panel, but now includes cooling. Radiative cooling decreases the thermal pressure, which causes compression and, in turn, increases the density. Compared to the top panel, compression is visible, especially at early times, with the compression ratio being dependent on the ISM density. As the density increases, so does the compression ratio. Without an ISM magnetic field, the astrosphere takes longer to decompress, and cooling must take place before it is able to decompress. The effect of cooling is especially visible at early times.

The bottom panel of Figure 3.16 shows the evolution of a computed astrosphere with an ISM density of 1.6726×10^{-24} g cm^{-3}. This is ten times less than the other two panels. Radiative cooling is included. Compared to the previous two contour plots, for this lower ISM density scenario, radiative cooling leads to a large increase in the compression of the outer shell. This figure ends this chapter's discussion, which highlighted the sensitivity of the evolution of astrospheres to different parameters.

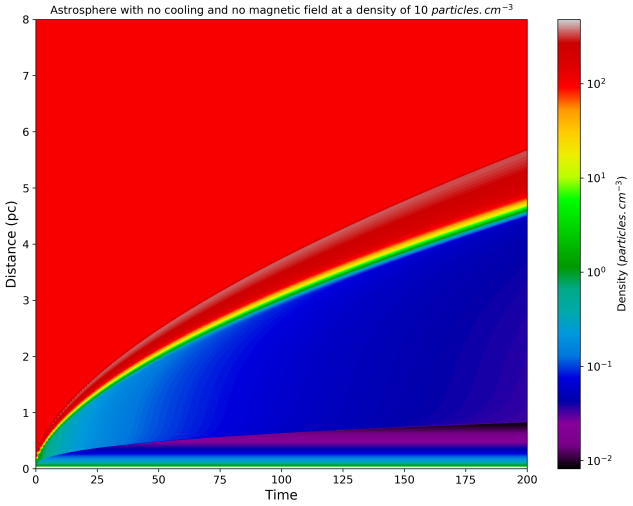

(a) *ISM density of* 1.6726×10^{-22} $\mathrm{g\,cm^{-3}}$ *or 10* $\mathrm{particle\,cm^{-3}}$ *with no radiative cooling.*

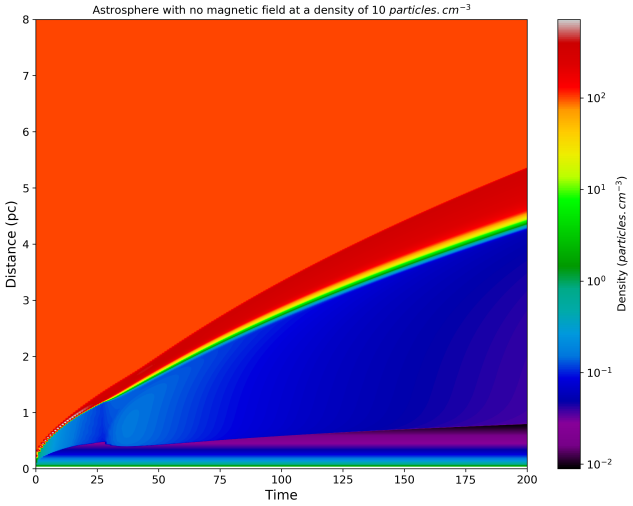

(b) *ISM density of* 1.6726×10^{-22} $\mathrm{g\,cm^{-3}}$ *or 10* $\mathrm{particle\,cm^{-3}}$ *with radiative cooling.*

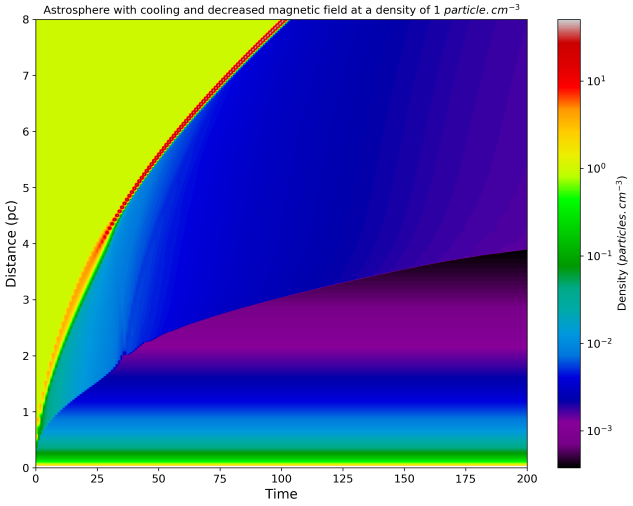

(c) *ISM density of* 1.6726×10^{-24} $\mathrm{g\,cm^{-3}}$ *or 1* $\mathrm{particle\,cm^{-3}}$.

Figure 3.16: *Three contour plots illustrate the evolution of a computed astrosphere. The first plot is a hydrodynamic case with no radiative cooling. The second plot is a hydrodynamic case with radiative cooling. For the third plot, cooling is included and there is an ISM magnetic field of* 3×10^{-7} G.

In the next chapter, a three-dimensional model will be used to show the effect of different grid cell sizes on astrospheric evolution.

Chapter 4

Three-dimensional simulations

4.1 Introduction

In the previous chapter, a two-dimensional HD and MHD model was used to simulate the evolution of an astrosphere for different scenarios that corresponded to different parameters in the model. These include changing the ISM density, the ISM magnetic field and stellar mass-loss rate. The aim was to see the effect it has on the TS and BS positions and compression ratios as well as the effect that the interstellar magnetic pressure has on the astrosphere's evolution. It was shown that radiative cooling, which results in a thin outer shell around the astrosphere, is dependent on the ISM density with the compression of the outer shell occurring sooner for a higher ISM density. Another parameter changed was the mass-loss rate. The mass-loss rate has an effect on the stellar wind ram pressure. As the mass-loss rate increases so does the ram pressure, leading to an overall bigger astrospheric structure. It was also shown that the ISM magnetic pressure causes the outer shell to decompress. Depending on the magnitude, it can cause the effect of cooling to be less visible in simulations.

In this chapter, astrosphere simulations computed with a three-dimensional MHD model are presented. In this model, Pen et al. (2003) proposed a three-dimensional MHD solver that makes use of a total variation diminishing (TVD) scheme, as discussed in Chapter 2. For the results in this chapter, the ISM parameters are as follows unless stated otherwise. The density is 1 particle cm^{-3} or 1.6726×10^{-23} $\mathrm{g\,cm}^{-3}$, the temperature is 10^4 K and the relative speed is 35 $\mathrm{km\,s}^{-1}$. The ISM magnetic field is 10 μG and is orientated 45° relative to the inflow direction to illustrate maximum and minimum effects. As discussed before, in the model of Pen et al. (2003), radiative cooling is not included. However, in Chapter 3, section 3.4, it is shown that in the presence of a relatively large ISM magnetic field strength, the effect of cooling on the evolution is significantly reduced. The aim of this chapter is to compare the different MHD model results to each other to establish the sensitivity of the model to the assumed grid cell sizes. This is done, not by varying the number of grid points,

but by changing the outer boundary distances to increase or decrease the grid cell size.

4.2 Asymmetrical results

Figure 4.1 shows four plots, of which three show density contour plots corresponding to different grid cell sizes and one plot (panel d) shows the density as a function of distance from the inner outflow boundary, which will be referred to as normalized. The density calculations are shown at 90 000 years. For all calculations, a grid of $n_x = n_y = n_z = 350$ is assumed, but the outer boundary distances were varied to change the grid cell size. The simulation volume for panel a, the top left panel is 10 pc (Δx = Δy = Δz = $\frac{10\text{pc}}{350}$), for panel b, the top right is 20 pc (Δx = Δy = Δz = $\frac{20\text{pc}}{350}$) and for panel c, the bottom left is 30 pc (Δx = Δy = Δz = $\frac{30\text{pc}}{350}$). Panel d, bottom right, shows the radial density profiles and is made from slices taken along the solid line, which is shown in the contour panels. For Figure 4.1, $B_x = -10$ μG, $B_y = 10$ μG and $B_z = 0$ is assumed. This will result in the magnetic pressure influencing the cavity evolution in certain areas. The drawn-in lines in panel b show the orientation of the interstellar magnetic field.

The shape of the cavity in Figure 4.1 is what is expected when one uses a single-fluid magneto-hydrodynamic approach. A more in-depth discussion on the detailed structure of an astrosphere can be found in Chapter 1 and a discussion on the heliosphere as an example of an astrosphere in Chapter 2. Since the star has a relative speed compared to the surrounding ISM, the astrosphere has the distinctive bullet like shape, where the IAS is smaller in the nose direction, but larger in the tail direction. After the TS, we see an increase in density leading to the AP. The astrosphere expands into the ISM and the BS forms. Between the TS and the AP, we find the IAS and between the AP and the BS is the OAS. The stellar wind decelerates from supersonic to subsonic velocities at the TS leaving the flow inside the IAS as subsonic. For Figure 4.1 (plus the other figures in this chapter), the TS and surrounding areas are shown by the black/dark purple colours. The AP is the dark blue colours and the slightly light/dark green colours are the BS area.

The effect that different grid cell sizes have on astrosphere simulations in Figure 4.1, is especially clear in the radial profile, shown in the bottom right panel. Shown here is that as the grid cell size decreases, the profile becomes less smooth. This means that at the TS and the BS, the transition from supersonic to subsonic speeds occurs in fewer grid points. Also, the TS shock seems to be a little further out for a smaller grid scenario as when compared to the other grid scenarios. The BS for the smallest grid scenario seems to be further from the origin compared to the other cases. The overall size of the IAS and OAS also varies as the grid cell size changes.

The TS and BS compression ratios can be calculated from the radial profiles shown in the bottom right panel. These are shown in Table 4.1. With increasing grid cell size, the BS compression ratio decreases by $\sim 5\%$ from scenario a to b and $\sim 10\%$ from b to c. The compression ratio from scenario a to c decreases by $\sim 14\%$ when the grid is made three times larger, with the TS compression ratio decreasing by $\sim 5\%$ from scenario a to b and $\sim 5\%$ from b to c. Comparing scenario a to scenario c shows that the compression ratio decreased by $\sim 10\%$ with a three times larger grid cell size. Thus, the compression ratios and smoothness of the results are somewhat dependent on grid cell size. Note that the ISM orientation in this figure is in the x-y plane. Other field configurations will be discussed later in order to illustrate how sensitive these results are to magnetic pressure.

TS and BS compression ratios of Figure 4.1			
Shock	Scenario a ($\Delta x = \Delta y = \Delta z = \frac{10\text{pc}}{350}$)	Scenario b ($\Delta x = \Delta y = \Delta z = \frac{20\text{pc}}{350}$)	Scenario c ($\Delta x = \Delta y = \Delta z = \frac{30\text{pc}}{350}$)
Termination shock	4.0	3.8	3.6
Bow shock	2.1	2.0	1.8

Table 4.1: *The TS and BS compression ratios of Figure 4.1.*

Figure 4.2 shows a contour plot of the ISM magnetic field corresponding to the density contour shown in Figure 4.1. Note that no stellar field is assumed in these simulations, but will be included in the next chapter. Again, different scenarios are shown corresponding to different simulation volumes as in the previous figure. Panel d shows the different radial profiles from the cuts taken along the x-y level in the nose direction, as indicated by the black line in Figure 4.1. Because only the ISM magnetic field is considered, almost zero values are present where a stellar field should be, hence the black appearance inside of the astrosphere.

Due to the orientation of the field, if the stellar wind flows perpendicular to the ISM field, we are able to see the largest possible compression of the field. When the flow is parallel, we see almost no compression. As seen from panel d, is that similar to the density scenario, changing the grid cell size does have an effect on the magnetic field. It results in a smoother radial profile for the larger grid cell size.

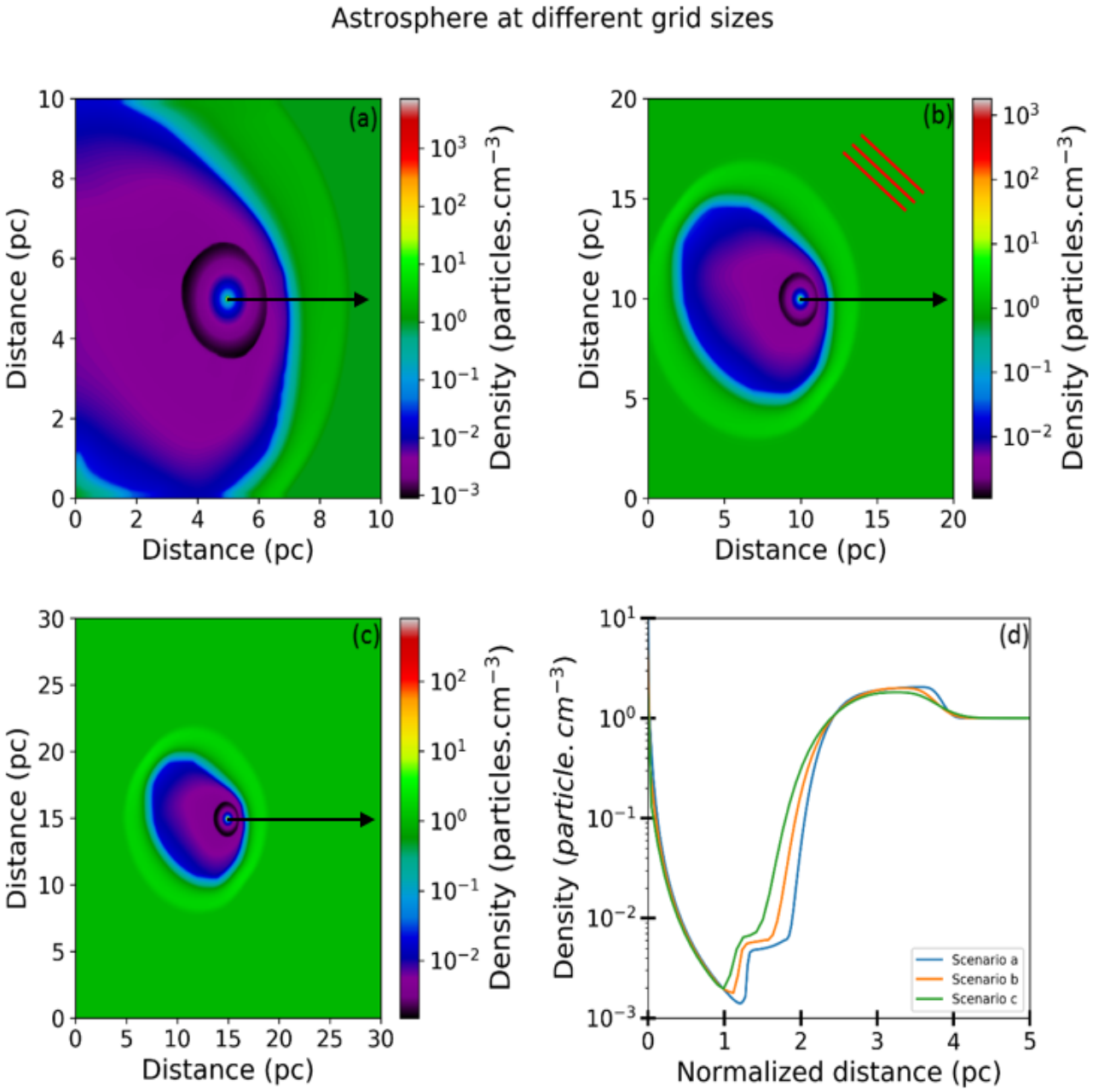

Figure 4.1: *Panels a, b and c show contour density plots that correspond to three different grid cell sizes by keeping the number of grid points the same, but changing the simulation volume. Results are shown at 90 000 years. It is assumed that* $n_x = n_y = n_z = 350$ *for all calculations with the simulation volume being varied from 10 pc in panel a to 20 pc in panel b and then to 30 pc in panel c. Plot d shows the density as a function of distance from the inner outflow boundary in the nose direction. The solid black line in panels a, b and c indicates the cut along which the data was taken to construct panel d. The blue line in the radial profile corresponds to panel a, the orange line to panel b and the green line to panel c. For this figure, an ISM magnetic field of* $B_x = -10$ μG, $B_y = 10$ μG *and* $B_z = 0$ *is assumed and the lines in panel b show the orientation of the field. A relative speed of 35* km.s^{-1} *is assumed.*

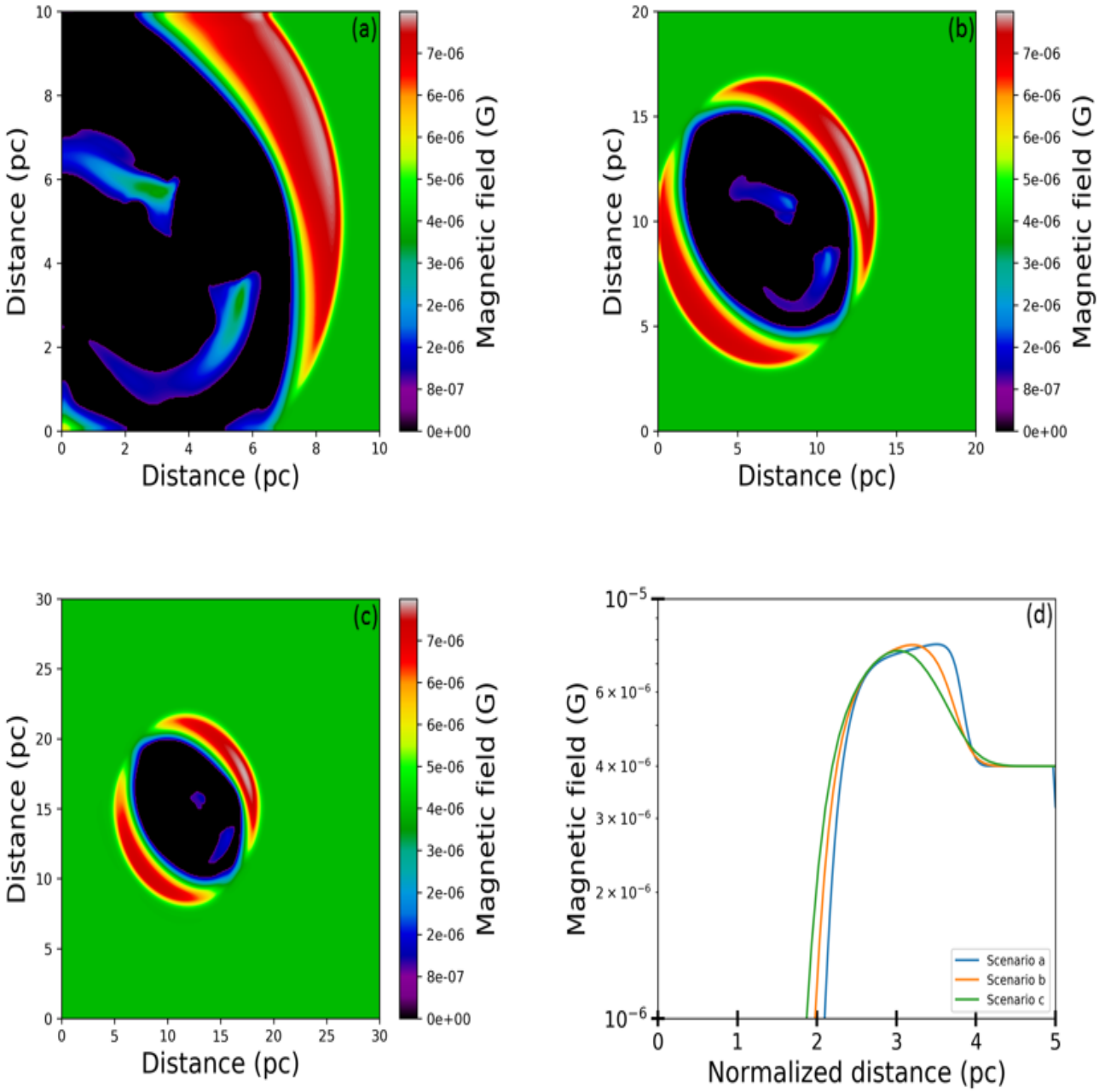

Figure 4.2: *Similar to Figure 4.1, but in terms of the interstellar magnetic field magnitude. Panel a shows the contour plot for a simulation volume of 10 pc, panel b for 20 pc and panel c for a volume of 30 pc. For the normalized radial profile, panel d, the magnetic field is plotted on a logarithmic scale and is made from cuts taken along the solid line, as shown in Figure 4.1. In panel d, the blue line corresponds to panel a, the orange line corresponds to panel b and the green line to panel c. A relative speed of 35* $\mathrm{km\,s^{-1}}$ *is assumed in the model.*

4.3 Bullet-shaped cavity

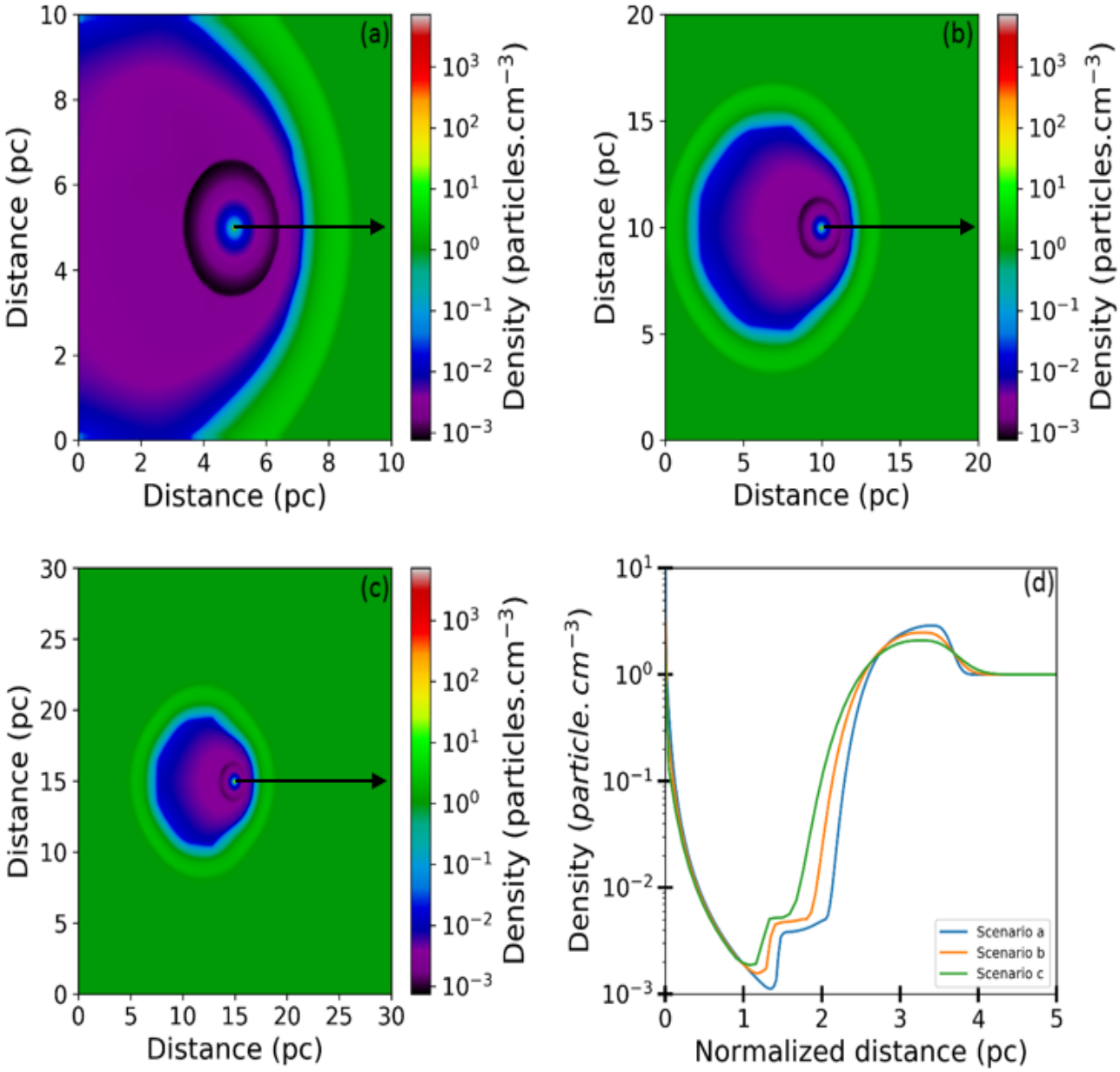

Figure 4.3: *Similar to Figure 4.1, but for this simulation no ISM magnetic field is assumed.*

Figure 4.3 is similar to Figure 4.1, showing the astrospheric evolution in terms of density at 90 000 years simulation time. As in Figure 4.1, simulations corresponding to different grid cell sizes are shown, with the difference being that in this figure no ISM magnetic field is included. Relative motion is again included with an ISM speed of 35 km s^{-1}.

Compared to Figure 4.1, this astrosphere has a clearer bullet- shaped structure. This is due to the exclusion of the strong ISM magnetic field assumed in Figure 4.1. The IAS size decreases for

TS and BS compression ratios of Figure 4.3			
Shock	Scenario a ($\Delta x = \Delta y = \Delta z = \frac{10\text{pc}}{350}$)	Scenario b ($\Delta x = \Delta y = \Delta z = \frac{20\text{pc}}{350}$)	Scenario c ($\Delta x = \Delta y = \Delta z = \frac{30\text{pc}}{350}$)
Termination shock	4.0	3.7	3.5
Bow shock	2.9	2.5	2.1

Table 4.2: *The TS and BS compression ratios of Figure 4.3.*

increasing grid cell size. For panel a to b, the TS compression ratio decreases by $\sim 7\%$ and from panel b to c it decreases by $\sim 5\%$. In panel a, the BS compression ratio is 2.9, for panel b the ratio is 2.5 and for panel c the compression ratio is 2.1, indicating that the increasing grid cell size, from panel a to panel c, causes a decrease in compression from panel a to b by $\sim 14\%$ and from panel b to c by $\sim 16\%$. With decreasing BS compression ratio, the density also decreases while the size of the OAS increases. The compression ratios can be found in Table 4.2.

Figure 4.4 is similar to Figure 4.3 but in the y-z plane. The results are shown at an earlier simulation time of 60 000 years. Again, panels a to c show the density of the computed astrosphere for the three different grid cell sizes and panel d gives the normalized radial profile, done in the same manner as the previous figures. The bullet-shaped structure is not seen in this plane. The TS compression ratio decreases by $\sim 13\%$ from scenario a to b and then by $\sim 4\%$ from scenario b to c. In this plane, the TS and BS compression ratios decrease for increasing grid cell size, as seen in panel d, with the TS ratio decreasing by $\sim 13\%$ from ~ 3.0 for scenario a to ~ 2.6 for scenario b to ~ 2.3 for scenario c, with $\sim 12\%$.

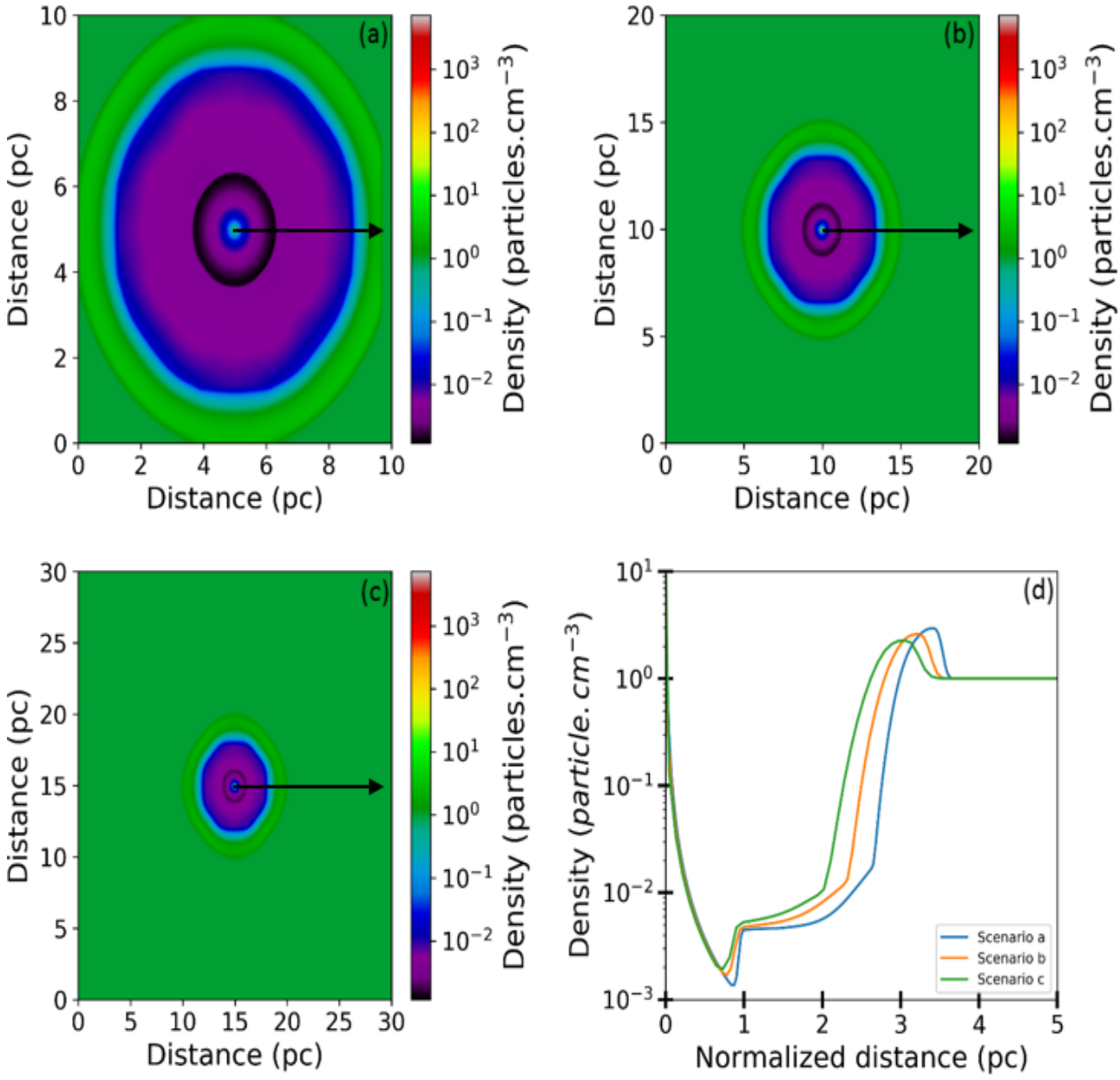

Figure 4.4: *Similar to the previous two figures but in the y-z direction and for a simulation time of 60 000 years.*

TS and BS compression ratios of Figure 4.4			
Shock	Scenario a ($\Delta x = \Delta y = \Delta z = \frac{10\text{pc}}{350}$)	Scenario b ($\Delta x = \Delta y = \Delta z = \frac{20\text{pc}}{350}$)	Scenario c ($\Delta x = \Delta y = \Delta z = \frac{30\text{pc}}{350}$)
Termination shock	3.1	2.7	2.6
Bow shock	3.0	2.6	2.3

Table 4.3: *The TS and BS compression ratios of Figure 4.4.*

4.4 Comparing results corresponding to different magnetic field orientations

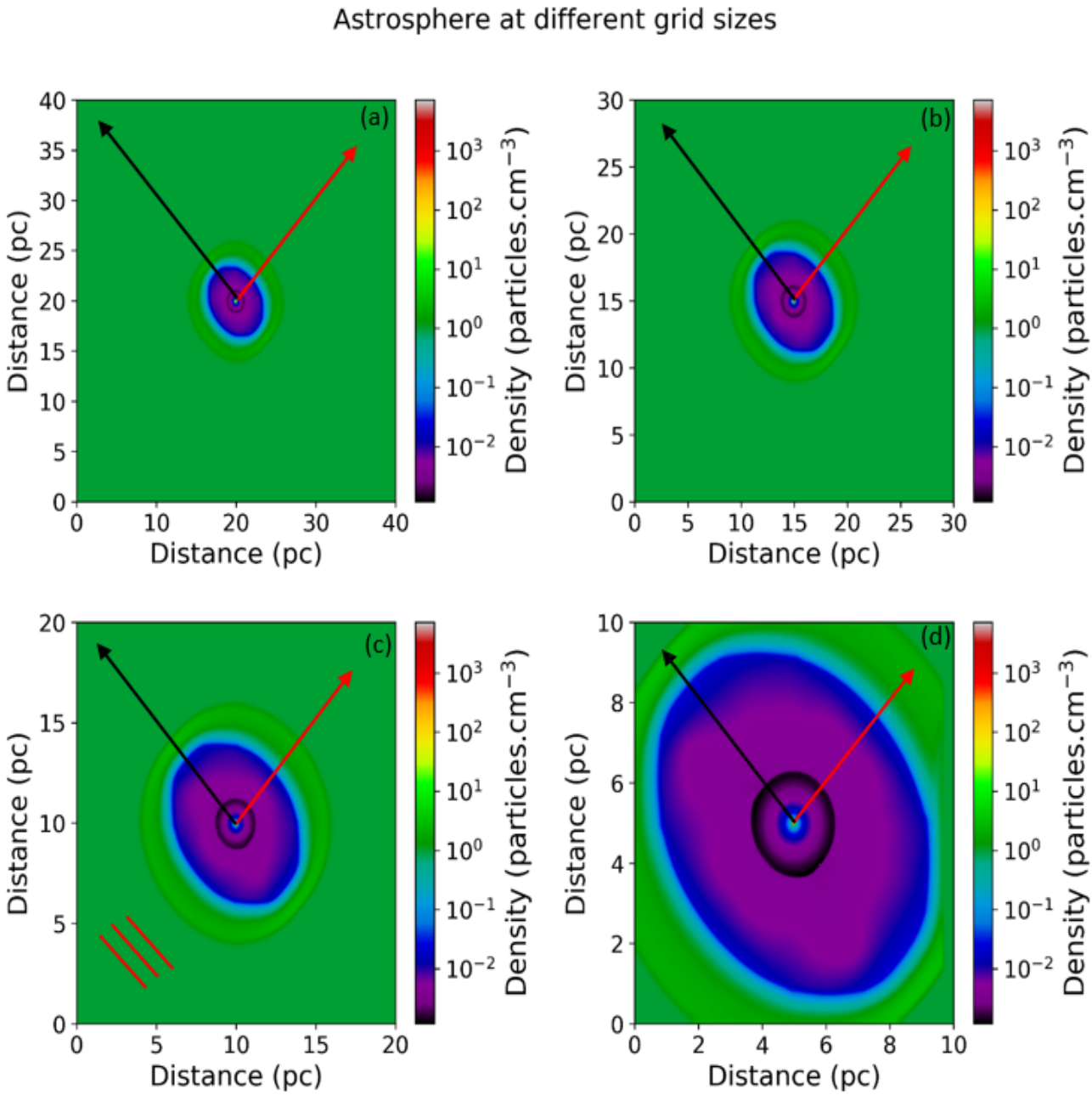

Figure 4.5: *Model simulations corresponding to four different grid cell sizes for 70 000 years simulation time. A grid of* $n_x = n_y = n_z = 350$ *is assumed and the simulation volumes from panels a to d are 40 pc, 30 pc, 20 pc and 10 pc, respectively. The black line and the red line in the panels are the cuts along which the radial profiles are shown in Figure 4.6. The drawn lines in panel c illustrate the orientation of the interstellar magnetic field.*

Figure 4.5 shows a computed astrosphere but this time for four different grid cell sizes corresponding to the assumption of different simulation volumes as indicated in the figure. The ISM magnetic

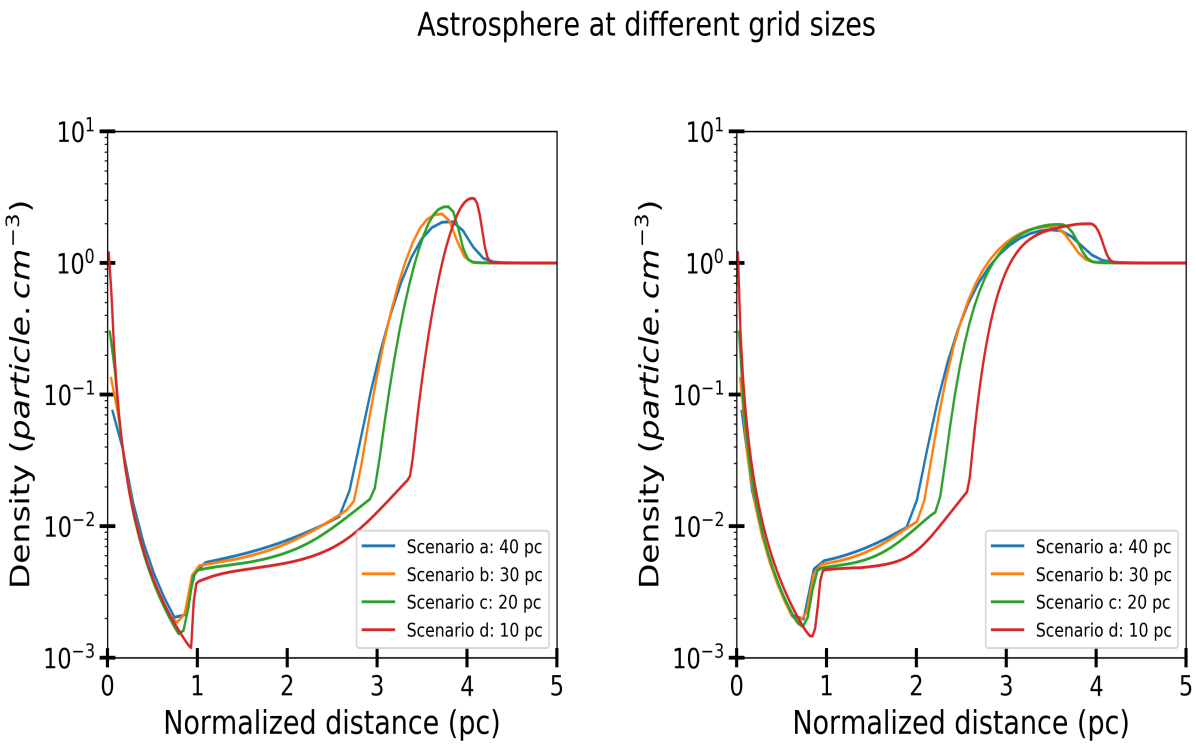

Figure 4.6: *This compares the radial profiles along the lines shown in Figure 4.5. The plot on the left hand side is the results corresponding to a slice along the black line, while the right hand side profile corresponds to the red line.*

field is assumed to be $B_x = -10$ μG, $B_y = 10$ μG and $B_z = 0$ and no relative speed is assumed. The density-contour graphs are shown for 70 000 years simulation time. Again, for the grid we have $n_x = n_y = n_z = 350$ but for panel a the assumed simulation volume is 40 pc, for panel b it is 30 pc, for panel c it is 20 pc and for panel d it is 10 pc. In panel d, the solid black line and the red line show the directions in which the radial profiles are plotted (see Figure 4.6). The drawn lines in panel c illustrate the orientation of the interstellar magnetic field. The ISM magnetic pressure is expected to have almost no effect along the solid black line, whereas along the red line, maximum effects of the ISM field on model results are expected.

The radial profiles corresponding to the different grid cell sizes are shown in Figure 4.6. The panel on the left shows results corresponding to a slice along the black line in Figure 4.5, while the right panel shows results corresponding to a slice along the red line. As in the other figures, as the grid decreases, the compression increases leading to a larger increase in the ISM density at the BS. Another factor to consider is the ISM magnetic field, which causes the size of the OAS and, in turn, the compression ratio of the BS to change. For the grid cell sizes 10-30 pc there is only a small difference in the compression ratio of the TS, as demonstrated in the figure and tabled in Tables 4.4

and 4.5. The compression ratio for the cavity of grid cell size 40 pc is lower than the other three.

TS and BS compression ratios of Figure 4.6, left side panel				
Shock	Scenario a ($\Delta x = \Delta y = \Delta z = \frac{40\text{pc}}{350}$)	Scenario b ($\Delta x = \Delta y = \Delta z = \frac{30\text{pc}}{350}$)	Scenario c ($\Delta x = \Delta y = \Delta z = \frac{20\text{pc}}{350}$)	Scenario d ($\Delta x = \Delta y = \Delta z = \frac{10\text{pc}}{350}$)
Termination shock	2.6	2.8	3.0	3.3
Bow shock	1.9	2.3	2.6	3.0

Table 4.4: *The TS and BS compression ratios of Figure 4.6, left side panel.*

TS and BS compression ratios of Figure 4.6, right side panel				
Shock	Scenario a ($\Delta x = \Delta y = \Delta z = \frac{40\text{pc}}{350}$)	Scenario b ($\Delta x = \Delta y = \Delta z = \frac{30\text{pc}}{350}$)	Scenario c ($\Delta x = \Delta y = \Delta z = \frac{20\text{pc}}{350}$)	Scenario d ($\Delta x = \Delta y = \Delta z = \frac{10\text{pc}}{350}$)
Termination shock	2.7	2.7	2.7	3.4
Bow shock	1.7	1.8	1.9	1.9

Table 4.5: *The TS and BS compression ratios of Figure 4.6, right side panel.*

The direction in which the radial density profiles are plotted in Figure 4.6, right side panel, is shown by the solid red line in Figure 4.5. Along this direction, the BS region is much more spread out due to the magnetic pressure. The BS compression ratio increases as the density increases. There is a $\pm 15\%$ increase in the compression ratio from scenario a to d. The left side panel is the radial profile taken along the black line. In this direction, the magnetic pressure does not significantly influence the BS compression.

Comparing the radial profiles in the left side panel to those in the right side panel shows a clear difference in the density and BS compression ratio along the different directions. The effect that the interstellar magnetic field orientation has on the astrospheric structure, the density and the compression ratio is clearly visible. The magnetic pressure has almost no effect along the black line, and therefore the compression of the OAS in the left side panel remains nearly unaffected.

The magnetic pressure does, however, have a maximum effect in the direction of the red line, which is visible in the right side panel. Comparing the left and right panels in Figure 4.6 to each other shows that the ISM magnetic pressure somewhat influences the effect that the grid cell size has on simulations, e.g., for the left panel the BS compression changes by $\sim 36.7\%$ from a to d, while for the right panel the change is $\sim 11.8\%$. This is of course expected because the magnetic pressure results in lower compression ratios and also a naturally more smooth profile as compared to the case where the magnetic pressure contribution is small.

4.5 Summary and Conclusions

In this chapter, the effect of the grid cell size on the evolution of an astrosphere was shown. The simulations were done with a three-dimensional MHD model and the sensitivity of the model to the assumed grid cell sizes was shown. This was done by keeping the number of grid points the same, and then changing the outer boundary distances to either increase or decrease the grid cell size. The ISM magnetic field was assumed as $B_x = -10$ μG, $B_y = 10$ μG and $B_z = 0$. The effect that the ISM magnetic field orientation had on the astrospheric evolution was shown in Figures 4.1 and 4.6. The other ISM parameters that remained constant throughout were the ISM density of 1 particle cm^{-3} or 1.6726×10^{-23} g cm^{-3}, the ISM temperature of 10^4 K and the relative speed of 35 km s^{-1}. Some of the simulations included an ISM magnetic field and a relative speed, with others including either one or the other or neither of the two. A grid of $n_x = n_y = n_z = 350$ was assumed. The effect that relative speed has on the astrosphere is discussed in detail in the next chapter. The radial profiles shown were made from cuts taken along the solid black and red lines as indicated in the different panels. It was shown that increasing the computational domain for the same number of grid cells, reduced the resolution and thus the sharpness of features could not be captured.

Figure 4.1 showed model results that were done assuming three different outer boundaries, namely 10 pc, 20 pc and 30 pc, while keeping the number of grid points the same. Furthermore, $B_x = -10$ μG, $B_y = 10$ μG and $B_z = 0$ and a relative speed of 35 km s^{-1} were assumed. Panel d showed the normalized radial profile. From the radial profile and Table 4.1, it was clear that the TS and BS compression ratios decreased for increasing grid cell size. Figure 4.2 showed the density rendered profile of the interstellar magnetic field corresponding to Figure 4.1. No stellar field was assumed, and the parameter was set to zero for all simulations. Shown here was that the grid cell size affected the magnetic field, and similar to the density was that for a larger grid cell size the results are much more smooth as when compared to a smaller grid cell size.

Figures 4.3 and 4.4 showed the model results for a more bullet-shaped astrosphere. The parameters were the same as in Figure 4.1, but no ISM magnetic field was assumed. Relative motion with a relative speed of 35 km s^{-1} was assumed. Figure 4.4 was also similar to 4.1, but the results were shown at an earlier simulation time. The results of Figures 4.3 and 4.4 were consistent with that of Figure 4.1, concluding that the TS and BS compression ratios decreased for an increasing grid cell size.

Figures 4.5 and 4.6 showed results also corresponding to different grid cell sizes. However, empha-

sis here was on comparing profiles along different directions where the ISM magnetic field orientations differ. Along the black line, the ISM magnetic pressure was determined to have almost no effect, but had maximum effects along the red line. The profiles in the left side panel showed results corresponding to cuts taken along the black line and the profiles in the right side panel showed results corresponding to cuts taken along the red line in Figure 4.5. For the left side panel, the compression of the OAS remains almost unaffected, while for the right side panel, due to the increase in magnetic pressure, the OAS decompressed faster increasing its size. In conclusion, the ISM magnetic field pressure also influenced the effect that different grid cell sizes had on model simulations. In a region of large magnetic pressure, the effect of the grid cell size was less because the magnetic pressure naturally leads to a smoother profile.

Chapter 5

Three-dimensional simulations of M-stars

5.1 Introduction

In the previous chapter, simulations were done with a three-dimensional cartesian MHD model. The effects of varying the simulation volume (grid cell size) and the effect of the ISM magnetic field on the evolution of an astrosphere were shown. Some of those simulations included a relative speed and others a strong ISM magnetic field to show the effects that these parameters have on simulations. It was concluded that the grid cell size does affect the evolution of the astrosphere and by varying the grid cell size the TS and BS positions, density and compression ratios were influenced. The orientation of the interstellar magnetic field, together with relative speed, also influenced the astrosphere's overall size, density and compression ratios.

The aim of this chapter is to compare different three-dimensional MHD model results of two different stars to the results of Herbst et al. (2020). These authors used the three-dimensional MHD code CRONOS (Kissmann et al. 2018). This model has been successfully used for simulations of hot O-and B-type stars (Scherer et al. 2015), and can also be used to study the shock structures of astrospheres (Scherer et al. 2016). The two M-dwarf stars that are selected in this study are LHS 1140 and Proxima Centauri. For these two, the relative ISM speeds as well as the outflow speeds will be varied to illustrate the sensitivity of the astrospheres to these parameters. Again, the three-dimensional cartesian model, as described in Chapter 2.2, will be used, and results will be compared to Herbst et al. (2020). For the previous chapter, no stellar magnetic field was assumed, but for this chapter, a stellar field is included. For an in-depth discussion on the different parameters, refer to Herbst et al. (2020) or Herbst et al. (2022).

Simulations were done under the assumption that there is a likeness between the stellar field and the heliospheric magnetic field. This leads to the following astrospheric magnetic field,

$$B = B_0 \frac{r_0^2}{r^2} \sqrt{1 + \left(\frac{r\Omega}{\nu_{SW}} \right)^2 sin^2\vartheta}, \tag{5.1}$$

similar to the Parker spiral (Parker 1958). The parameters are the magnetic field magnitude at the inner boundary (B_0), the stellar rotation rate (Ω), the distance from the star (r_0), the stellar distance from the origin (r), with the colatitude angle (ϑ) and the stellar wind speed (ν_{SW}). This equation results in a field with a radial and azimuthal component, although the azimuthal component dominates most of the astrosphere.

M-dwarfs are extremely common, accounting for at least 75% of all stars in our galaxy (Dittmann & et al. 2017). The two stars chosen in this chapter are LHS 1140 and Proxima Centauri. LHS 1140 or GJ 3053 is an inactive star with Proxima Centauri or GJ 551 an active flaring star, meaning that its luminosity is subject to change. Between the two stars, Proxima Centauri is 4.22 light years from the Sun and thus is the closest, with LHS 1140 48.9 light years from the Sun. Proxima Centauri is a small, main-sequence star with an overall low luminosity. M-dwarfs have also recently become a main topic of investigation in the search of habitable exoplanets. Both LHS 1140 and Proxima Centauri have an earth-like planet, namely LHS 1140 b and Proxima Centauri b. Proxima Centauri b has a mass of ∼1.3 times that of the earth and the orbital period is 11.2 days (Garraffo et al. 2016), while LHS 1140 b has a mass of ∼6.38 times that of the earth and the orbital period is 24.7 days (Dittmann & et al. 2017).

5.2 Astrospheric simulations of LHS 1140

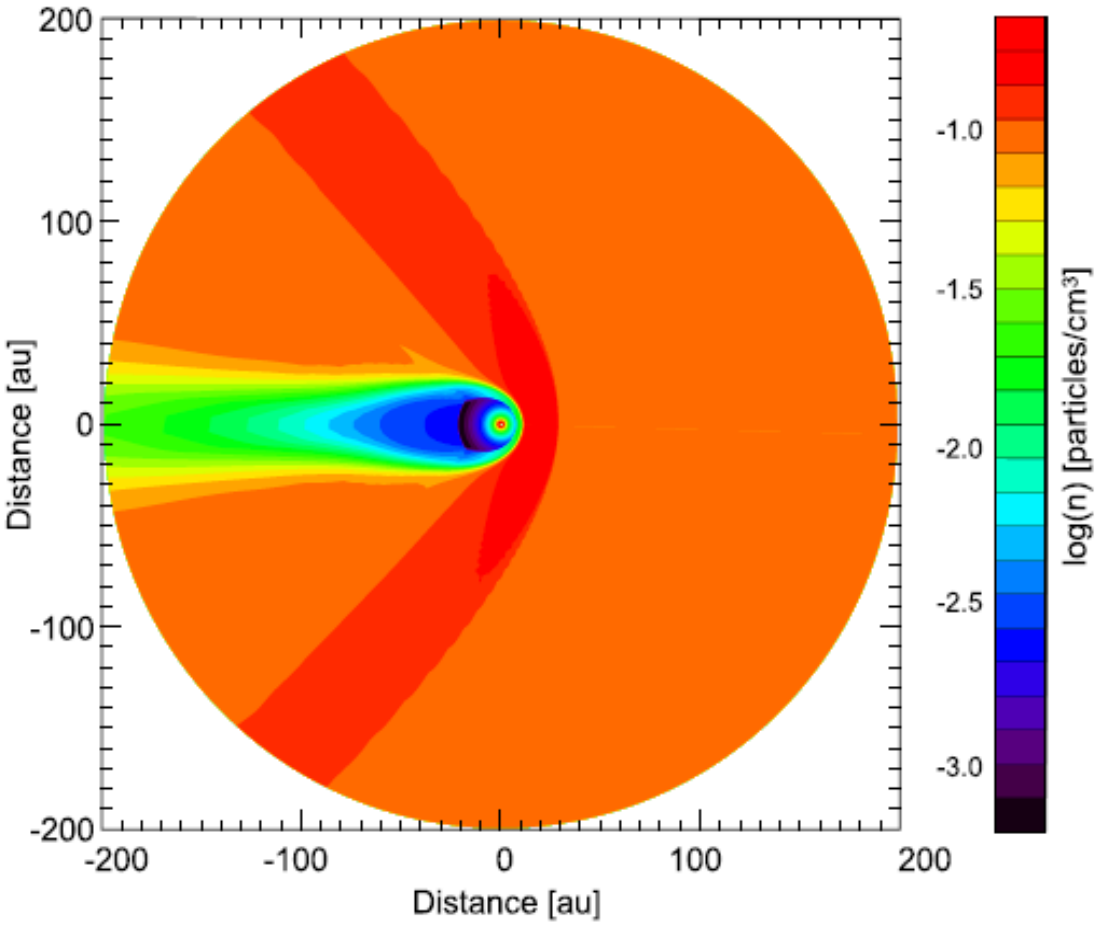

Figure 5.1: *The density of the astrosphere of LHS 1140 taken from Herbst et al. (2020). The density is plotted on a spherical grid of resolution* $N_r \times N_\vartheta \times N_\varphi = 1024 \times 64 \times 120$ *cells. All assumed parameters can be viewed in Table 1 of Herbst et al. (2020).*

Figure 5.1 shows the computed density of the astrosphere of LHS 1140, taken from Herbst et al. (2020). For the simulations, a spherical grid was used. The resolution of the grid for LHS 1140 was $N_r \times N_\vartheta \times N_\varphi = 1024 \times 64 \times 120$ cells. The TS is at a distance of ∼8.1 AU, the BS is at a distance of ∼28.9 AU and the AP is at a distance of ∼11.5 AU, which shows that the size of the astrosphere is small compared to, e.g. our heliosphere.

For this study, astrospheric simulations of LHS 1140 with similar, but not quite the same, parameters to those found in Table 1 of Herbst et al. (2020) were assumed. The reason is that some of those listed in Herbst et al. (2020) were more constrained with additional literature studies (Scherer, private communication 2022). In this work, an ISM density of 0.3 particles cm^{-3} is assumed. Other assumptions made are the ISM magnetic field of 3.7×10^{-6} G, the ISM temperature of 9000 K and

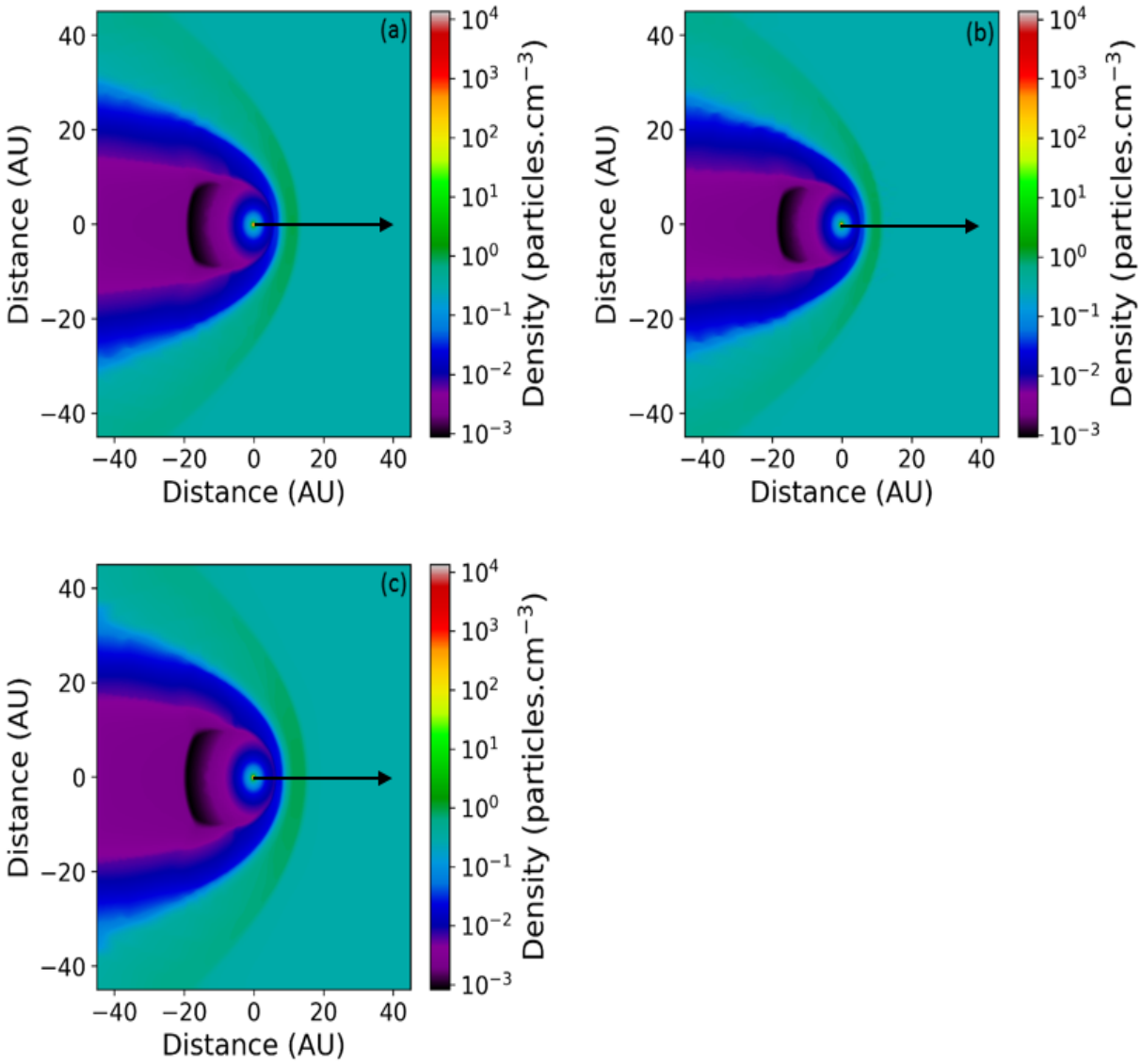

Figure 5.2: *The density of the astrosphere of LHS 1140 with the density plotted as a function of distance for 120 000 years simulation time. A grid cell size of* $\Delta x = \Delta y = \Delta z = \frac{90\text{pc}}{350}$ *is assumed. The plot shows the astrospheric evolution for three different ISM wind speeds. Panel a is the standard scenario and has an ISM wind speed of 40* $\text{km}\,\text{s}^{-1}$*. Panel b is simulated with a faster ISM wind speed of 45* $\text{km}\,\text{s}^{-1}$ *and panel c is simulated for a slower ISM speed of 35* $\text{km}\,\text{s}^{-1}$*.*

the stellar mass-loss rate of $\sim 2 \times 10^{-15}$ $\text{M}_{\odot}\,\text{year}^{-1}$. The simulations were performed on a cartesian grid of $\Delta x = \Delta y = \Delta z = \frac{90\text{AU}}{350}$ with a simulation volume of 90 AU.

Figure 5.2 shows the density of the astrosphere for LHS 1140 for 120 000 years simulation time. The astrosphere is simulated for three different ISM wind speeds. Panel a, top left, shows the standard ISM wind speed scenario of 40 $\text{km}\,\text{s}^{-1}$, similar to what is assumed in Herbst et al. (2020), for the simulation in panel b, top right, the ISM wind speed is 45 $\text{km}\,\text{s}^{-1}$ and for the simulation in panel c, bottom left, the ISM wind speed is 35 $\text{km}\,\text{s}^{-1}$. The black line in panels a, b and c indicates

the direction in which the radial profiles, Figure 5.3, are plotted. From the different scenarios it is evident that the astrosphere size is somewhat influenced by the ISM wind speed. As the ISM wind speed increases, the size of the OAS decreases. In panel a of Figure 5.2, the TS is at a distance of ∼6.1 AU, the BS at a distance of ∼12 AU and the AP at a distance of ∼9.4 AU. Compared to Figure 5.1, it is clear that the astrosphere for Figure 5.1 is larger than the one in Figure 5.2. However, note that for the simulations in this work, the ISM magnetic field and ISM density values for Figure 5.2 are slightly different to the ones used for Figure 5.1. This, along with the difference in grid cell size (as discussed in the previous chapter), can account for the size difference. Also, whether or not both simulations are shown for the same simulation time is also unknown. The sizes of the IAS and the OAS are different, with the IAS and the OAS of Figure 5.1 being larger and leading to an overall larger astrosphere. However, when compared to our heliosphere, both of these simulations predict a relatively smaller astrosphere.

Figure 5.3 shows the computed radial profile along the arrows in Figure 5.2. Scenario a, blue line, is taken from panel a and has an ISM wind speed of 40 $\mathrm{km\,s^{-1}}$, scenario b, orange line, is taken from panel b and has an ISM wind speed of 45 $\mathrm{km\,s^{-1}}$ and then scenario c, green line, is taken from panel c and has an ISM wind speed of 35 $\mathrm{km\,s^{-1}}$. As the ISM wind speed decreases, the AP moves further out away from the inner boundary and the size of the IAS and the OAS increases. For a smaller speed, the overall size of the astrosphere increases. All three results are relatively smooth indicating the need for simulations to be done on a much finer grid in the near future, as was illustrated in the previous chapter.

From Figure 5.3, for scenario a, the TS is at a distance of ∼6.1 AU, the AP at ∼9.4 AU and the BS at ∼12 AU. For scenario b, the TS is at ∼5.5 AU, the AP at ∼8.7 AU and the BS at ∼10.6 AU and for scenario c, the TS is at a distance of ∼6.8 AU, the AP at ∼11 AU and the BS at ∼14.2 AU. From the above results it is clear that the astrosphere for LHS 1140 is relatively small, which proves that not all cool M-stars have large astrospheres (see also Herbst et al. (2020)). From the standard ISM wind speed (scenario a), to the faster ISM wind speed (scenario b), the TS and the BS move inwards by ∼9.8% and ∼11.7% respectively. Comparing scenario a to c (smaller ISM wind speed), the TS and BS move outward by ∼11.5% and ∼18.3% respectively. Shown here is that the relative speed is an important parameter. The TS and BS compression ratios are also slightly affected.

Figure 5.4 shows the plot of the corresponding stellar and ISM magnetic field of the standard scenario, as shown in panel a of Figure 5.2. The xy, xz and yz profiles are shown in panels a to c,

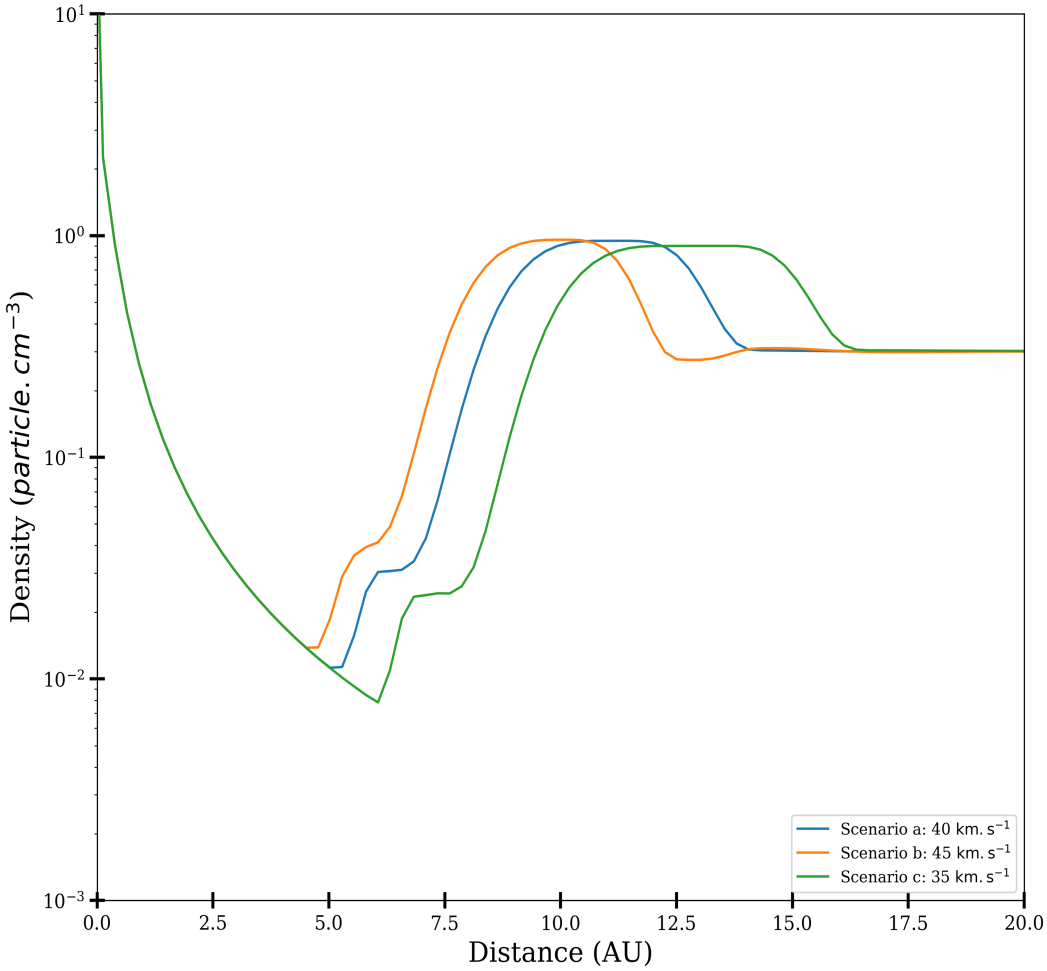

Figure 5.3: *The computed radial profile corresponding to Figure 5.2 shows the density as a function of the distance for three different ISM wind speeds. The blue line, scenario a, is taken along the black line in panel a, the orange line, scenario b, is taken along the black line in panel b and the green line, scenario c, is taken from panel c along the black line. Scenario a is for an ISM wind speed of 40* $\mathrm{km\,s^{-1}}$*, scenario b is for a ISM wind speed of 45* $\mathrm{km\,s^{-1}}$ *and scenario c is for an ISM wind speed of 35* $\mathrm{km\,s^{-1}}$.

respectively. As discussed in the previous chapters, the addition of an ISM magnetic field increases the ISM magnetic pressure, allowing the OAS to decompress faster lowering the density and, in turn, the compression ratio. In terms of the magnetic field, the BS is particularly noticeable. As the ISM magnetic pressure increases, it suppresses the BS. The plot shows that the ISM magnetic field piles up in specific regions, resulting in more ISM magnetic pressure being exerted in these areas.

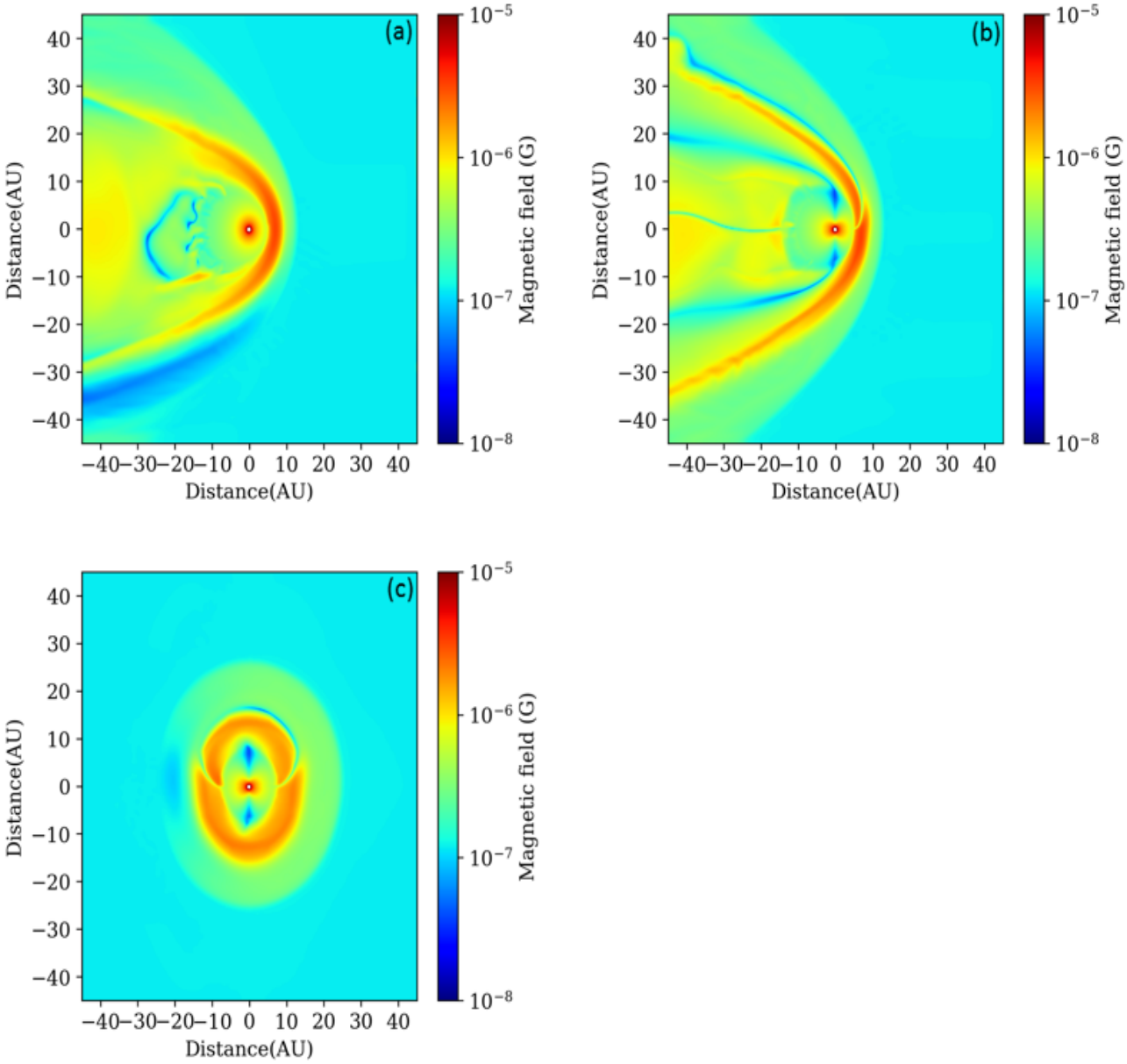

Figure 5.4: *Similar to Figure 5.2, but in terms of the stellar and ISM magnetic field. The contour plot corresponds to the astrosphere simulated in panel a and the assumed ISM wind speed is 40* $\mathrm{km\,s^{-1}}$. *For this figure, panel a shows the astrosphere in the xy plane, panel b shows the astrosphere in the xz plane and panel c shows the astrosphere in the yz plane.*

5.3 Astrospheric simulations of Proxima Centauri

Figure 5.5 shows the computed density plot of the astrosphere of Proxima Centauri, taken from Herbst et al. (2020). Again, the assumed parameters can be viewed in Table 1 of Herbst et al. (2020). The simulation was done with a spherical grid of resolution $N_r \times N_\vartheta \times N_\varphi = 1024 \times 64 \times 32$ cells. The TS is located at a distance of ∼76 AU, with the AP located at a distance of ∼110 AU. From the plot it is visible that for this simulation of Proxima Centauri there is no clear BS.

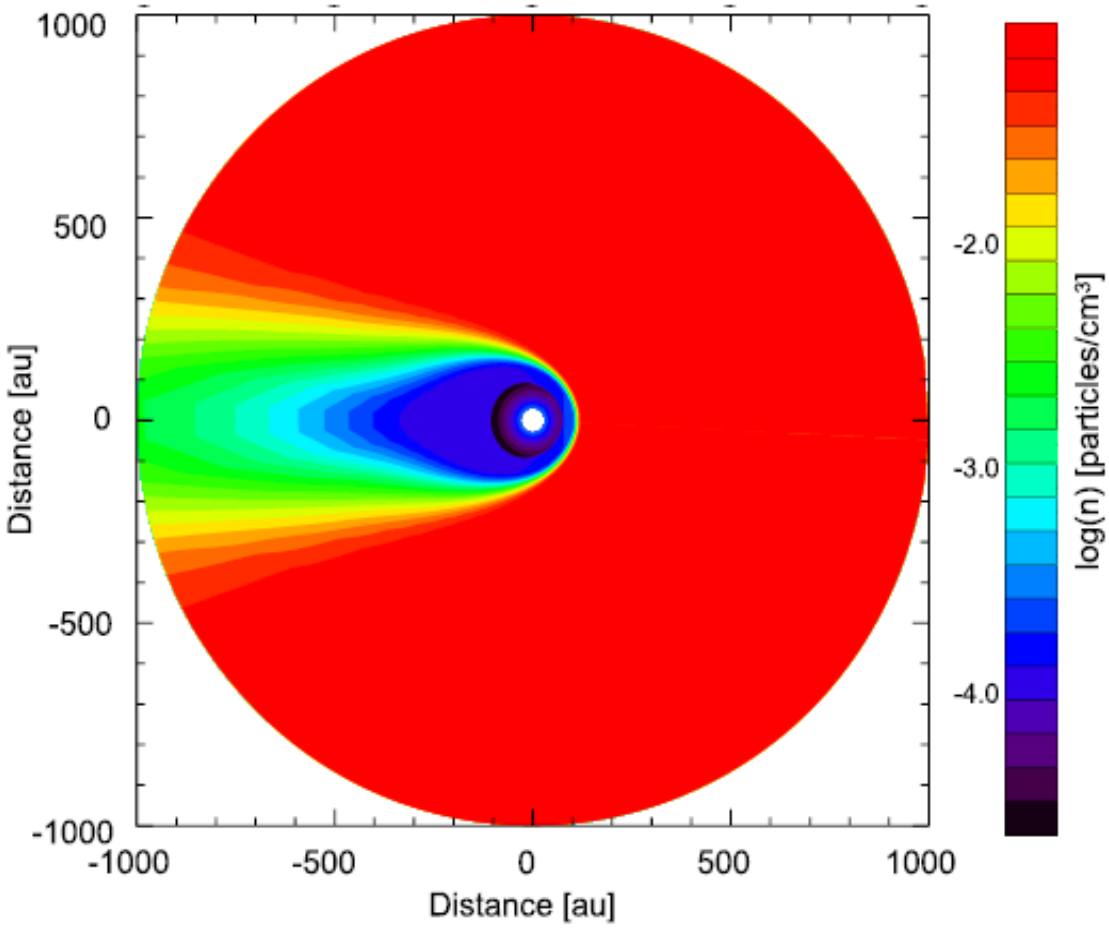

Figure 5.5: *The simulated astrosphere of Proxima Centauri by Herbst et al. (2020). The resolution of the spherical grid used for the simulation is* $N_r \times N_\vartheta \times N_\varphi = 1024 \times 64 \times 32$ *cells.*

For this study, astrospheric simulations of Proxima Centauri with an ISM density of 0.3 particles cm^{-3}, an ISM magnetic field of 2.9×10^{-6} G, ISM temperature of 9000 K and a stellar mass-loss rate of $\sim 5 \times 10^{-17}$ $\mathrm{M}_\odot\,\mathrm{year}^{-1}$ are assumed. The simulations are done on a cartesian grid with 3000 AU simulation volume.

Figure 5.6 shows the computed density at 120 000 years simulation time. The plots illustrate a

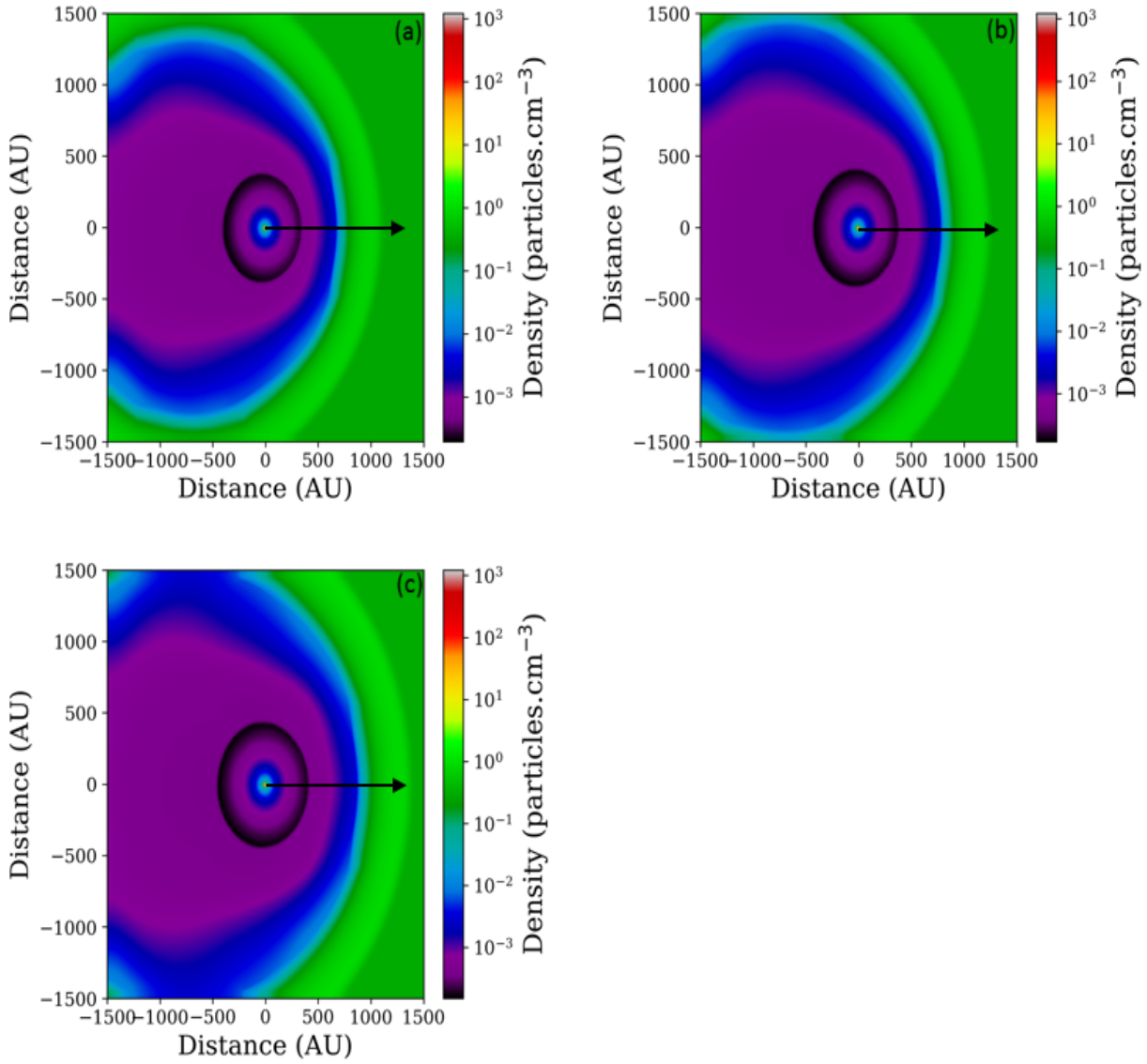

Figure 5.6: *The simulated astrosphere of Proxima Centauri. The density is plotted as a function of the distance for different outflow speeds, illustrating the effect that the outflow speed has on the astrosphere evolution. For panel a the outflow speed is set to 1300* $\mathrm{km\,s^{-1}}$*, for panel b the outflow speed is 1500* $\mathrm{km\,s^{-1}}$ *and for panel c it is 1700* $\mathrm{km\,s^{-1}}$*. An ISM density of 0.3* $\mathrm{particles\,cm^{-3}}$ *and ISM magnetic field of* 2.9×10^{-6} *G are assumed along with a grid cell size of* $\Delta x = \Delta y = \Delta z = \frac{3000\mathrm{AU}}{350}$.

computed astrosphere of Proxima Centauri corresponding to three different outflow speeds increasing from panel a to panel c. Panel a, again top left, has an outflow speed of 1300 $\mathrm{km\,s^{-1}}$, the outflow speed used for the simulation in panel b is 1500 $\mathrm{km\,s^{-1}}$ and then for panel c the outflow speed is 1700 $\mathrm{km\,s^{-1}}$. The rest of the model parameters were left unchanged. A stellar field is also included. Again the parameters are somewhat different to those reported in Herbst et al. (2020) due to updated values found in literature (Scherer, private communication 2022). The overall computed astrosphere for Proxima Centauri is larger than that of LHS 1140. For the larger outflow speed, panel c, the astrosphere is overall larger and the size of the IAS and OAS increases. For the smaller outflow

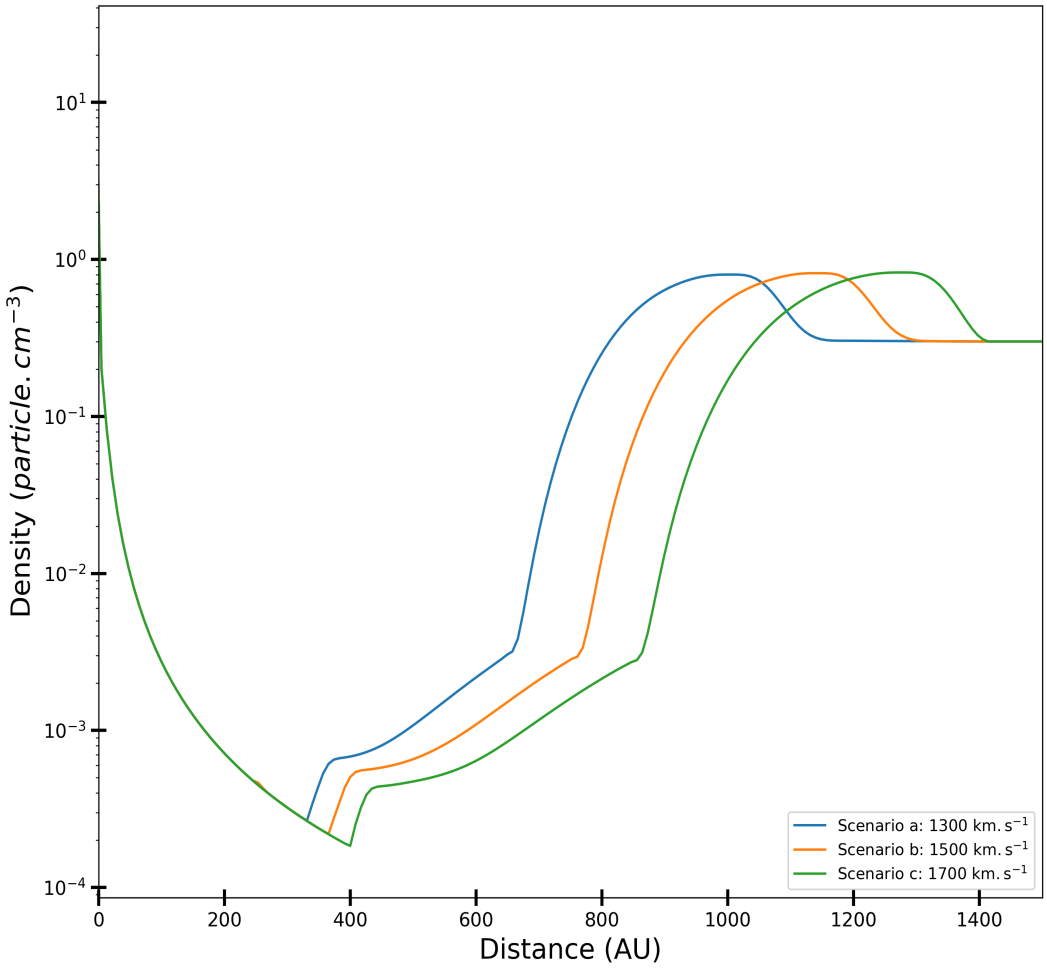

Figure 5.7: *The computed radial density profile taken as a cut along the solid line in Figure 5.6. The blue line, scenario a, is the standard outflow speed scenario of 1300* $\mathrm{km\,s^{-1}}$ *and is taken along the black line of panel a in Figure 5.6, the orange line, scenario b, is for an outflow speed of 1500* $\mathrm{km\,s^{-1}}$ *taken along the line in panel b and the green line, scenario c, is for an outflow speed of 1700* $\mathrm{km\,s^{-1}}$ *taken along the line in panel c.*

speed, panel b, the size of the IAS and OAS decreases. By comparing panel b of Figure 5.6 to Figure 5.5, it shows that there is a clear difference between the two figures at the TS and AP positions as well as the size of the IAS. A possible explanation is the difference in grid cell size as well as the ISM magnetic field magnitude and ISM density assumed for the simulations. Figure 5.6 (this work) has a well-defined BS, whereas Figure 5.5 (Herbst et al. 2020) has no visible BS. However, as mentioned, not quite the same parameters were assumed. Also the simulation times of the two models are different. This is definitely something to study in the near future.

Figure 5.7 shows the radial profile of 5.6. Scenario a, blue line, has an outflow speed of 1300 $\mathrm{km\,s^{-1}}$, while scenario b, orange line, has an outflow speed of 1500 $\mathrm{km\,s^{-1}}$ and scenario c, green line,

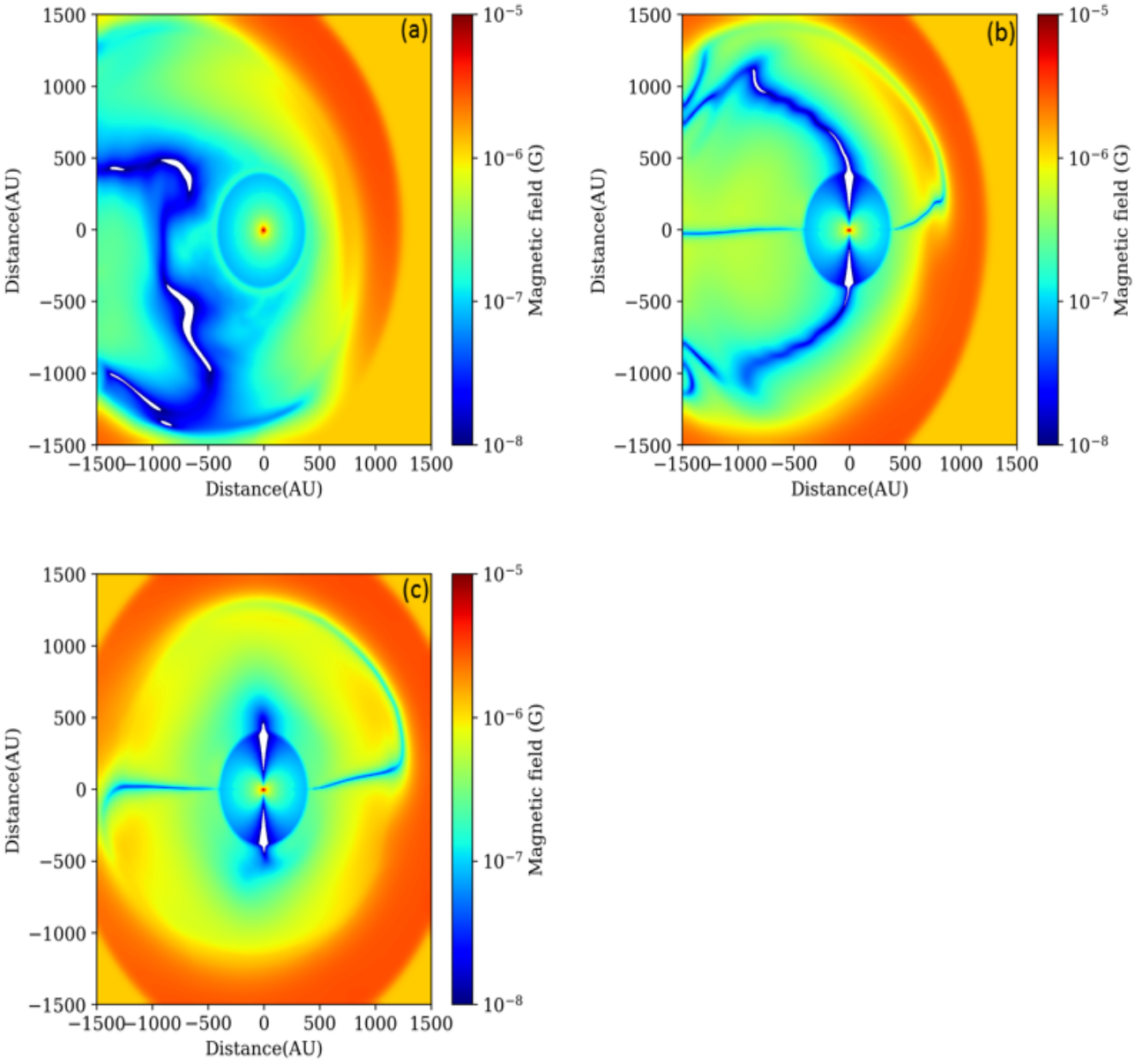

Figure 5.8: *This is the stellar and ISM magnetic field corresponding to Figure 5.6 shown for different orientations. Specifically, the astrosphere simulated in panel b. The assumed outflow speed is the standard scenario of 1500* $\mathrm{km\,s^{-1}}$*. The white regions are the areas where the magnetic field magnitude dips below the model's bottom limit.*

has an outflow speed of 1700 $\mathrm{km\,s^{-1}}$. The radial profiles are made from slices taken along the black line. As the outflow speed increases, the TS, AP and BS move further away from the inner boundary. The TS and BS of scenario a are located at a distance of ∼369 AU and ∼1038 AU, respectively. For scenario b the TS is located at ∼404 AU and the BS is located at ∼1173 AU, and for scenario c the TS is located at ∼432 AU with the BS at ∼1310 AU. The overall structure of the astrosphere of Proxima Centauri is larger than that of LHS 1140. From the standard outflow speed, scenario a, to scenario b, the TS and the BS move outwards by ∼9.5% and ∼13% respectively. For scenario b

to c, the TS and BS move outward by ∼7% and ∼11.7% respectively and then for scenario a to c, the TS moves outwards by ∼17% and the BS moves outwards by ∼26.2%. For the smaller outflow speed, the size of the IAS and the OAS decreases. As the outflow speed increases, the compression of the TS decreases, while the compression of the BS increases. For a decreasing outflow speed, the TS compression ratio increases and the BS compression ratio decreases. As the stellar wind is blown outwards, the density decreases. The ram pressure increases for increasing outflow speed resulting in the ISM being pushed further out by the astrosphere. This is necessary in order for the ram pressure to balance with the ISM pressure.

Figure 5.8 shows the stellar and ISM magnetic field related to Figure 5.6 panel b and is simulated for an outflow speed of 1500 $\mathrm{km\,s^{-1}}$. For this figure, panel a shows the astrosphere in the xy plane, panel b shows the astrosphere in the xz plane and panel c shows the astrosphere in the yz plane. The ISM magnetic field allows the OAS to decompress faster and lowers the density and the compression ratio of the BS, suppressing the BS. Again the plot shows that the magnetic field piles up in specific regions. This leads to an increase of ISM magnetic pressure being exerted on specific areas. Comparing Figure 5.8 to Figure 5.4, it is clear that there is an obvious difference in the stellar magnetic pressure at the TS, with the pressure exerted at Figure 5.4 being higher than that of Figure 5.8. For Figure 5.4, the ISM magnitude at the TS is between 10^{-6} and 10^{-5} G, whereas for Figure 5.8, the ISM magnitude at the TS is between 10^{-7} and 10^{-6} G. Beyond the TS for both figures there is a decrease in ISM magnetic pressure, with an increase towards the BS.

5.4 Summary and Conclusions

In this chapter, a three-dimensional cartesian MHD model was used to simulate the astrospheres of two M-stars, namely LHS 1140 and Proxima Centauri. Results were compared to that of Herbst et al. (2020), who made use of a different MHD model (Kissmann et al. 2018). The effect that the ISM wind speed had on the astrospheric evolution of LHS 1140 and the effect that the outflow speed had on the evolution of the astrosphere of Proxima Centauri were also shown. For this chapter, an ISM magnetic field and a stellar field were included for all simulations.

For LHS 1140, Figure 5.1 showed the computed density from Herbst et al. (2020). The TS was at a distance of ∼8.1 AU, the BS was at a distance of ∼28.9 AU and the AP was at a distance of ∼11.5 AU, which showed that the size of the astrosphere was relatively small when compared to, e.g. the heliosphere. Figure 5.2 showed the density plot as calculated in this work, with Figure 5.3 the corresponding radial plot taken as a cut along the solid line. For panel a in Figure 5.2, the ISM wind speed was 40 $\mathrm{km\,s^{-1}}$, for panel b it was 45 $\mathrm{km\,s^{-1}}$ and then for panel c it was 35 $\mathrm{km\,s^{-1}}$. From the radial profile it was clear that the AP moved further away from the inner boundary as the ISM wind speed decreased. For scenario a, the TS was at a distance of ∼6.1 AU and the BS at a distance of ∼12 AU. For scenario b, the TS and BS were at a distance of ∼5.5 AU and ∼10.6 AU, respectively, while the TS for scenario c was at ∼6.8 AU and the BS was at ∼14.2 AU.

Comparing Figure 5.1 to panel a of Figure 5.2, showed a visible difference in overall astrosphere size. The differences in size could be due to the different parameters assumed as well as the different models and/or different simulation times. However, both models showed that the astrosphere of LHS was much smaller than when compared to that of our local heliosphere. Figure 5.4 was similar to panel a of Figure 5.2, but in terms of the stellar and ISM magnetic field. The assumed ISM wind speed was 40 $\mathrm{km\,s^{-1}}$. The plot shows that the ISM magnetic field piles up in specific regions, increasing the ISM magnetic pressure exerted in those areas.

In Figure 5.6, the astrospheric simulations of Proxima Centauri were shown. Figure 5.6 showed the plot with Figure 5.7 the corresponding radial profiles taken as a cut along the solid line. The astrosphere for Proxima Centauri was significantly larger than the astrosphere of LHS 1140. For panel a in Figure 5.6, the assumed outflow speed was 1300 $\mathrm{km\,s^{-1}}$, for panel b it was 1500 $\mathrm{km\,s^{-1}}$ and for panel c the outflow speed was 1700 $\mathrm{km\,s^{-1}}$. As the outflow speed increased, the TS, AP and BS moved further out and the size of the IAS and the OAS increased. For scenario a, the TS and

BS were located at a distance of ∼369 AU and ∼1038 AU, respectively. For scenario b, the TS was located at ∼404 AU and the BS was located at ∼1173 AU, and then for scenario c, the TS and BS were located at ∼432 AU and ∼1310 AU, respectively.

Figure 5.5 showed the computed density of Proxima Centauri from Herbst et al. (2020). The simulation was done by using the CRONOS code (Kissmann et al. 2018) in spherical geometry. Their results showed that their computed astrosphere had no discernible BS. Comparing this figure to Figure 5.6 showed that there was a difference in the TS and AP positions, as well as in the size of the IAS. As mentioned before, this can possibly be explained by the difference in parameters that were used. In addition, the results of Herbst et al. (2020) were computed in spherical geometry, while in this work, cartesian geometry was used. Of late, the CRONOS code is now being executed in cartesian geometry with more similar parameters as in this study and results are eagerly anticipated.

Chapter 6

Summary and Conclusions

One of the aims of this study was to use HD and MHD models to illustrate the effects of certain parameters on astrospheric evolution and to calculate the astrospheres of LHS 1140 and Proxima Centauri. The two-dimensional hydrodynamic and magneto-hydrodynamic model of Fahr et al. (2000), Scherer & Ferreira (2005) and Ferreira & de Jager (2008) was used for the simulations in Chapter 3, while the three-dimensional cartesian model of Pen et al. (2003), previously used by Strauss (2013) to simulate the heliosphere, was used for the simulations done in Chapters 4 and 5. The two models were discussed in Chapter 2 and a brief summary was given on similar studies done by researchers using the same models.

In Chapter 3, the effects that the mass-loss rate, ISM density, ISM magnetic field and radiative cooling had on astrospheric evolution were illustrated. Including radiative cooling in simulations led to a drop in the thermal pressure of the astrosphere and the compression ratio of the BS increased, reducing the OAS to a thin structure. After cooling, the astrosphere started to decompress leading to a lower density. Radiative cooling influenced the overall structure of the astrosphere and resulted in the creation of smaller circumstellar bubbles. The positions of the TS, AP and the BS, as well as the compression ratio of the BS were affected by cooling.

Simulations were also done for three different mass-loss rates. Changing the mass-loss rate influenced the ram pressure, which led to different-sized astrospheres. A smaller ram pressure resulted in a smaller astrosphere. For a lower mass-loss rate and at earlier simulation times, the density of the outer shell decreased, while the temperature was higher compared to a higher mass-loss rate. This was because of the radiative cooling process. As illustrated at later times, once the cooling process was completed, there was little to no difference between the compression ratios of the TS and the BS for the three different mass-loss rate scenarios.

Also illustrated in Chapter 3 is that the ISM density influenced the compression ratios of the TS and the BS, along with the rate of cooling. The compression ratios of the outer shell were found to be dependent on the ISM. Increasing the ISM density led to the formation of a smaller astrosphere, and the rate at which cooling takes place was increased. The OAS also decompressed faster.

For the effect of different ISM magnetic field scenarios on the astrosphere's evolution, simulations were done for three ISM magnetic field magnitudes. Because of the two-dimensional model limitation, an azimuthal ISM magnetic field was assumed, resulting in the field always being perpendicular to the outflow direction. The ISM magnetic field effected the TS and BS positions along with the compression ratios of both shocks. As the ISM magnetic field magnitude increased, so did the magnetic pressure. For a stronger ISM magnetic field the density and the compression ratio of the BS decreased. The increased magnetic pressure counteracted the effects of radiative cooling, allowing the OAS to decompress faster. This led to the formation of a COAS and a HOAS.

A three-dimensional cartesian MHD model (Pen et al. 2003) was used for the astrospheric simulations done in Chapter 4. Changing the outer boundary distances and keeping the amount of grid points the same, allowed the grid cell size to either be increased or decreased. Astrospheric simulations were done assuming different grid cell sizes, and the results were compared to each other to establish the model's sensitivity to the different grid cell sizes. It was shown that the size of the grid cell used, affected the compression ratios of the TS and the BS. As the grid cell size decreased, the compression ratios increased. Results obtained for a larger grid cell size were also more smooth. The ISM magnetic field included in the model was relatively large and the effect its orientation had on the astrospheric expansion was also shown. In the direction where the flow is parallel to the ISM magnetic field, the magnetic pressure is expected to have almost no effect. However, maximum effects were expected when the outflow is perpendicular to the magnetic field.

The same three-dimensional model was used in Chapter 5 to simulate the astrospheres of both LHS 1140 and Proxima Centauri. For LHS 1140, three different simulations were done for three different ISM wind speeds. The relative speed slightly affected the TS and BS compression ratios. As the ISM wind speed increased, so did the size of the OAS, as a result the BS moved further out. Comparing the results of this study to that of Herbst et al. (2020) showed that the astrosphere simulated by Herbst et al. (2020) was larger than the one computed in this study. The differences were most likely due to the different grid cell sizes, the ISM density and the ISM magnetic field magnitude assumed throughout both studies. The astrosphere of Proxima Centauri was also computed, but for

three different outflow speeds. For a larger outflow speed, the size of the IAS and the OAS increased. As the outflow speed increased, so did the overall size of the astrosphere. Comparing these results to those obtained by Herbst et al. (2020), showed that there was a noticeable difference between the TS and AP positions as well as the size of the IAS. Again the differences could be due to the ISM density, ISM magnetic field magnitude and the difference in grid cell size as well as the difference in simulation times. Efforts are currently underway to standardise parameters between the two models.

Bibliography

Choudhuri, A. R. (1998), *The physics of fluid and plasmas: An introduction for astrophysicists*, Cambridge, UK: Cambridge University Press.

Croswell, K. (2021), *Voyager still breaking barriers decades after launch*, The Proceedings of the National Academy of Sciences, Vol. 118, No. 17.

Dalgarno, A. & McCray, R. A. (1972), *Heating and Ionization of HI Regions*, Astronomy & Astrophysics, Vol. 10, p. 375-426.

Dittmann, J., I. J. C. D. & et al. (2017), *A temperate rocky super-Earth transiting a nearby cool star*, Nature, Vol. 544, p. 333–336.

Evans, C. R. & Hawley, J. F. (1988), *Simulation of magnetohydrodynamic flows - a constrained transport method*, The Astrophysical Journal, Vol. 332, p. 659–677.

Fahr, H. J., Kausch, T. & Scherer, H. (2000), *A 5-fluid hydrodynamic approach to model the solar system-interstellar medium interaction*, Astronomy & Astrophysics, Vol. 357, p. 268–282.

Ferreira, S. & de Jager, O. (2008), *Supernova remnant evolution in uniform and non-uniform media*, Astronomy & Astrophysics, Vol. 478, p. 17–29.

Ferriere, K. (1998), *The hot gas filling factor in our galaxy*, The Astrophysical Journal, Vol. 503, 700È716.

Garraffo, G., Drake, J. J. & Cohen, O. (2016), *The space weather of Proxima Centauri b*, The Astrophysical Journal Letters, Vol. 833, L4 (6pp).

Gottlieb, C. B. & Shu, C. (1998), *Total variation diminishing Runge-Kutta schemes*, MATHEMATICS OF COMPUTATION, Vol. 67, p. 73-85.

Gvaramadze, V. V., Gualandris, A. & Zwart, S. P. (2009), *On the origin of high-velocity runaway stars*, Monthly Notices of the Royal Astronomical Society, Vol. 396, p. 570–578.

Heerikhuisen, J. & Pogorelov, N. V. (2011), *An estimate of the nearby interstellar magnetic field using neutral atoms*, The Astrophysical Journal, Vol. 738, Number 1.

Herbst, K., Grenfell, J. L., Sinnhuber, M., Rauer, H., Heber, B., Banjac, S., Scheucher, M., Schmidt, V., Gebauer, S., Lehmann, R. & Schreier, F. (2019), *A new model suite to determine the influence of cosmic rays on (exo)planetary atmospheric biosignatures*, Astronomy & Astrophysics, Vol. 631, A101.

Herbst, K., Scherer, K., Ferreira, S. E. S., Baalmann, L. R., E., E. N., Fichtner, H., Kleimann, J., Strauss, D. T. R., Moeketsi, D. M. & Mohamed, S. (2020), *On the Diversity of M-star Astrospheres and the Role of Galactic Cosmic Rays*, The Astrophysical Journal Letters, Vol. 897, L27 (7pp).

Herbst, K., Scherer, K., Ferreira, S. E. S., Baalmann, L. R., E., E. N., Strauss, D. T. R., Bykov, A., Izmodenov, V. V., Korolkov, S. D., Levenfish, K. P., Linsky, J. L. & Meyer, D. M. A. (2022), *Astrospheres of Planet-Hosting Cool Stars and Beyond When Modeling Meets Observations*, Space Science Reviews, Vol. 218, p. 29.

Izmodenov, V. V. & Alexashov, D. B. (2015), *Three-Dimensional kinetic-MHD model of the global heliosphere with the heliopause-surface fitting*, The Astrophysical Journal Supplement Series, Vol. 220, p. 32.

Jin, S. & Xin, Z. (1995), *The relaxation schemes of conservation laws in arbitrary space dimensions*, Communications on Pure and Applied Mathematics, Vol. 48, p. 235–277.

Keppens, R., van Marle, A. J., Meliani, Z. & et al. (2012), *Parallel, grid-adaptive approaches for relativistic hydro and magnetohydrodynamics*, Journal of Computational Physics, Vol. 231, p. 718.

Kissmann, R., Kleimann, J. & Krebl, B. (2018), *The CRONOS Code for Astrophysical Magnetohydrodynamics*, The Astrophysical Journal Supplement Series, Vol. 236, p. 53 (26pp).

Light, J. (2017), *Numerical modelling of astrospheres*, North–West University (Potchefstroom Campus), South Africa.

Light, J., Ferreira, S. E. S., Scherer, K., van der Schyff, A. E. & Herbst, K. (2022), *On the numerical modelling of astrospheres, including those of luminous blue variable stars, and the modulation of cosmic rays within*, Monthly Notices of the Royal Astronomical Society, Vol. 516, p. 3284–3296.

Lux, O., Neuhäuser, M. & Bischoff, R. (2021), *A search for runaway stars in 12 Galactic supernova remnants*, John Wiley & Sons, Ltd, Vol. 342, p. 553-577.

Manuel, R. (2013), *Time-dependent modulation of cosmic rays in the outer heliosphere*, North–West University (Potchefstroom Campus), South Africa.

McComas, D. J., Alexashov, D., Bzowski, M., Fahr, H., Heerikhuisen, J., Izmodenov, J., Lee, M. A., Möbius, E., Pogorelov, N., Schwadron, N. A. & Zank, G. P. (2012), *The heliosphere's interstellar interaction: No bow shock*, Science, Vol. 336, p. 1291–1293.

McGreivy, N. (2017), *General Plasma Physics I*, Princeton University, AST 551.

Mellema, G. & Lundqvist, P. (2002), *Stellar wind bubbles around WR and [WR] stars*, Astronomy & Astrophysics, Vol. 394, p. 901-909.

Mohamed, S. & Aydil, E. (2022), *3D models of the circumstellar environments of evolved stars: Formation of multiple spiral structures*, Monthly Notices of the Royal Astronomical Society, Vol. 513, p. 4405–4430.

Moloto, K. D., Engelbrecht, N. E. & Burger, R. A. (2018), *A Simplified Ab Initio Cosmic-ray Modulation Model with Simulated Time Dependence and Predictive Capability*, The Astrophysical Journal, Vol. 859(2), p. 107.

Opher, M., Richardson, J. D., Toth, G. & Gombosi, T. I. (2009), *Confronting observations and modeling: The role of the interstellar magnetic field in Voyager 1 and 2 asymmetries*, The Astrophysical Journal, Vol. 332, p. 659–677.

Parker, E. N. (1958), *Dynamics of the Interplanetary Gas and Magnetic Fields*, The Astrophysical Journal, Vol. 128, p. 664.

Parker, E. N. (1968), *The role of stochastic fields in admitting low-energy galactic cosmic rays to the solar system*, Journal of Geophysical Research, Vol. 73, p. 6842.

Pen, U. L., Arras, P. & Wong, S. (2003), *A free, fast, simple, and efficient total variation diminishing magnetohydrodynamic code*, The Astrophysical Journal Supplement Series, Vol. 149, p. 447–455.

Perets, H. B. & Subr, L. (2012), *The properties of dynamically ejected runaway and hyper-runaway stars*, The Astrophysical Journal, Vol. 751, p. 133.

Pogorelov, N. V., Heerikhuisen, J. & Zank, G. P. (2008), *Probing heliospheric asymmetries with an MHD-kinetic model*, The Astrophysical Journal Letters, Vol. 675, L41–L44.

Pogorelov, N. V., Heerikhuisen, J., Zank, G. P. & Borovikov, S. N. (2009), *Influence of the interstellar magnetic field and neutrals of the shape of the outer heliosphere*, Space Science Reviews, Vol. 143, p. 31–42.

Pogorelov, N. V., Stone, E. C., Florinski, V. & Zank, G. P. (2007), *Termination shock asymmetries as seen by the Voyager spacecraft: The role of the interstellar magnetic field and neutral hydrogen*, The Astrophysical Journal, Vol. 668, p. 611–624.

Richardson, J. D., Kasper, J. C., Wang, C., Belcher, J. W. & Lazarus, A. J. (2008), *Cool heliosheath plasma and deceleration of the upstream solar wind at the termination shock*, Nature, Vol. 454, p. 63–66.

Scherer, K. & Ferreira, S. E. S. (2005), *A heliospheric hybrid model: hydrodynamic plasma flow and kinetic cosmic ray transport*, Astrophysics and Space Sciences Transactions, Vol. 1, p. 17–27.

Scherer, K., Fichtner, H., Kleimann, J., Wiengarten, T., Bomans, D. J. & Weis, K. (2016), *Shock structures of astrospheres*, Astronomy & Astrophysics, Vol. 586, A111.

Scherer, K., Schyff, v. d. A., Bomans, D., Ferreira, S. E. S., Fihtner, H., Kleimann, J. & Strauss, D. T. R. (2015), *Cosmic rays in astrospheres*, Astronomy & Astrophysics, Vol. 576, A97.

Schure, K. M., Kosenko, D., Kaastra, J. S., Keppens, R. & Vink, J. (2009), *A new radiative cooling curve based on an up-to-date plasma emission code*, Astronomy & Astrophysics, Vol. 508, p. 751-757.

Siewert, M., Pohl, M. & Schlickeiser, R. (2004), *The impact of thermal gas in AGN jets on the low-frequency emission*, Astronomy & Astrophysics, Vol. 425, p. 405 - 416.

Snyman, J. L. (2007), *Modelling of the heliosphere and cosmic ray transport*, North–West University (Potchefstroom Campus), South Africa.

Strauss, D. T. R. (2013), *Modelling of cosmic ray modulation in the heliosphere by stochastic processes, Ph.D thesis*, North–West University (Potchefstroom Campus), South Africa.

Strauss, D. T. R. & Effenberger, F. (2017), *A Hitch-hiker's Guide to Stochastic Differential Equations*, Space Science Reviews, Vol. 212, p. 151–192.

Tomisaka, K. (1990), *Blowout of superbubble in galactic magnetic field*, The Astrophysical Journal, Vol. 361, L5-L8.

Toro, E. F. (2009), *Riemann Solvers and Numerical Methods for Fluid Dynamics*, Springer Berlin, Heidelberg, Vol. 3, p. 409.

Van den Eijnden, J., Saikia, P. & Mohamed, S. (2022), *Radio detections of IR-selected runaway stellar bow shocks*, Monthly Notices of the Royal Astronomical Society, Vol. 512, p. 5374–5389.

van der Schyff, A. E. (2016), *Numerical Modeling of the Evolution Stellar Wind Cavities and Supernova Remnants*, North–West University (Potchefstroom Campus), South Africa.

van Marle, A. J., Meliani, Z. & Marcowith, A. (2012), *A hydrodynamical model of the circumstellar bubble created by two massive stars*, Astronomy & Astrophysics, Vol. 541, p. 4.

van Marle, A. J., Meliani, Z. & Marcowith, A. (2015), *Shape and evolution of wind-blown bubbles of massive stars: on the effect of the interstellar magnetic field*, Astronomy & Astrophysics, Vol. 584, A49.

Vorster, M. J., Ferreira, S. E. S., de Jager, O. C. & Djannati-Ataï (2013), *Numerical simulations of composite supernova remnants for small pulsar wind nebulae*, Astronomy & Astrophysics, Vol. 551, A127.

Webber, W. R. & Intriligator, D. S. (2011), *Voyagers 1 and 2 in a shrunken and squashed heliosphere*, Journal of Geophysical Research, Vol. 116(A06105), p. 1–8.

Wood, B. E. & Linsky, J. L. (2016), *Astrospheres, stellar winds, and the interstellar medium*, Cambridge, UK: Cambridge University Press, ISBN: 9781107090477, p. 56-79.